Navigating the Gradient: Melanoma Cell Durotaxis on Gradient Stiffness Substrates

Joshua Clugston

Thesis submitted to the University of Ottawa
in partial fulfillment of the requirements for the
Master's degree in Physics

Department of Physics
Faculty of Science
University of Ottawa

Abstract

The migratory behavior of A2058 human metastatic melanoma cells is investigated on substrates with a gradient in their mechanical stiffness, a process known as durotaxis. New methods were developed to fabricate hydrogel substrates with a gradient in stiffness using a bio-mimetic collagen protein to ensure physiological relevance. The impact of suppressing the protein FMNL2, a protein relevant to melanoma cell motility, was also studied. On isotropic substrates, A2058 cells underwent pronounced changes in their morphology and motility with increasing stiffness. They adopted more elongated shapes as substrate stiffness increased, and their motility decreased as well. The cells displayed a biphasic relationship with stiffness, as an optimal substrate modulus was determined for their motion. The FMNL2 knockdown cells showed similar behavior, but they were continuously more elongated and less motile than the control cells. On the gradient stiffness substrates, A2058 cells displayed a biphasic durotactic behavior. In soft regions (1-15kPa), the cells underwent positive durotaxis, migrating towards a stiffer region, while in stiff regions ($\geq$ 25kPa), they underwent negative durotaxis towards soft regions. Adurotactic motion was noticed between the soft and stiff regions. The FMNL2 knockdown cells showed noticeable decreases in their motility however, they still underwent durotaxis, suggesting that FMNL2 does not impact the mechanosensing abilities of A2058 cells. We then systematically studied the impact of altering the gradient strength of the substrates using new analytical techniques, and increasing gradient strength enhanced durotactic behavior. Overall, we show that local stiffness, within a physiologically relevant range, can have a dramatic impact on the durotactic behavior of A2058 skin cancer cells.

Statement of Originality

Unless stated otherwise, the work presented in this thesis was performed by the author during the duration of their degree under the supervision of Dr. James L. Harden. All experimental work was performed by myself, with some exceptions. The experiments studying cell behavior on silicone substrates was performed by Sarah Fox. The procedure to suppress the protein FMNL2 was also done by Sarah Fox. All data analysis was performed by myself. Data interpretation and final conclusions was performed by myself, Dr. James L. Harden, and Dr. John Copeland. Results from chapters 3, 4, and 5 were included in a presentation done at the Ottawa-Carleton Institute for Physics meeting in May 2023. Similar content was included in a poster presentation done at the Gordon research conference for soft condensed matter physics in August 2023. Chapters 3, 4, and 5 of this thesis are the basis for several manuscripts for publication, as listed below.

Manuscripts for publication:

Clugston, J., Fox, S., Harden, J.L., Copeland, J. A role for the formin FMNL2 in the response of melanoma cells to substrate stiffness, submitted to *BMC Molecular and Cell Biology*.

Clugston, J., Fox, S., Copeland, J., Harden, J.L. A2058 melanoma cells display a biphasic dependence on durotaxis mediated by substrate stiffness, to be submitted to *PRX Life*.

Clugston, J., Wan, F., Harden, J.L. Biomimetic gradient stiffness collagen hydrogels, in preparation for submission to *Biomacromolecules*.

Acknowledgments

First, I want to thank my supervisor, Dr. James Harden. His expertise and advice were crucial to the success of this work, and I couldn't have done it without him. His mentorship has shaped me as a scientist, teaching me to approach and think about problems with a critical mindset, and I am honored to have had the opportunity to learn from him.

I would also like to thank Dr. John Copeland for his help and guidance over the past couple of years. This project wouldn't have been possible without his support, especially in areas beyond my biology knowledge. Additionally, I am grateful to Dr. Sarah Fox for her immense help with the experimental aspects of this work.

Special thanks to Dr. Fan Wan and Lukasz Andrzejewski. Fan spent many hours training me on different equipment and experimental methods, while Lukasz's expertise in designing, constructing, and 3D printing new experimental equipment has been invaluable.

To my parents, Jodi and William, I cannot begin to describe how thankful I am for your support throughout my journey at uOttawa. My success here is not just a result of my efforts at the university, but the culmination of the love, advice, and guidance you have given me since the day I was born. Your unwavering support and belief in me has shaped who I am and laid the foundation for all my achievements.

Finally, a huge thank you to my girlfriend, Madi. You're my biggest supporter, always cheering me on, and I couldn't have done this without you. Through every late night and tough moment, you've been right there, keeping me going with your patience and encouragement. From celebrating every little win to helping me get back up when things got rough. I'm so grateful to have you by my side. Thank you for always believing in me and being my number one fan.

Contents

List of Figures

List of Tables

List of Abbreviations

A: Cell area

AC: Alternating contact

AFM: Atomic force microscopy

DI: Durotactic index

DMA: Dynamic mechanical analyzer

ECM: Extracellular matrix

EDC: 1-Ethyl-3-(3-dimethylaminopropyl) carbodiimide hydrochloride

F-actin: Actin filaments

FD: Feret diameter

FMNL2: Formin-like protein 2

G-actin: Actin monomers

InvOLS: Inverse optical lever sensitivity

KD: Knockdown

LVER: Linear viscoelastic regime

MSD: Mean squared displacement

NHS: N-Hydroxysuccinimide

P: Cell perimeter

PBS: Phosphate buffered saline

RGD: Arg-Gly-Asp

SEM: Standard error of the mean

SPS: Sodium persulfate

TFM: Traction force microscopy

WT: Wild type

d: Dimensionality

D: Diffusion coefficient

E: Young's modulus

E′: Elastic storage modulus

$\mathbf{E''}$: Elastic loss modulus

$\mathbf{\tilde{E}}$: Laterally averaged modulus

$\mathbf{G(t)}$: Relaxational modulus

$\mathbf{G'}$: Shear storage modulus

$\mathbf{G''}$: Shear loss modulus

$\mathbf{G^*}$: Complex shear modulus

$\mathbf{L}$: Path distance

$\mathbf{R}$: Roundness

$\mathbf{S}$: Global order parameter

$\mathbf{S_{Local}}$: Local order parameter

$\mathbf{s_m}$: Average moving speed

$\mathbf{t}$: Time

$\mathbf{t_m}$: Time spent in motion

$\mathbf{v}$: Velocity

α: Anomalous diffusion exponent

$\mathbf{\Gamma}$: Anomalous diffusion coefficient

γ: Shear strain

$\dot{\gamma}$: Shear strain rate

δ: Phase angle

ϵ: Extensional strain

η: Shear viscosity

θ: Net angular displacement

$\mathbf{\Lambda}$: Net displacement

ν: Poisson's ratio

σ: Extensional stress

τ: Maxwell relaxation time

ϕ: Angle between cell body and defined axis

ω: Angular frequency

Chapter 1

Overview

Ever since Robert Hooke first peered at cork through a rudimentary microscope, and Antonie van Leeuwenhoek marveled at the 'animalcules' in a drop of water, the microscopic world has captivated generations of scientists [1]. In the 19th century, Robert Brown's observations of pollen grains suspended in water unveiled the phenomenon of Brownian motion, deepening our intrigue in the microscopic world [2]. These pivotal moments in scientific history have not only revolutionized our understanding of the microscopic structures that make up all life, but have also set the groundwork for further discoveries in all fields of science. Since the aforementioned discoveries in science, the microscopy and imaging equipment has drastically improved, widening the field and introducing limitless opportunities for new fields of research. To the field of biology & biophysics, live cell imaging has had an undeniably dramatic impact [3]. It allows for the detailed study of biological processes such as cell division, cell death, wound healing, and cell migration across large populations, and for the creation of quantitative models describing them [3, 4].

In the field of biophysics, live cell imaging has allowed for the mechanisms that drive cells to migrate to be explored. In a way, it has made these systems increasingly more complex, as we now know of many different factors that can impact cell motion. The concentration of specific molecules, the mechanical properties of their environment, and even electric fields have been found to impact the motion of cells during migration [5, 6].

The purpose of this thesis is to utilize live cell imaging to investigate the affect of discernible changes at the cellular level in environmental stiffness. Specifically, we are looking at a form of

cell migration known as durotaxis, which is migration along a gradient of stiffness. Our chosen system for these studies was a metastatic melanoma cell line, A2058 human metastatic melanoma cells, known for their ability to invade healthy tissue and spread throughout the body.

The second chapter of this thesis acts as an introduction to the necessary cell biology background, focusing on cell motility and specifically durotaxis. We also introduce melanoma cells, and previous work that has been done in regards to their motility. Specific proteins thought to be relevant to their motility are also introduced, as we investigate the affects of suppressing these proteins later on.

In the third chapter, we introduce the background, experimental methods, and physical theory necessary for characterizing the mechanical properties of soft materials. Methods for fabricating and characterizing soft materials that mimic the *in vivo* environments melanoma cells reside in are also discussed. We also introduce the system that will be used to create the substrates for studying durotaxis here. Furthermore, we also present and discuss the developed methods and results for creating gradient stiffness substrates utilized in chapter 5.

Previous work has shown that cells can undergo drastic changes in their behavior when residing on substrates of different stiffness. The aim of the fourth chapter is to characterize the behavior of our melanoma cells on isotropic stiffness substrates. Specifically, we study the role of substrate stiffness on the morphology and motility of the melanoma cells, as well as the effects of suppressing FMNL2, a protein relevant to cell motility, in A2058 melanoma cells. The results showed that A2058 melanoma cells undergo pronounced morphological changes, becoming increasingly more elongated with increasing substrate stiffness. Interestingly, we find that for their motility, their exists an optimal stiffness that maximizes their migration. Furthermore, we show that FMNL2 knockdown in A2058 cells had an impact on their morphology and motility. These results provide a vital control and tool for comparison for the following chapter on cellular behavior on substrates of gradient stiffness.

In the penultimate chapter, we then present and discuss the results of A2058 melanoma cell motion on gradient stiffness substrates. We utilize our results from chapter 3 on the mechanical properties of the substrates and the results of cell motion on homogeneous stiffness substrates from

chapter 4 to draw conclusions regarding the cellular response to gradients in substrate stiffness. We find that these cells did exhibit changes in their motility, with cells preferentially aligning and moving along the direction of the gradient. However, their motility was found to be dependent on both the rate at which the stiffness changed, as well as the absolute stiffness of their starting position.

In the sixth and final chapter, we summarize the results of the thesis, and propose new areas of research based on our findings and unanswered questions. Following this chapter, there are appendices with supplementary information.

Chapter 2

Introduction to Cell Motility

2.1 Background

2.1.1 Cell Biology

Cells are the fundamental units of life, with each type carrying out intricate processes to contribute to the entire organism [7]. At the microscopic level, they represent the smallest entity that can carry out all the functions of life. In the vast web of life that spans from simple single-celled organisms to complex multicellular organisms like humans, cells provide both the building blocks and the operational framework. Their complexity is reflected in their complex internal structure, where both genetic and biochemical activities are carefully coordinated. This intricate organization within cells sets the stage for understanding their dynamic capabilities and structural components.

The Cytoskeleton

Analogous to the organs found in the human body, individual cells are composed of many subcellular structures called organelles, each fulfilling specific roles within the cell. Central to these structures is the cytoskeleton, which is crucial not only for maintaining cell shape and the organization of organelles but also for cell motion. The cytoskeleton itself is constructed from three types of protein fibers: microfilaments, intermediate filaments, and microtubules [8]. Among these, microfilaments, also known as actin filaments, consist of actin protein monomers. These

filaments dynamically assemble and disassemble through processes termed polymerization and depolymerization, respectively.

The cytoskeleton is not just a structural component of the cell, but also plays pivotal roles in cell signaling, intracellular transport, and cellular responses to external stimuli. This dynamic network responds to and influences the cell's interactions with its environment, setting the stage for understanding how microfilaments contribute to these processes. Microfilaments form structures that enable the cell to exert protrusive forces by contracting and extending these fibers, and by relative motion of these fibres generated by protein motors. Located primarily around the cell's perimeter, these structures include filopodia and lamellipodia. Filopodia are thin, hair-like protrusions that explore the local environment; they consist of multiple actin filaments aligned in parallel bundles that confer their slender shape. Conversely, lamellipodia are flat, sheet-like protrusions at the cell's leading edge, facilitating movement. They feature a network of crosslinked actin filaments that provides the necessary mechanical support for environmental probing and locomotion.

As microfilaments support the cellular architecture, their influence extends beyond the cell itself. Through structures like lamellipodia and filopodia, the cell engages with the extracellular matrix (ECM), which is the local environment surrounding the cell. Cell protrusions can interact with the ECM through, for example, the formation of a structure known as a focal adhesion. Focal adhesions act as an anchor to the ECM, and are formed in response to interactions of specific ECM protein domains with transmembrane proteins known as integrins [9]. These integrins can be classified into subfamilies, according to their binding affinity to specific ECM proteins, such as fibronectin, collagen, and laminin [10]. Integrins generally facilitate the connection between the cell's internal structures and its external environment. Arg-Gly-Asp (RGD) is a peptide sequence found in many proteins in the ECM and is recognized by several types of integrin proteins. In particular, it is found in in some forms of collagen, as well as in fibronectin, a glycoprotein that is locally secreted by some cells into the ECM to promote cell-ECM adhesion [11]. Due to their ubiquitous function in cell-ECM binding, RGD peptides are widely used to functionalize traditionally non-adhesive surfaces, such as plastic or hydrogels like polyacrylamide, to enhance

cell adhesion for *in vitro* studies

Focal adhesions provide a means for cells to directly interact with and learn about their environment. At these binding sites, cells can generate both intracellular and extracellular forces to sense their environment, which can directly impact their resultant behavior. It is this process, the transformation of mechanical cues into biochemical responses, that is the essence of mechanosensing. Understanding these mechanisms is crucial as they form the foundation for cellular behaviors such as motility and directed migration, subjects that will be further explored in subsequent sections.

Cell Migration Mechanisms

Cell migration involves the movement of cells from one location to another and is essential for numerous physiological functions, including development and wound healing. This process relies on a cells ability to perform mechanotransduction, which is the transformation of mechanical signals into biochemical actions inside of the cell. To understand the process of cell migration, we can utilize the motor clutch model to explain how the interactions between a cell and its surrounding ECM facilitate motion [12, 13, 14].

Migration begins when a cell becomes polarized in the direction of motion, characterized by distinct leading and trailing edges. The process of actin monomers (G-actin) polymerizing into actin filaments (F-actin) underpins this process. Rapid polymerization at the leading edge results in the extension of lamellipodia in the direction of motion (Figure 2.1-1). The lamellipodium then anchors to the substrate through a new focal adhesion, driving the plasma membrane forward (Figure 2.1-2). Concurrently, at the trailing edge focal adhesions are disassembled, which generates backward tension on the F-actin network, inducing the retraction of the trailing edge in the direction of motion (Figure 2.1-3). New F-actin formation at the leading edge propels older filaments toward the trailing edge, creating a retrograde flow. This flow is resisted by the cell's attachment to the substrate, allowing continuous actin polymerization at the leading edge, which in turn advances the cell [15]. A new lamellipodium is then formed, and the cycle then restarts (Figure 2.1-4). Thus, the protrusion of the leading edge combined with the retraction of the

trailing edge facilitates overall cell movement [13].

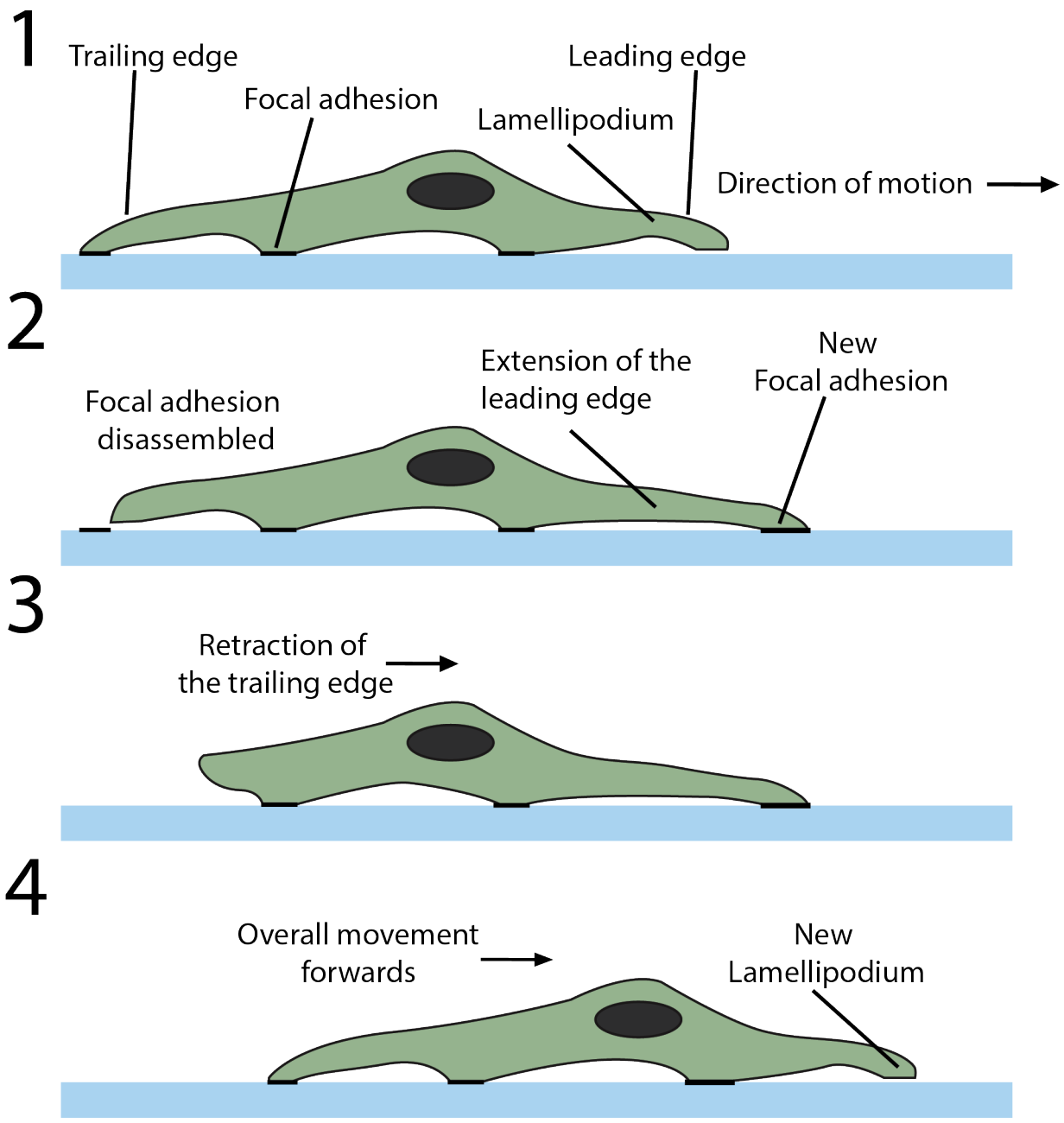

Figure 2.1: The motion of cells described in four steps: In the first, a new lamellipodium is formed, extending in the direction of motion. In the second, the focal adhesion at the trailing edge is disassembled, while a new one forms at the leading edge. In the third step, the disassembly of the trailing edge focal adhesion causes the trailing edge to retract in the direction of motion. The cycle then begins again with the formation of a new lamellipodium at the leading edge.

From this process, we can see that mechanosensing and generating forces with the ECM is a vital component of cell motion. As such, cells will often exhibit different behavior on substrates of different rigidity, as the stiffness of the substrate can impact the magnitude of force that cells

can generate [16]. On stiff substrates, cells can generate larger contractile force, which results in cells adopting elongated morphologies with stable actin stress fibers that are well aligned with the long axis of the cell and also in the formation of stable focal adhesions that facilitate cell binding and motility [16, 17, 18]. Conversely, on soft substrates, cells will adopt round morphologies, with radially distributed actin fibers around the cell [16, 17], resulting in reduced force generation that can limit cell attachment to the ECM and reduce cell motility. This behavior suggests that cells would likely migrate towards stiffer environments where they can form stable interactions with the ECM, although there are notable exceptions.

Forms of Cell Migration

Cell movement can occur randomly as cells explore their environment, or it can be directed by extracellular signals that guide their migration. The nature of cell motion, whether random or directed, is influenced by both intrinsic cell directionality and external regulatory factors. Intrinsic cell directionality relates to the cell's autonomous response to motogenic signals, which are cues that trigger the mechanisms of cell motion [19]. For instance, in the presence of uniformly ligand binding sites on a cell culture dish, cells exhibit low intrinsic directionality, leading to random motion. Conversely, if motogenic stimuli are presented as an external gradient, the cell's internal steering mechanisms align with the external signal to produce directed motion [15].

The nature of the motion is intricately linked to the type of external signal received. Directed motion in response to chemical signals dissolved in the environment is termed chemotaxis, while motion driven by gradients of substrate binding sites or cues in the ECM is known as haptotaxis [20]. In this chapter, we focus on durotaxis, which is directed cell migration in response to spatial gradients in substrate stiffness [15].

2.2 Migration along a stiffness gradient

2.2.1 Introduction to durotaxis

Cells have been shown to respond to a variety of external signals, that can all affect their resultant motion. Durotaxis is the directed motion of cells in response to mechanical signals in the form of spatial changes in substrate stiffness. This migratory method was first shown to exist in NIH-3T3 fibroblast cells, where these cells were found to directionally migrate from soft to stiff areas of their substrate [21]. This motion, from soft to stiff environments, is known as positive durotaxis. Since it's discovery, the majority of durotaxis studies have found cell lines exhibiting positive durotaxis. A vast array of cells including Schwann cells [22], smooth muscle cells [23], and a range of cancer cells [24], have all been found to exhibit behavior consistent with positive durotaxis [25, 26]. Other studies have also shown that durotaxis is a property of both single and collective cell migration, and that collective cell durotaxis is more efficient than single cell durotaxis in some cell lines [27]. Collective positive durotaxis has been reported in groups of MDCK cells [27], as well as groups of human epidermal carcinoma cells [28]. These collective behaviors indicate that durotaxis could be a factor in the coordination of larger scale cell events, such as wound healing, where it is speculated that mechanical coordination of cell groups would be required for such processes [25, 29].

The observed motility behavior in cell types exhibiting positive durotaxis are consistent with basic features of the motor clutch model of cell motion. However, the motor clutch model also predicts behavior that goes against the idea of cells continuously seeking stiffer regions [30]. In particular, biphasic regions of stiffness are predicted to exist for some cell types, for which there exists an intermediate stiffness region where traction force would be maximized [30]. This suggests that cells would not necessarily migrate towards the stiffest area of the substrate, but rather would seek an optimal area that maximizes their force generation with the substrate. This then suggests that some cell types may exhibit negative durotaxis, which is directed motion from a stiff to soft area (if their optimal stiffness is less than that of their current mechanical environment). Furthermore, once in their optimal stiffness region, some cells may exhibit adurotactic motion, which is when cells do not move in preferential directions in response to a stiffness gradient [25].

Evidence of both negative durotaxis and adurotactic motion have been found in some cell types. One comparative study on multiple cancer cell lines [24] found that all of the cancer cell lines tested exhibited the strongest durotactic response in the softest region of their substrates (2-7kPa), and in the stiffer regions, the durotactic behavior of these cells was dramatically reduced. This study also found that these cells had the lowest average speeds in the softest areas of the substrates, where they exhibited the largest durotactic response, indicating that cell speed was not a good indication of durotactic motion in these cell lines. Another study on U251-MG glioblastoma cell motility[31] found that the optimal stiffness region governing motile response could be modulated by changing the number of available motor proteins, consistent with the behavior predicted by the motor clutch model. Furthermore, some cell types have been found to undergo negative durotaxis. The first recorded evidence of this behavior was seen in Xenopus retinal ganglion cells, for which cell expansion progresses from stiff to soft areas of their environment [32]. This behavior has also been found in some cancer cell types melanoma skin cancer cells, which are known for their ability to invade healthy tissue [26, 33]. Moreover, U251-MG cells have also been shown to undergo negative durotaxis, as when observed on stiff areas greater than 10kPa, they would preferentially migrate down to their optimal stiffness region between 5-10kPa [26].

Despite numerous motility studies done *in vitro*, the prevalence of durotaxis for systems *in vivo* remains unclear, with few studies showing evidence of its occurrence. The difficulty in doing so lies in the complexity of real living systems, which contain a wide range of signals that cells can respond to. For example, the morphology and biochemical composition of the ECM of living tissues often changes between different tissues, making it difficult to determine the true underlying causes of cell migration behavior. One area that durotaxis could be relevant to *in vivo* is embryonic development, as cells have exhibited durotactic behavior in both developing mice and Xenopus frogs [29, 34]. Another *in vivo* process that durotaxis is thought to be relevant to is cancer cell invasion, as *in vivo* tumor microenvironments are often stiffer than the surrounding healthy tissue [35, 36, 37]

2.2.2 Altering Durotactic Behavior

There are multiple factors that can impact the durotactic response of motile cells. One factor that can be experimentally adjusted *in vitro* is the strength of the stiffness gradient of the supporting ECM-mimetic substrate, which refers to the rate at which the modulus of the material is changing with distance along the substrate. By changing this quantity, the change in stiffness a polarized cell can sense between its leading and trailing edges would be affected, resulting in potentially different cell behavior. For example, in a study done on mesenchymal stem cells, three different gradients were used: 1 Pa/μm, 10 Pa/μm, and 100 Pa/μm [38]. In all three cases, the cells underwent positive durotaxis and preferentially navigated to the stiffer side of the material. However, the migration speed of the cells, defined as the component of velocity in the direction of the gradient, was found to correlate with the strength of the gradient [38]. In another study, the same relationship was found with smooth muscle cells, as their durotactic response increased with the strength of the gradient [39], as shown by the average distance travelled in the direction of the gradient increasing with the strength of the gradient. Another factor that has been found to affect some cell lines durotactic ability, is the absolute range of stiffness exhibited across the substrate. As previously mentioned, some cancer cells lines have been found to exhibit positive durotaxis on soft substrates between 2-7kPa, while on stiffer substrates (7-18kPa), their durotactic potential was dramatically reduced, in spite of having the same gradient of stiffness across the substrate (20Pa/μm) [24].

2.2.3 Quantifying Durotactic Behavior

Mean Squared Displacement

Cell motility on a substrate is a complex process that typically involves alternating periods of active cell propulsion and quiescent states. During the active phases, cells propel themselves using the actin-myosin network, as discussed above. These forces drive the cell forward, but the direction, velocity, and duration of these propulsion phases may not be consistently correlated across successive periods. This variability can result in a range of motility behaviors, including random walks and directed motion.

Tracking cell movement over time is a fundamental technique in the study of cell motility, providing critical insights into the behavior of cells as they navigate their environment. This process typically involves capturing the position of a cell at successive time points using high-resolution microscopy techniques, coupled with image processing algorithms that accurately identify and track the cell's center of mass, nucleus, or another point of interest (such as a fluorescent marker). The core idea of cell tracking is to generate a time series of the cell's position, represented as $\vec{r}(t_i)$, where t_i corresponds to the i-th time point in the observation period. This time series enables researchers to construct a trajectory of the cell's movement, which is essential for quantitative analyses. Knowing the precise position of the cell at each time point allows for the calculation of various dynamic parameters, such as speed, persistence, and the mean squared displacement (MSD). One of the key advantages of cell tracking is its ability to capture the heterogeneity of cell behavior. By analyzing the trajectories of individual cells, different modes of motion can be identified.

Once the cell's position is known at each time point, one of the most informative metrics that can be calculated is the MSD [40]. The MSD provides a measure of the average squared distance that a cell travels over a specified time lag τ. This metric is particularly powerful because it encapsulates both the extent and nature of the cell's movement over time. Mathematically, the MSD is defined as the ensemble average of the squared displacement of the cell's position vector between an initial time t_0 and a later time $t_0 + \tau$:

$$\Delta r^2_{\mathrm{MSD}}(\tau) = \langle \|\vec{r}(t_0 + \tau) - \vec{r}(t_0)\|^2 \rangle_{t_0} \tag{2.1}$$

Knowing the cell's position at each time point allows for the determination of the displacement vector $\vec{r}(t_0+\tau)-\vec{r}(t_0)$, which is the cornerstone of the MSD calculation. By averaging the squared magnitudes of these displacement vectors over many time intervals and possibly many cells, the MSD reveals how far, on average, a cell moves as a function of time lag τ.

The shape and scaling of the MSD as a function of τ provide deep insights into the underlying mechanisms driving cell motion. For example, a linear relationship between MSD and time lag ($\Delta r^2_{\mathrm{MSD}}(\tau) \sim \tau$) indicates purely diffusive motion, where the cell's movement is random and

uncorrelated. In contrast, A relationship of $\Delta r^2_{\text{MSD}}(\tau) \sim \tau^\alpha$, with α indicating scaling behavior, can suggest directed motion if $\alpha > 1$ or confined motion if $\alpha < 1$, which is discussed further below.

Purely Diffusive Motion

In the simplest model of cell motility, cells move randomly on the substrate, a behavior analogous to Brownian motion. Each step the cell takes has a length $\ell = \|\vec{dr}\|$ and occurs in a random direction within a small time interval dt. Over a time interval t, the probability distribution for the cell's displacement vector $\vec{R}$ can be shown to follow a Gaussian distribution, a result derived in d dimensions in Appendix A. The Gaussian form of the probability distribution for random walk processes in two dimensions is given by:

$$P(R,t) = \frac{1}{4\pi Dt} \exp\left(-\frac{R^2}{4Dt}\right) \tag{2.2}$$

where D is the diffusion coefficient, a parameter that quantifies the rate of spreading of the cell's position over time. The MSD in 2D for purely diffusive motion can be derived from the second moment of this probability distribution as follows (a derivation in d dimensions is available in Appendix A). The MSD, denoted by $\langle R^2(t)\rangle$, is defined as:

$$\langle R^2(t)\rangle = \int_0^\infty R^2 P(R,t)\, 2\pi R\, dR \tag{2.3}$$

where $2\pi R\, dR$ is the differential area element in two dimensions, accounting for the circular symmetry. Substituting the probability distribution into this expression and simplifying, we have:

$$\langle R^2(t)\rangle = \frac{1}{2Dt} \int_0^\infty R^3 \exp\left(-\frac{R^2}{4Dt}\right)\, dR \tag{2.4}$$

This integral can be evaluated using the substitution $u = \frac{R^2}{4Dt}$, which gives $du = \frac{R\, dR}{2Dt}$. Substituting and simplifying our expression then gives:

$$\langle R^2(t)\rangle = 4Dt \cdot \int_0^\infty u \exp(-u)\, du \tag{2.5}$$

The integral $\int_0^\infty u \exp(-u)\, du$ can be solved using integration by parts, and is equal to a value of 1. So, our expression then becomes:

$$\langle R^2(t) \rangle = 4Dt \tag{2.6}$$

Thus, the mean squared displacement (MSD) for cells moving diffusively in two dimensions is:

$$\Delta r^2_{\text{MSD}}(\tau) = 4D\tau \tag{2.7}$$

where τ is the lag time and D is the diffusion constant.

Here, D represents the diffusion constant, which depends on factors such as the cell's environment and intrinsic motility mechanisms. This linear relationship between MSD and time lag is characteristic of freely diffusive processes and serves as a baseline model for more complex behaviors.

Biased Diffusive Motion

In the study of cell motion, the movement of cells can often be influenced by external signals, leading to a biased diffusion process. Such external signals can include chemical gradients (chemotaxis) or variations in substrate stiffness (durotaxis), which cause the cell to preferentially move in certain directions. This bias can be mathematically modeled by considering different probabilities for the cell to move in the x and y directions. Specifically, let p_{+x} and p_{-x} be the probabilities of moving forward and backward along the x-axis, and p_{+y} and p_{-y} be the probabilities of moving forward and backward along the y-axis. In a scenario where the probabilities in the x-direction are equal ($p_{+x} = p_{-x}$), the motion in the x-direction would be purely diffusive. However, if the probabilities in the y-direction are unequal ($p_{+y} > p_{-y}$), the motion in the y-direction would exhibit a biased behavior, leading to a net displacement along the y-axis. This model allows us to understand how cells can experience both random diffusion in one dimension and directed movement in another, reflecting the complex nature of cellular navigation in response to environmental cues.

The simplest 1D biased diffusion model assumes that the particle or cell can only move in two directions: forward or backward. The probability of moving forward is p_+, and the probability of

moving backward is p_-. If $p_+ > p_-$, the cell experiences a net drift in the forward direction. This model can be analytically derived and solved to understand the combined effects of diffusion and drift, providing insights into how directional movement emerges from stochastic processes. The full derivation can be found in Appendix A, with the main steps shown below.

Consider a particle moving in one dimension under the influence of a bias [41]. The particle can jump to the right with probability p_+ and to the left with probability p_- in each time step Δt. The particle moves a distance ℓ in each step. For a single step, the mean displacement $\langle \Delta x \rangle$ is:

$$\langle \Delta x \rangle = \ell \cdot p_+ \Delta t + (-\ell) \cdot p_- \Delta t = \ell(p_+ - p_-)\Delta t \tag{2.8}$$

The simplified variance of the displacement $\mathrm{var}(\Delta x)$ is:

$$\mathrm{var}(\Delta x) = \ell^2(p_+ + p_-)\Delta t \tag{2.9}$$

For a total time t, where the particle takes $N = \frac{t}{\Delta t}$ steps, the total mean displacement $\langle x(t) \rangle$ and variance $\mathrm{var}(x(t))$ are:

$$\langle x(t) \rangle = N \langle \Delta x \rangle = \ell(p_+ - p_-)t \tag{2.10}$$

$$\mathrm{var}(x(t)) = N \mathrm{var}(\Delta x) = \ell^2(p_+ + p_-)t \tag{2.11}$$

Thus, the drift velocity v and diffusion coefficient D are given by:

$$v = \frac{\langle x(t) \rangle}{t} = \ell(p_+ - p_-) \tag{2.12}$$

$$D = \frac{\mathrm{var}(x(t))}{2t} = \frac{\ell^2(p_+ + p_-)}{2} \tag{2.13}$$

The probability of finding the particle at position x at time $t + \Delta t$ is:

$$P(x, t + \Delta t) = [1 - (p_+ + p_-)\Delta t]P(x, t) + p_+ \Delta t \cdot P(x - \ell, t) + p_- \Delta t \cdot P(x + \ell, t) \tag{2.14}$$

Expanding $P(x, t + \Delta t)$, $P(x - \ell, t)$, and $P(x + \ell, t)$ using a Taylor series and substituting them

back into the original probability function yields a simplified expression in form of the diffusion equation. However, there is an additional term arising from the bias, which is the drift velocity of the cell.

$$\frac{\partial P(x,t)}{\partial t} = -v\frac{\partial P(x,t)}{\partial x} + D\frac{\partial^2 P(x,t)}{\partial x^2} \tag{2.15}$$

This partial differential equation can be solved using the Fourier transform method (shown in Appendix A) to obtain the following probability function:

$$P(x,t) = \frac{1}{\sqrt{4\pi Dt}} \exp\left(-\frac{(x-vt)^2}{4Dt}\right) \tag{2.16}$$

This is the Gaussian solution for the probability distribution, which contains an additional term that accounts for the drift velocity v.

To find the mean squared displacement $\langle x^2(t)\rangle$, we again compute the second moment of the distribution to then obtain:

$$\langle x^2(t)\rangle = (vt)^2 + 2Dt \tag{2.17}$$

where $v = \ell(p_+ - p_-)$ is the drift velocity, and $D = \frac{\ell^2(p_+ + p_-)}{2}$ is the diffusion coefficient. The result of the 1D biased diffusion model shows that the motion of the cell is characterized by a combination of random diffusion and a deterministic drift velocity. The diffusion component arises from the random nature of the movement, where the cell has a certain probability of stepping forward or backward at each time step. This leads to a spread in the position of the particle over time, described by the diffusion coefficient D. This behavior is shown in Figure 2.2 showing the time evolution of the probability functions of both unbiased and biased 1D random walks. In both cases, the variance of the distributions becomes larger with time, proportional to the diffusion coefficient. However, the introduction of a bias in the step probabilities p_+ and p_- results in an additional drift term, which causes the mean position of the cell to shift in the direction of the bias (Figure 2.2A). This drift velocity v represents the net effect of the bias, effectively "guiding" the random motion in a particular direction. The combined effect of diffusion and drift means that the cell's position over time is not purely random but also exhibits a predictable component in the

direction of the bias. In Figure 2.2B, a comparison between the 1D MSD functions are shown. At low times, both curves show similar linear behavior, but at large times, the quadratic term from the drift velocity results in the noticeable increase in the biased MSD function. This behavior is similar to the durotactic motion of cells on 2D substrates. Perpendicular to the gradient, there are no extracellular signals causing directed motion, resulting in freely diffusive motion. Along the gradient, the difference in substrate stiffness acts as a bias in their motion, causing them to preferentially move along the gradient direction.

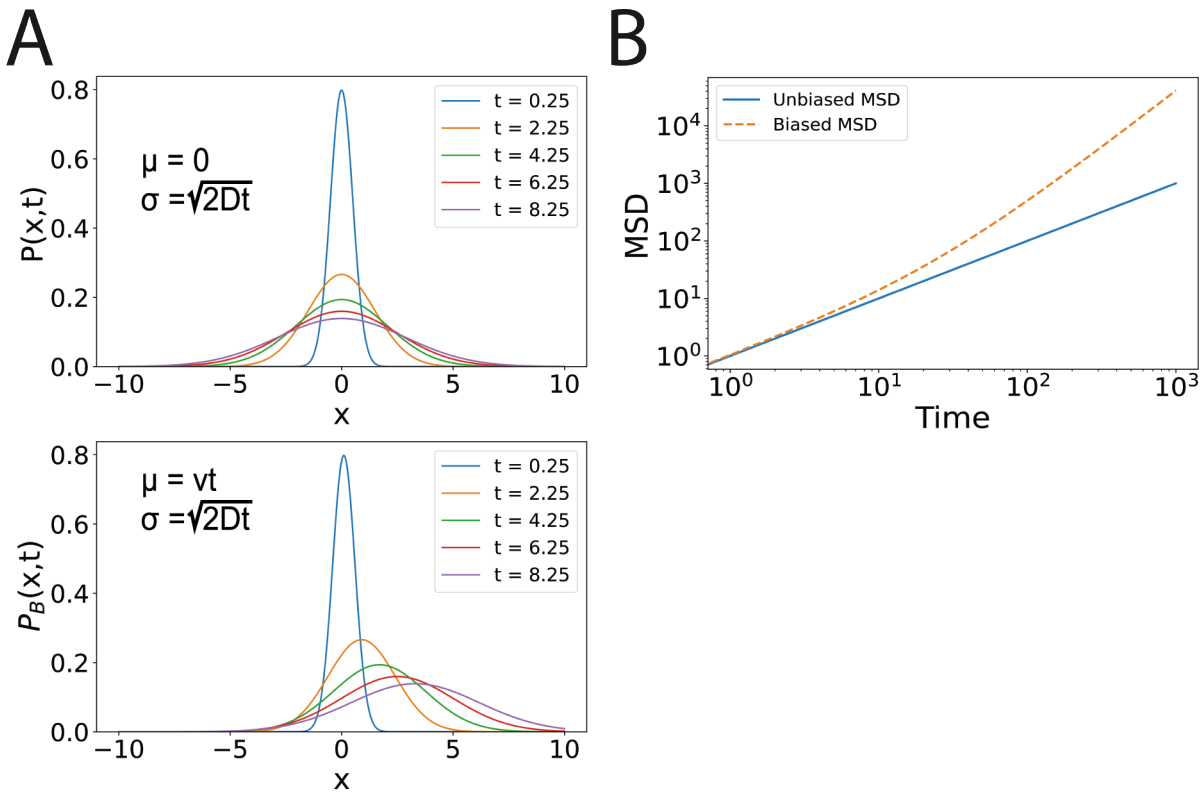

Figure 2.2: A: Two plots showing the time evolution of unbiased ($P(x,t)$) and biased ($P_B(x,t)$) probability distributions showing the evolution of their mean (μ) and standard deviation (σ). B: The 1D MSD function of biased (orange), and unbiased (blue) random walks.

Generalized MSD

Measured cell MSD data can be applied to characterize the nature of cell motility on biological substrates (e.g. to determine the extent to which cell motion is random or directed). In the case of durotaxis, we can compare the motion of cells on homogeneous and gradient stiffness substrates using the MSD. On homogeneous stiffness substrates, the motile cells should possess a

low intrinsic directionality due to the lack of motogenic signals, resulting in random cell motion, while the opposite is true on the gradient substrates. To show this, we can plot the MSD vs time and the resulting curve can be analyzed to determine characteristic regimes of cell motion. If the MSD plot is linear in time, i.e $MSD \propto t$, then the cells are undergoing free diffusion (shown in Figure 2.3) [42], and the effective diffusion coefficient of the cell can be obtained from the data.

However, nonlinear behavior of MSD curves often arises in biological systems, which is known as anomalous diffusion [42]. This form of diffusion can be expressed as the following

$$MSD = \langle \Delta \vec{r}(\tau)^2 \rangle = 2d\Gamma\tau^{\alpha} \tag{2.18}$$

where α is the anomalous exponent [42], Γ is the anomalous diffusion coefficient, and d is the system dimensionality. Figure 2.3 shows each of the specific types of diffusion associated with nonlinear behavior. If the MSD plot is nonlinear and following a fractional power law, i.e $MSD \propto t^{\alpha}, \alpha < 1$, then the particles are undergoing subdiffusive motion [43]. This behavior indicates that there are additional underlying dynamical processes or constraints hindering motion. This kind of motion has been consistently found in 3D cell culture studies, due in part to confinement effects [43]. The second case, where $MSD \propto t^{\alpha}, 1 < \alpha < 2$, is indicative of superdiffusive motion, where the particles are undergoing some form of directed motion. The third case, where $\alpha = 2$, is ballistic motion, indicative of particles moving at constant velocity [44]. It is normally seen for a objects moving at a constant velocity, described by $r = \nu\tau$. The final case, where $\tau > 2$, is hyperballistic motion, which has been in observed in optical systems [45], but is not normally observed in biological settings.

In the context of cell motility, analyzing MSD plots provides insights into how cells respond to their environment. Subdiffusive behavior, observed for instance in 3D cell studies within dense or highly crosslinked environments, indicates constrained and hindered motion. Conversely, on standard cell culture plates, cells may exhibit nearly diffusive behavior due to the absence of motogenic signals, resulting in random motion. Superdiffusive behavior has been observed in some cell lines that undergo directed migration [46]. Furthermore, the diffusive behavior of cells is not always constant; the anomalous exponent and diffusion coefficient describing the MSD of

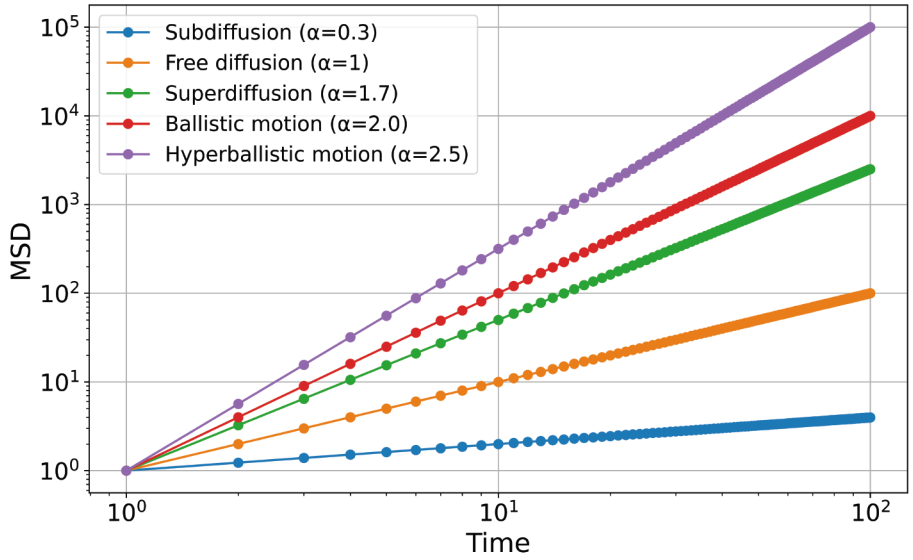

Figure 2.3: Simulated ensemble MSD curves for $N = 10^4$ particles undergoing subdiffusive, diffusive, superdiffusive, ballistic, and hyperballistic motion.

a cell's motion can vary over time [47, 46]. The MSD can also provide insight for how cells are moving in their environment, and can be used to compare how cells respond to different stimuli, such as substrate stiffness [43]. On different stiffness substrates cell motility can differ, as cells may move slower or faster depending on how close the stiffness of the substrate is to their optimal stiffness. For instance, the study by Luzhansky et all found that MDA-MB-231 breast cancer cells show a biphasic dependence on substrate stiffness, and had an optimal stiffness around 18kPa, as this is where the MSD and average speed of the cells was at a maximum. Furthermore, through the analysis of the cells MSD curves, they showed how different characteristics of their anomalous MSD model, either α or Γ (the anomalous diffusion coefficient), were sensitive to different components of the cells environment. The anomalous exponent was more sensitive to the substrate stiffness, while Γ was more sensitive to changes in the surfaces adhesive ligands; which are what the cells use to attach themselves to the substrate.

Van Hove Correlation

Another quantity that can be used to show directed cell motion is the displacement, which is calculated as follows

$$\vec{\Lambda} = \langle \vec{r}(t) - \vec{r_0} \rangle, \tag{2.19}$$

where $\vec{r}(t)$ denotes the displacement of the cell at a given time t, and $\vec{r_0}$ denotes the defined initial position. Since this metric is not squared, it can be either positive or negative, and the sign can then indicate in which direction the cells preferentially moved towards over a specified time interval. This quantity is typically calculated for the components of $\vec{\Lambda}$ in each orthogonal direction, and the resultant values averaged over the cell population can be plotted as a histogram. This data can then be fit with a model for the distribution function, often known as the Van Hove distribution in the context of particle tracking. For simple diffusive motion of identical elements, a Gaussian distribution around 0 would be expected, whereas directed motion would show a skewed distribution in the direction of cell migration. Moreover, heterogeneity in the motility of the cell population also leads to broadening of the distribution function. By calculating the Van Hove distribution for a sufficient number of lag times one can also calculate the full MSD as a function of τ, and then calculate other related metrics [48].

Commonly Used Durotaxis Metrics

To further quantify cell durotaxis, numerous other metrics have also been defined to determine the strength of the durotactic response of a given cell. Using time lapse videos of cell motion, each cell can be tracked, and their coordinates recorded at each time step. With these coordinates, different values including displacement, distance travelled, and velocity can all be calculated. The components of vector quantities along specified directions (e.g. along the direction of the gradient of substrate stiffness) are of particular interest. Figure 2.4, illustrates several of the variables used as durotaxis metrics for the case of a stiffness gradient in the $\hat{y}$ direction. One of the most commonly used metrics for studying durotaxis is the Durotactic Index (DI), calculated as

$$DI = \frac{\Delta y}{L} \tag{2.20}$$

where Δy is the distance travelled in the gradient direction, and L is the total distance travelled by the cell. This value can range between 0 and 1, with lower values indicating random cell motion and values closer to 1 indicating persistent motion along the gradient.

Cell motion along the gradient can also be quantified using the net angular displacement of

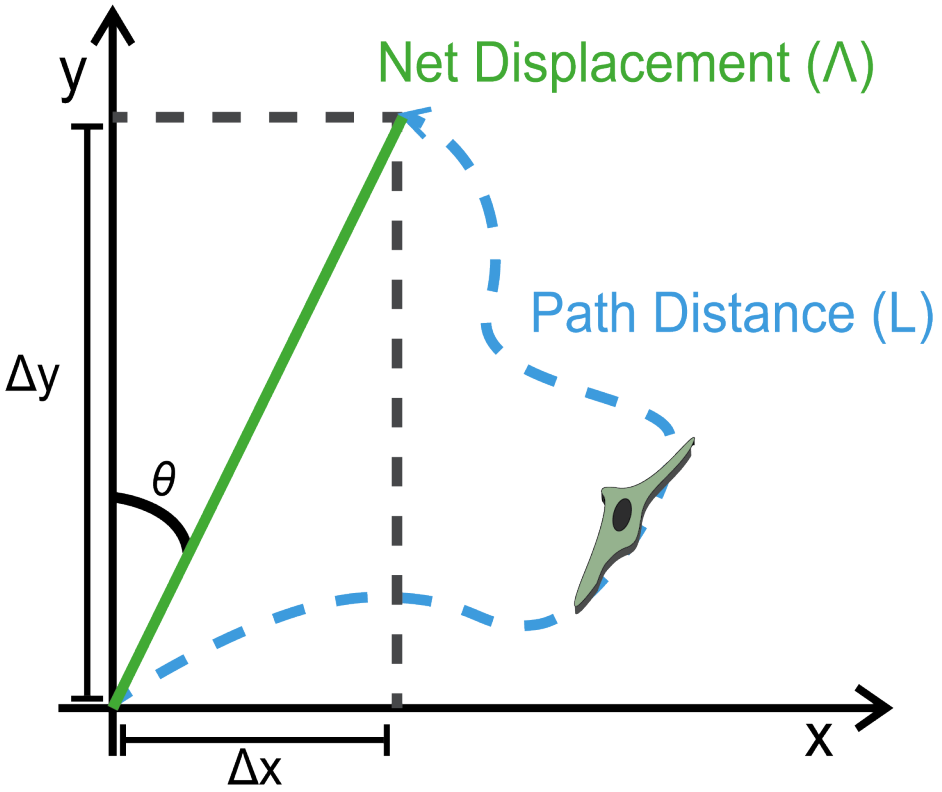

Figure 2.4: A drawing of a path a cell can take in response to a stiffness gradient in the $\hat{y}$ direction, showing the quantities that can be extracted from its motion for further analysis.

the cell, $\theta(t)$, by determining the angle between the instantaneous net displacement vector $\vec{\Lambda}(t)$ and the stiffness gradient direction, $\hat{y}$ according to the following:

$$\theta = arctan\left(\frac{\Delta x}{\Delta y}\right). \tag{2.21}$$

When the time-series of angular displacements of each cell are then plotted from 0° to 360° as a histogram, the motion of the cells can then be classified as random or persistent according to the resultant distribution. A uniform distribution around the entire plot indicates random motion, as the cells moved in all directions, while a tighter distribution around a specific angle would indicate persistent cell motion in that direction.

Using the net displacement of the cell $\vec{\Lambda}(t)$, the components of the average velocity of the cell can also be determined using

$$v_{x,y} = \frac{\Lambda_{x,y}}{t}, \tag{2.22}$$

where $\Lambda_{x,y}$ and $v_{x,y}$ are the Cartesian components of the net displacement and average velocity,

and t is the time parameterizing the cell coordinates. If the cell is undergoing some form of directed motion, then what would likely be seen is the component of velocity parallel to the gradient would be larger than the perpendicular component.

In addition to characterizing motility, we can also analyze the morphology of the cells to gain some insight into their behavior. To do so, we can define metrics that define the shape the cells have adopted. One way to do this, is to fit an ellipse to all cells being studied, and then calculate the ratio between the minor and major axis of the ellipse. This is known as the roundness (R) of a cell, and is calculated as

$$R = \frac{b}{a} \tag{2.23}$$

where and a and b denote the major and minor axis respectively. R can be a value between 0 and 1, where values close to 1 indicate circular morphologies, while values approaching 0 mean the cell is needle-like. During motion, cells tend to become more elongated, so this metric can be used to compare cell morphology between isotropic and anisotropic stiffness substrates. Moreover, cells have been shown to change their shape according to the stiffness of the substrate they reside on [49]. So, this quantity can also be used to show the affect of substrate stiffness on cell morphology.

The orientation of cells on their substrate may also be coupled to the direction of their motion. We can define a 2D orientational order parameter that will quantify the orientation of cells along a specific axis. This order parameter is calculated by finding the angle between each cell and a defined axis, and then using the following expression to define a local parameter for a given cell:

$$S_{Local} = 2cos^2\phi - 1, \tag{2.24}$$

where ϕ is the angle between the axis and the major axis of the cell (Figure 2.5). The local order parameter for all cells can then be plotted as a histogram to observe the distribution of cell orientations. We can then obtain the global order parameter as an average over the local values for each cell:

$$S = \langle S_{Local} \rangle. \tag{2.25}$$

S has traditionally been used to describe the orientation of anisotropic particles on a flat surface

with respect to a specific direction [50, 51].

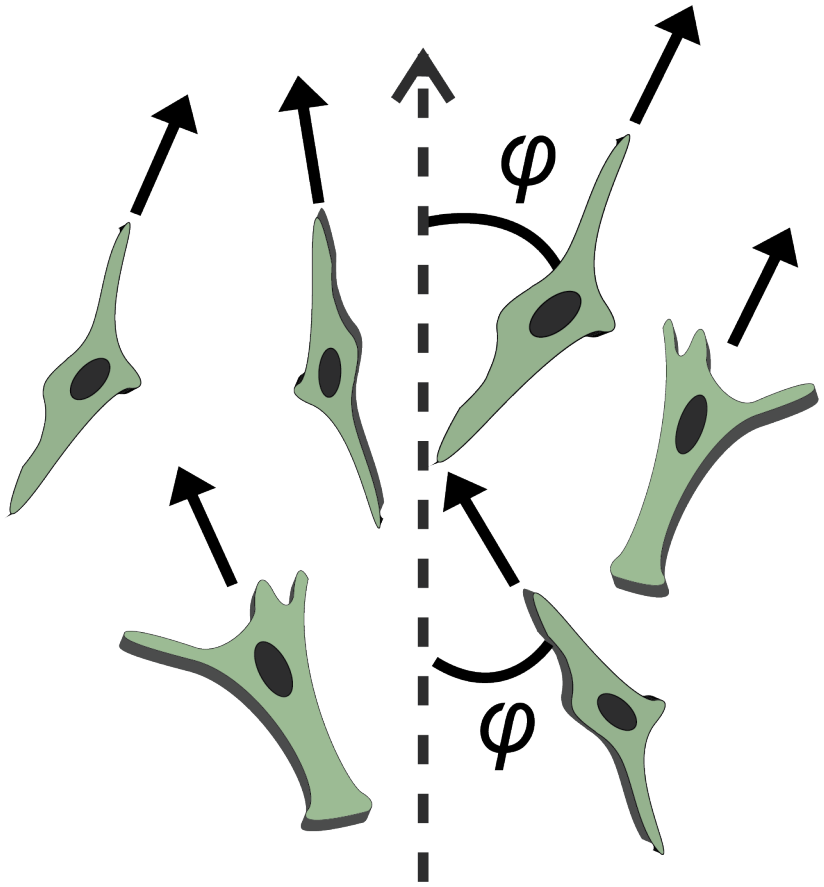

Figure 2.5: A cartoon drawing of cells and the angle they make along a defined axis. The angle between the cell body and the axis can be used to calculate the order parameter.

In this thesis, all of the previously described parameters will be used to quantify the motion of cells on different substrates.

2.3 Melanoma Cell Migration

2.3.1 Introduction to Melanoma

Skin cancer is one of the most prevalent types of cancer in the world, with thousands of new cases being reported each year [52]. Although the survival rate of skin cancer is high, the largest number of deaths come from the type of skin cancer known as melanoma [52]. Melanoma begins in melanocyte cells, which are melanin-producing cells originating in the basal layer of the epidermis,

the top layer of skin. This cancer is the most aggressive and deadly form of skin cancer, as it can rapidly spread or metastasize to other areas of the body if left untreated. The incidence rates of melanoma have also dramatically increased over the past couple of decades, with thousands of reported deaths around the world each year. To create new treatment plans for melanoma, understanding how melanoma cells metastasize and migrate throughout the body is crucial.

For cancer metastasis to occur, the cancerous cells must first probe their environment using various cell protrusions to determine whether to migrate. Using filopodia and lamellipodia primarily, these cells will sense different signals, such as substrate stiffness, that can then impact their subsequent motion. Cancerous tissues frequently exhibit increased stiffness when compared to the surrounding healthy tissues, so a gradient in substrate stiffness is created at their boundary. This differential stiffness, discernible at the cellular level, can influence cell migration [53]. Due to this, it is thought that durotaxis could be a factor in cancer metastasis [24]. Some melanoma cell lines have been found to exhibit durotactic behavior while migrating. Particularly, both B16 and A375 melanoma cells have been shown to undergo negative durotaxis, and preferentially move towards softer environments [33]. Beyond these two cell lines, no other melanoma cell lines have been shown to display durotactic behavior.

2.3.2 Formin Proteins

Cell migration is heavily dependent on the protrusions cells use to probe their environment. In cancerous cells such as carcinoma and breast cancer cells, increased filopodia formation has been linked to increased invasion by these cells [54]. These protrusions are dependent on a group of proteins known as formins, which aid in regulating actin polymerization and the binding and bundling of F-actin [55, 56, 57, 58]. Some formin proteins, such as Formin like-2 (FMNL2), and Formin like-3 (FMNL3), have been shown to contribute to increased filopodia formation in multiple cell lines [59, 60]. In particular, FMNL2 has been shown to be involved with the formation and turnover cell-cell attachment sites, as well as cell-substrate attachment sites (FAs) [61, 62]. As well, FMNL2 has been shown to initiate filopodia assembly in melanoma cell lines [63]. Cell motility studies on melanoma cell lines have also been done to study the affect of FMNL2 on cell

motion. In A375 melanoma cells, specific forms of FMNL2 have been found to be upregulated during cell motion [60]. Moreover, in B16 melanoma cells, efficiency of migration was reduced when FMNL2 was silenced [64].

In this thesis, A2058 melanoma cells will be studied to determine if they respond to changes in substrate stiffness and if they are durotactic. They will first be studied on homogeneous stiffness substrates, and then studied on gradient substrates. All of the quantitative metrics shown in this chapter will be used to quantify and compare their morphology and motility on these substrates. Furthermore, the affect of suppressing FMNL2 will also be studied on both homogeneous and gradient stiffness hydrogel substrates. In the subsequent chapter, the methods for fabricating and characterizing these homogeneous and gradient stiffness hydrogel substrates will be presented in detail.

Chapter 3

Fabricating and Characterizing Gradient Stiffness Hydrogels

3.1 Introduction

To study the motion of cells on substrates with a gradient in stiffness, we must first fabricate the substrate material, and then determine ways of characterizing its mechanical properties. For the majority of the results in this thesis, these substrate materials will be collagen hydrogels. The focus of this chapter will be on the different methods employed to fabricate and characterize these substrates. Different methods of creating gradient modulus substrates will be explored to determine which ones are best for our studies. These methods will employ different properties of the chosen materials, and some methods are combined to create the ideal gradient.

3.2 Background

3.2.1 Hydrogels

Hydrogels are viscoelastic materials composed of a network of linked of polymer chains solvated by an aqueous solution [65]. These materials are composed of both a viscous component, such as water, and a solvated polymeric component, which gives the material its elastic properties. To

form a hydrogel, the solubilized components must become crosslinked, or bonded to each other, to form the network that gives the gel its elastic properties. These crosslinks can be either transient or chemical in nature.

Transient crosslinking refers to crosslinks in these systems that are not permanent; they can be reformed, broken, or altered in response to specific stimuli such as changes in temperature, pH, light exposure, or mechanical stress [66]. This behavior enables transient crosslinked hydrogels to undergo significant changes in properties like viscosity, elasticity, and porosity. These crosslinks are generally formed due to physical interactions between neighbouring polymer chains in the gel, such as electrostatic interactions or entanglement between chains. Chemical crosslinking refers to the formation of strong covalent bonds between different sites of neighbouring polymers [67]. These bonds are often irreversible without denaturing the polymer itself. Due to this, chemically crosslinked hydrogels are often significantly stronger than those formed by physical interactions [66].

Collagen Hydrogels

Collagen is the most abundant protein found in humans, and accounts nearly one third of the entire protein content in our body [68]. This is because it forms the basis of the ECM found around most of the cells in our bodies [68]. This protein has a unique, triple-helical structure, composed of three polypeptide chains that wind around each other to form the helix. Each of these chains are sequences of amino acids, which are the monomers that make up proteins. Collagen proteins can have 19 (out of the total 20), amino acids appearing in their sequence, but the most common are glycine, proline, alanine, and hydroxyproline. The most abundant amino acid, glycine, is found at every third residue in the chain, as it is what allows collagen to adopt its triple helical shape.

Inside the human body, there are numerous types of collagen, each with differing structures to suit their role in the body. Type 1 collagen, found in skin, tendons, ligaments, and organs [69] is the most common one in the body. Type I collagen fibers are packed together to form long, unbranched cables with high tensile strength and toughness, providing resilience to tissues [70]. It is for these reasons, that type 1 collagen is typically utilized in hydrogels for biomedical

applications [69, 70].

In most forms of collagen, hydrogels are formed through thermal gelation of reconstituted collagen. In this case, lyophilized collagen is first dissolved into solution, where individual collagen molecules are separated and well dispersed [68, 71]. When the temperature of the solution is increased to physiologically relevant temperatures, around 37°C, the collagen strands then reassemble into their triple helical structure. Following this, the collagen triple helices then self-associate to form collagen fibrils, which in turn associate into fibers. The fibrils and fibers are stabilized in solution by physical interactions and in some cases by intermolecular crosslinking, which then creates a robust hydrogel structure.

For the work done in this thesis, a series of bio-mimetic collagen 1 proteins based on the collagen-like protein Sc12 from the bacteria *Streptococcus pyogenes* were used [72]. These proteins are highly soluble, form robust triple helical assemblies in a variety of aqueous solution conditions, and are capable of forming stable hydrogels in physiologically relevant environments through the use of several chemical crosslinking methods. We employed four members of this series in the studies for this thesis: the base bio-mimetic collagen 1 protein (VB), which is optimized for chemical crosslinking of carboxylate and amine residues using a variety of well-established bioconjugate chemistries, and a variant (GYQ) that has been modified to include tyrosine residues in the sequence, to allow for crosslinking to occur through the formation of dityrosine bonds. Furthermore, two additional variants of these (VB-RGD and GYQ-RGD) which include RGD sequences to enhance cell adhesion to the hydrogels were also utilized. Typically, hydrogels for these studies utilized mixtures of the four collagen-mimetic variants, as described below. The details of the crosslinking methods utilized to make these hydrogels are presented in the following three subsections.

Collagen Crosslinking - EDC/NHS

A primary method that can crosslink all collagen-mimetic variants introduced above employs two crosslinkers, 1-Ethyl-3-(3-dimethylaminopropyl) carbodiimide hydrochloride (EDC), and N-Hydroxysuccinimide (NHS), with the reaction mechanism shown in Figure 3.1 [73, 74]. When

introduced to an aqueous solution of collagen, the first step that occurs is the reaction of the EDC with free carboxyl groups along a strand of collagen. These carboxyl groups would be found primarily on the side chains of aspartic acid and glutamic acid residues. This reaction then forms an unstable intermediate known as O-acylisourea. Following this, one of three reaction pathways can occur. In the first pathway, O-acylisourea will react with water and undergo hydrolysis, which removes the EDC, resulting in no crosslinking between collagen strands [74, 75]. In the second pathway, O-acylisourea will react with an amine group on another collagen strand, to form a stable amide bond. However, hydrolysis is more likely to occur than this pathway. The third pathway involves the second crosslinker, NHS, which reacts with O-acylisourea. In this reaction, the EDC molecule is removed and an amine-reactive group that has higher stability than O-acylisourea is formed, which then reacts with a free amine group on another collagen strand to form an amide bond crosslink. This is the primary reason for using NHS in this reaction, as it will react with the intermediate created by EDC to form a more stable intermediate that is more likely to form crosslinks. It is also important to note that both EDC and NHS are left in solution at the end of the reaction, allowing them to be washed out.

Collagen Crosslinking - Genipin

Another method to chemically crosslink all collagen-mimetic variants involves genipin, a natural crosslinker extracted from gardenia fruit. Known for its low cytotoxicity, genipin has been effectively utilized to crosslink various hydrogels, including collagen, chitosan, and gelatin [76, 77, 78, 79, 80]. The reaction mechanism targets the primary amine groups of the collagen, typically involving lysine, arginine, or hydroxylysine residues [81]. Initially, genipin reacts with these amino groups, which modifies its ring structure, enabling subsequent reactions (Figure 3.2). A nitrogen atom from the collagen then replaces an oxygen atom in genipin's six-member ring, forming a covalent bond between genipin and collagen. Subsequently, two genipin-collagen complexes react, resulting in a structure where two genipin molecules and two collagen fibers are covalently linked [81]. It is also important to note that unlike the EDC-NHS mechanism, genipin integrates itself into the final structure of the collagen matrix, resulting in permanent qualitative changes. During

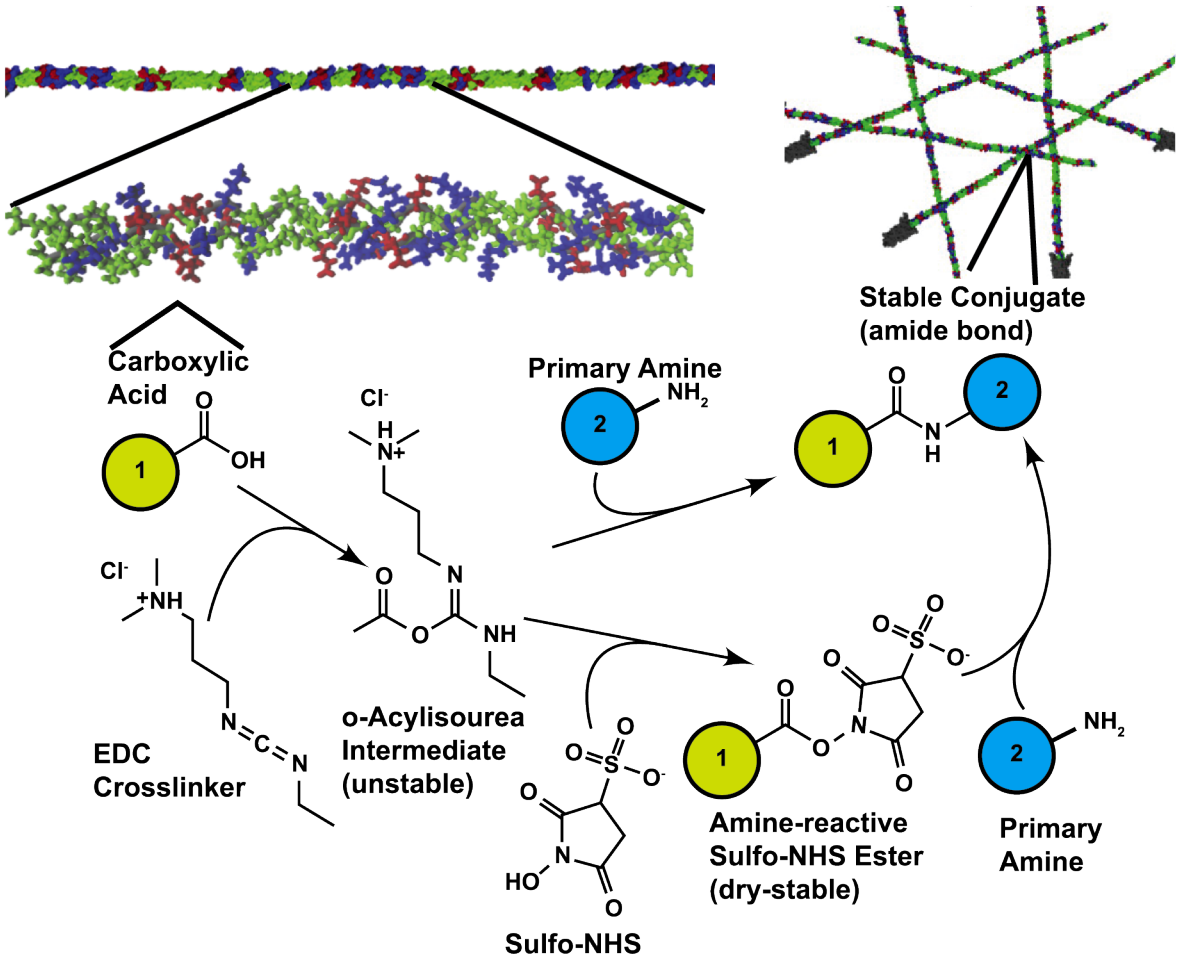

Figure 3.1: The reaction pathways for EDC & NHS crosslinking with collagen. EDC first reacts with a carboxylic acid functional group, creating O-acylisourea. This molecule can then either hydrolyze, with no crosslink forming, react with a primary amine group on the collagen strand to form a crosslink, or react with NHS to form another intermediate. This intermediate then reacts with a primary amine group, forming a crosslink.

this reaction, the altered form of genipin incorporated into the collagen network turns permanently blue, which allows for spectroscopic assessment of the reaction's progress. This is advantageous given that genipin's reaction can take up to 72 hours to complete, which is considerably longer than other collagen crosslinking methods [82].

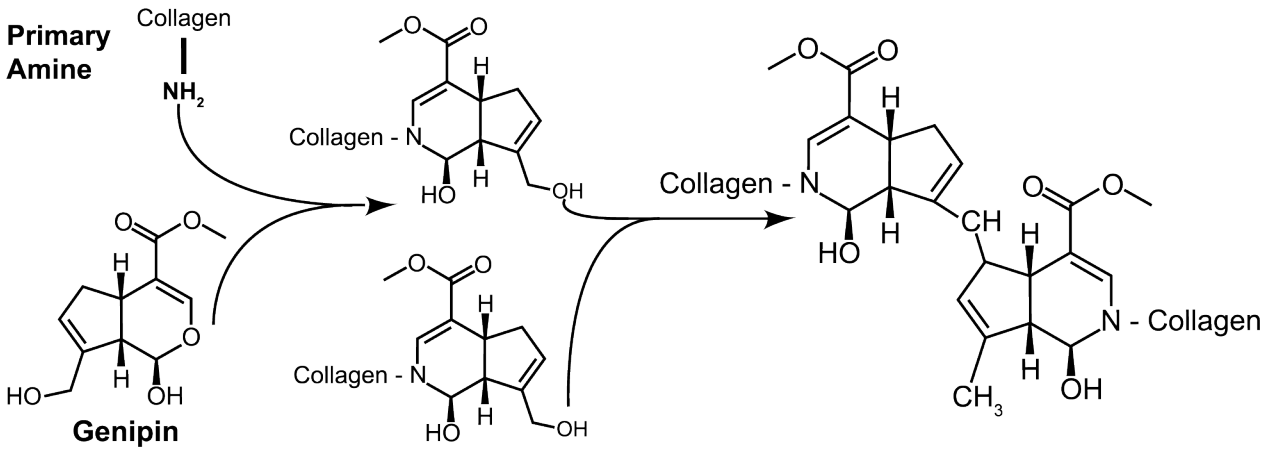

Figure 3.2: Genipin reacts with collagen through a reaction with primary amine groups on the strand. The genipin molecule now becomes covalently bonded to the amine group. Two of the genipin-collagen complexes can then react, resulting in a crosslink with genipin remaining in the final structure.

Collagen Crosslinking - Riboflavin Photocatalysis

The final method is used for crosslinking of the tyrosine-containing collagen-mimetic variants (GYQ and GYQ-RGD). Tyrosine features a phenyl ring with a bonded hydroxyl group at the terminus of its side chain, that can be used for chemical crosslinking to create intermolecular dityrosine bonds. Many methods have been created to form these bonds, including the use of the enzyme horseradish peroxidase [83], as well as multiple photocatalysts including ruthenium, rose bengal, and riboflavin (vitamin B_2) [84, 85, 86, 87]. In collagen systems, the use of both rose bengal and riboflavin have been studied due to their low cytotoxicity, and have been successfully used in clinical applications to enhance the strength of corneal collagen [84, 88].

In the studies done in this thesis, riboflavin crosslinking will be explored as a method of creating collagen hydrogels. In this crosslinking method, riboflavin acts as a photoinitiator, which are molecules that generate reactive species when exposed to specific wavelengths of light. Upon exposure to UVA light, riboflavin transits to a singlet (short-lived, $10^{-8}s$) or triplet (long-lived,

10^{-2}s) state, where two reaction pathways can then occur, both involving the triplet state. In type 1 reactions, the triplet state directly interacts with the tyrosine and oxidizes it. While in type 2 reactions, the riboflavin transfers energy directly to ground state oxygen, which produces reactive singlet state oxygen ions which then reactive with tyrosines. Finally, two tyrosyl radicals then react together, creating a dityrosine bond [88, 89].

One drawback of using riboflavin is its slow rate of crosslinking, which can be improved by the use of sodium persulfate (SPS) [90]. The use of SPS with riboflavin has been successfully tested in other hydrogels including silk fibroin and keratin hydrogels, with each study reporting decreased crosslinking time and increased crosslinking density with its use [90, 91]. However, the exact mechanism by which SPS accelerates the reaction kinetics is currently unknown, but is thought to be caused by SPS rapidly regenerating the excited riboflavin state [90].

3.2.2 Material Characterization

Stress & Strain

To mechanically characterize a material and its properties we have to study how it responds to different applied forces. In general, there are three types of forces that are relevant for this thesis: tensile, compressive, and shear (Figure 3.3). Tensile forces act to elongate or stretch a material in the direction of the applied force and decrease its cross-sectional area. Compressive forces act in the direction opposite to tensile ones, resulting in decreased length and increased cross sectional area. Shear forces are applied parallel or tangential to the face of a material, causing the material to slide over itself and deform at constant volume.

To derive relevant expressions describing the behavior of materials under these forces, we can start by studying the materials elasticity, or its ability to return to its original size after a deformation. For an applied uniaxial tensile/compressive force on a material, we can define a characteristic extensional stress σ as

$$\sigma = \frac{F_z}{A_z} \tag{3.1}$$

where F_z is the applied force in the $\hat{z}$ direction, and A_z is the cross sectional area of the material

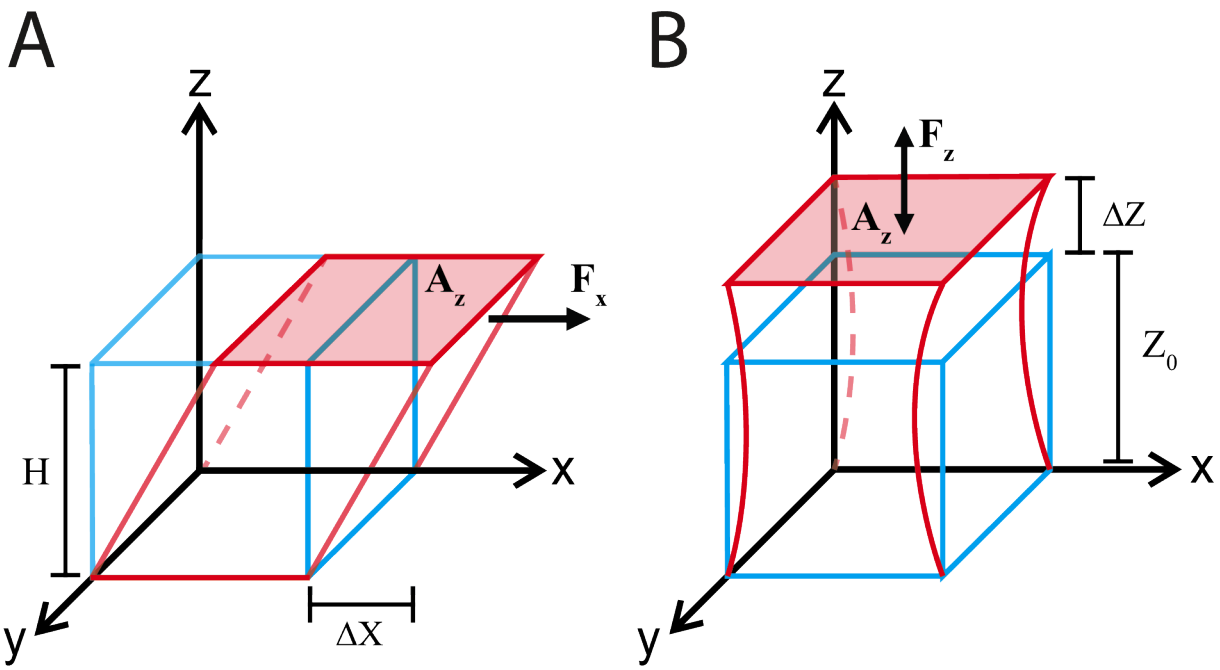

Figure 3.3: Rectangular objects subjected to shear forces (A), and uniaxial tensile and compressive forces (B).

normal to the $\hat{z}$ direction to which the force is applied [92]. This quantity provides an intensive measure of the force applied to the material in units of N/m^2, known as the Pascal (Pa). We also define a characteristic (dimensionless) extensional strain ϵ of the material, an intensive measure of deformation under a load, by

$$\epsilon = \frac{\Delta Z}{Z_0} \tag{3.2}$$

where ΔX is the change in length of the material under load, and X_0 is the materials natural length. Note that stress and strain are second-rank tensor quantities, $\overline{\overline{\boldsymbol{\sigma}}}$ and $\overline{\overline{\boldsymbol{\epsilon}}}$; here the scalar characteristic extensional stress and strain are diagonal components of these tensors: $\sigma = \left(\overline{\overline{\boldsymbol{\sigma}}}\right)_{xx}$ and $\epsilon = \left(\overline{\overline{\boldsymbol{\epsilon}}}\right)_{xx}$.

We can now use the relationship between stress and strain to understand and classify the mechanical behavior of materials. An ideal elastic material exhibits a linear relation between extensional stress and strain:

$$\sigma = E\epsilon \tag{3.3}$$

where E, the slope of the function, is the Young's modulus for uniaxial extensional deformations

[93]. The Young's modulus of a material represents how easily the material will deform under an applied compressive or tensile stress, and has units of Pa. It is important to note that above a critical value of stress, an elastic material reach its yield point, beyond which it will no longer deform in a linear way and return to its original state.

Alternatively, for an applied shear force on a material, we can define a characteristic shear stress σ as

$$\sigma = \frac{F_x}{A_z} \tag{3.4}$$

where F_x is the applied force in the $\hat{x}$ direction acting on a surface of area A_z normal to the $\hat{z}$ direction [92]. We also define a characteristic (dimensionless) shear strain γ of the material by

$$\gamma = \frac{\Delta X}{H} \tag{3.5}$$

where ΔX is the net displacement of the material parallel to the force on the top surface, and H is the nominal thickness of the material. In this case, the scalar characteristic shear stress and strain are off-diagonal components of the stress and strain tensors: $\sigma = \left(\overline{\overline{\boldsymbol{\sigma}}}\right)_{xy}$ and $\gamma = \left(\overline{\overline{\boldsymbol{\epsilon}}}\right)_{xy}$. As before, an elastic material exhibits a linear relation between shear stress and strain:

$$\sigma = G\gamma \tag{3.6}$$

where G is the shear modulus.

Materials may also behave as liquids. For ideal (Newtonian) viscous materials under shear deformation, a linear constitutive relationship between stress and strain rate holds:

$$\sigma = \eta\dot{\gamma} \tag{3.7}$$

where η is the shear viscosity of the liquid and $\dot{\gamma}$ is the shear strain rate.

Viscoelasticity

Of course, what was written above only applies for materials that are perfectly elastic or viscous. For viscoelastic materials, their stress response will reflect a combination of elastic and viscous properties. When a stress is applied, the elastic portion of the material responds immediately by storing energy from the deformation, and then releasing it when the stress is removed. For the viscous component, the added energy is dissipated through internal friction, which takes time [93]. The combination of these components then causes a nonlinear stress-strain curve during loading and unloading, and also causes there to be a delay between the stress and strain curves as a function of time (Figure 3.4).

To derive relevant quantities for viscoelastic materials, we can start with the simplest model, the Maxwell model, which describes a spring (the elastic component) in series with a dashpot (the viscous component) [92]. Here, we illustrate this for the case of shear deformations. This model is described with the following differential equation

$$\sigma + \tau\dot{\sigma} = \eta\dot{\gamma} \tag{3.8}$$

where $\tau = \eta/G$ is known as the Maxwell relaxation time. Equation 3.6 has a general solution of the form

$$\sigma(t) = \frac{\eta}{\tau}\int_{-\infty}^{t} e^{-(t-t')/\tau}\dot{\gamma}(t')dt' \tag{3.9}$$

However, this model only describes materials that have a single relaxation time, which does not accurately describe the majority of viscoelastic materials [92]. To account for this, the Maxwell model can be extended to include materials with a finite number or continuum of relaxation times. To do this, we define a continuum function, $H(\tau)$, which represents the distribution of all relaxation times for the material. Integrating over $H(\tau)d\tau$ would then account for all of the Maxwell elements inside the material contributing to its behavior. We can thus rewrite expression 3.9 using this as

$$\sigma(t) = \int_{0}^{\infty} \frac{H(\tau)}{\tau}\left[\int_{-\infty}^{t} e^{-(t-t')/\tau}\dot{\gamma}(t')dt'\right]d\tau. \tag{3.10}$$

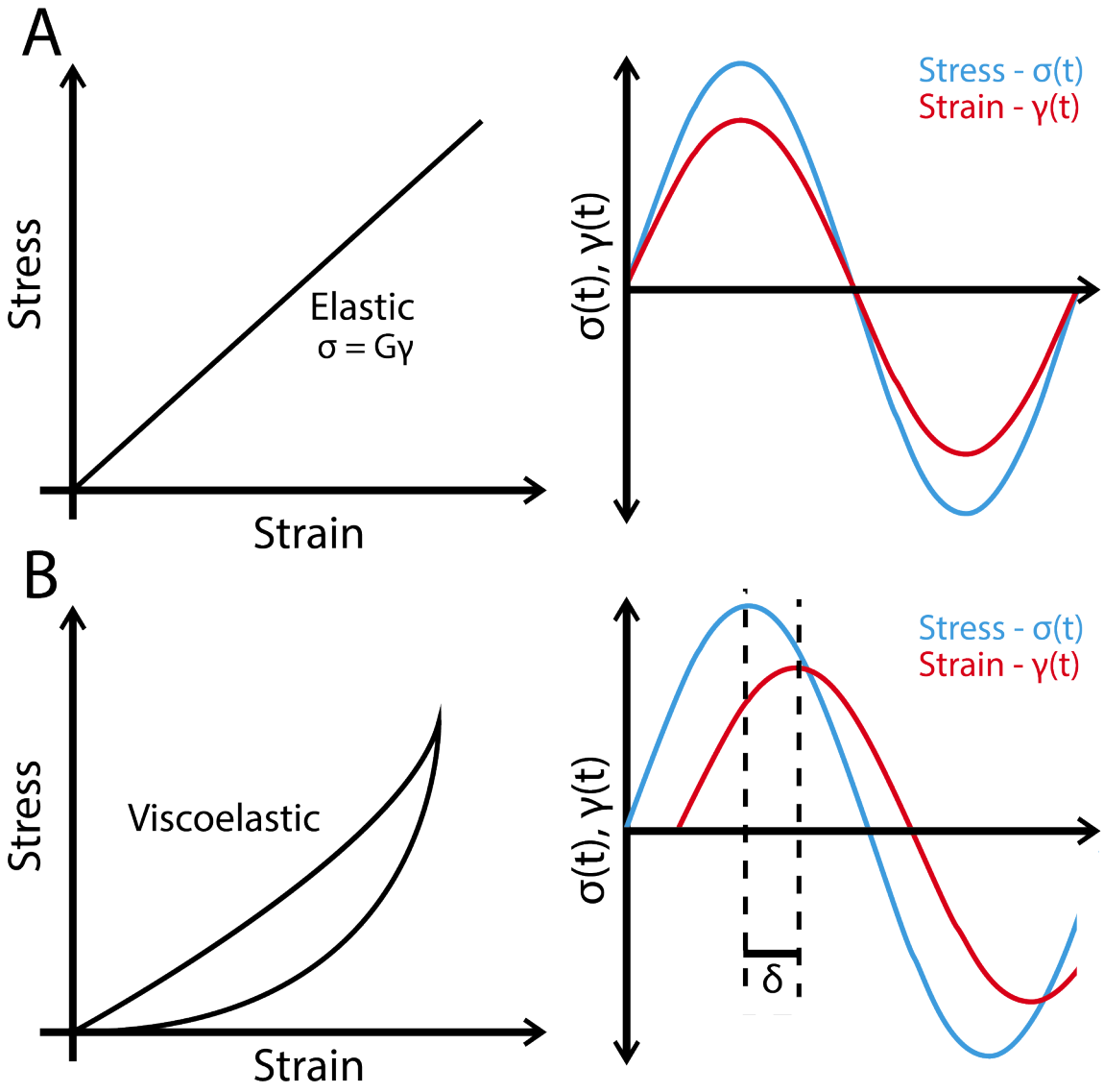

Figure 3.4: A: A loading cycle applied to a perfectly elastic material. The second plot shows the stress and strain functions as functions of time, where they are in phase with $\delta = 0$. B: A loading cycle for a viscoelastic material showing visible hysteresis in the cycle. The next plot shows the stress and strain curves with a noticeable phase difference $\delta > 0$.

One can now introduce the stress relaxation modulus of the system $G(t)$, defined by

$$G(t) = \int_0^\infty \frac{H(\tau)}{\tau} e^{-t/\tau} d\tau \tag{3.11}$$

which we can then use to rewrite the stress in a general form for linear viscoelasticity as

$$\sigma(t) = \int_{-\infty}^{t} G(t - t')\dot{\gamma}(t')dt'. \tag{3.12}$$

where the relaxation modulus $G(t)$ may come from more general models for viscoelastic materials.

To study a viscoelastic material, cyclic testing is often done, where the material experiences an applied strain at a fixed amplitude and frequency,

$$\gamma = \gamma_0 e^{i\omega t} \tag{3.13}$$

where γ_0 is the amplitude of the strain, ω is the frequency, and t is time. For small amplitude strains, resulting cyclic shear stress $\sigma(t)$ has the form:

$$\sigma(t) = \sigma_0 e^{i(\omega t + \delta)} \tag{3.14}$$

For small strain amplitudes, the formal relation between cyclic stress and strain can be obtained by using the form of $\gamma(t)$ from Eq. 3.13 in Eq. 3.12

$$\sigma(t) = i\omega\gamma_0 \int_{-\infty}^{t} G(t - t')e^{i\omega t'} dt' \equiv G^*(\omega)\gamma(t) \tag{3.15}$$

where the complex shear modulus $G^*(\omega)$ is defined by

$$G^*(\omega) = i\omega \int_0^\infty G(u)e^{-i\omega u} du \equiv G'(\omega) + iG''\omega) \tag{3.16}$$

Here, $G' = \mathrm{Re}(G^*)$ is the storage modulus and $G'' = \mathrm{Im}(G^*)$ is the loss modulus. The storage modulus is a measure of the elastic properties of the viscoelastic material, while the loss modulus is a measure of dissipation in the deformed material.

Alternatively, we can characterize the viscoelastic properties of a material using the the phase angle δ between stress and strain in a cyclic deformation protocol. By inserting Eqs. 3.13 and 3.14 into Eq. 3.15 and using elementary trigonometric identities, one obtains:

$$G^* = \frac{\sigma_0}{\gamma_0}\left(\cos(\delta) + i\sin(\delta)\right) = G' + G'' \tag{3.17}$$

Thus, we may conclude that the storage and loss moduli, respectively, can be written

$$G' = \frac{\sigma_0}{\epsilon_0}\cos(\delta), \tag{3.18}$$

$$G'' = \frac{\sigma_0}{\epsilon_0}\sin(\delta) \tag{3.19}$$

The phase angle can then be used to further classify the material. For an ideal elastic material, $\delta = 0$, resulting in $G'' = 0$, and the stress and strain are in phase. For an ideal viscous material, $\delta = 90°$ resulting in $G' = 0$, and the the stress and strain are $90°$ out of phase. When the phase angle is between $0°$ and $90°$, the material is viscoelastic, and can then be classified further as a viscoelastic solid or a viscoelastic liquid [94, 92]. For a viscoelastic solid we have the condition that $0° < \delta < 45°$, and for a viscoelastic liquid we have that $45° < \delta < 90°$ [94, 92].

The analysis for the viscoelastic response of a material to cyclic uniaxial compression/extension follows closely the case of cyclic shear deformation above. The principal results are those of Eqs. 3.12-3.19, with $\gamma \to \epsilon$ and $G \to E$.

To experimentally determine the viscoelastic properties of materials under cyclic deformation, we employed two standard rheology techniques. For the case of cyclic shear deformation, we used a rotational rheometer, in which a sample contained between two parallel plates is subjected to oscillatory rotation of the top plate while the bottom plate is held fixed (Fig 3.5A). The angular displacement and torque of the top plate as a function of time are recorded and used to infer the cyclic shear strain $\gamma(t)$ and stress $\sigma(t)$ in the sample. For the case of cyclic compressional deformation, we used a dynamic mechanical analyzer (DMA), in which a sample contained between two parallel plates is subjected to oscillatory compression by the up and down motion of the top plate while the bottom plate is held fixed (Fig 3.5B). The vertical displacement and force applied

by the top plate as a function of time are recorded and used to infer the cyclic compressional strain $\epsilon(t)$ and stress $\sigma(t)$ in the sample.

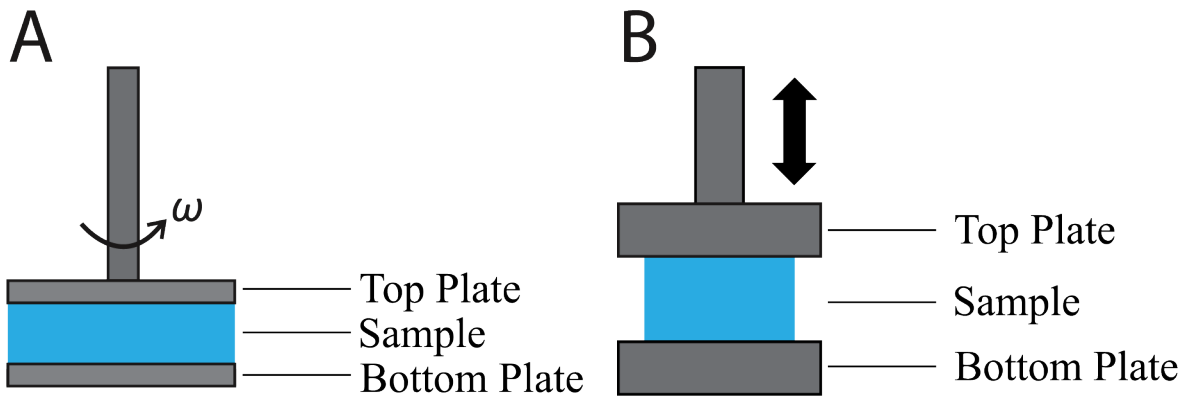

Figure 3.5: A: A representative drawing of a typical rotational rheometer setup with the sample sandwiched between an upper and lower plate. B: A representative drawing of a typical DMA setup with the sample sandwiched between an upper and lower plate.

In either case, two typical rheology protocols involve frequency and strain amplitude sweeps. Frequency sweeps measure complex moduli of the material as a function of the frequency of oscillation. Low frequencies test the material's ability to handle an applied force over large time scales, while high frequencies test the materials strength over short time scales. These tests are normally performed with a constant strain amplitude, specifically in its linear viscoelastic regime (LVER), where the material does not undergo any permanent deformation. Strain amplitude sweeps measure complex moduli of the material as a function of the applied cyclic strain amplitude at a constant frequency and test the materials ability to resist deformation with changing strain amplitude, allowing the mapping of the boundary of the LVER.

Atomic Force Microscopy

To characterize the substrates with a gradient in stiffness, we can no longer utilize the techniques that were described in previous section, as those were used to describe the bulk properties of homogeneous materials. For these, we may instead utilize atomic force microscopy (AFM), to characterize the spatial gradients. This technique utilizes a cantilever with a tip that is used to probe the surface of the material (Figure 3.6A), a process known as force spectroscopy. To make

force measurements of the sample, the AFM probe is first moved into position above the sample, and then lowered until it is in contact. The system utilizes a laser focused on the back of the probe where light reflects off and into a photodetector. This quantity is known as deflection, and it utilizes the position of the reflected light on the photodetector to measure the bending or displacement of the AFM probe. This data is then sent into a feedback system, which utilizes a piezoelectric stage to keep the AFM probe at a fixed height with respect to the sample.

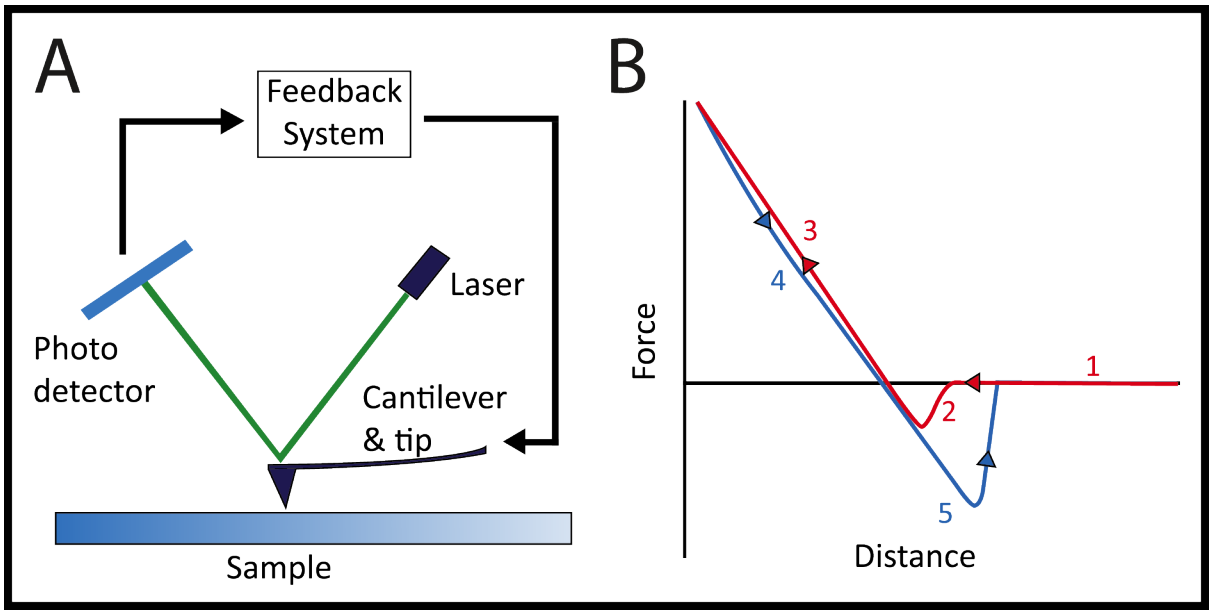

Figure 3.6: A: A schematic showing an AFM probe performing a measurement on a sample with the feedback system. B: A typical force distance curve for a soft sample showing the adhesive forces pulling the probe back towards the sample during retraction. The AFM probe approaching the sample is shown in red, while retraction is in blue.

To determine the modulus of the material, the AFM makes small indentations into the sample, where it can then record the force the sample exerts on the probe as a function of indentation depth [95]. This data can then be plotted and fit with a model to determine the modulus at that point on the sample. In Figure 3.6B, a typical force distance curve for a soft material is shown. In this figure there are five steps. In the first step, the probe approaches the sample. In the second step, the tip snaps into the sample, generally due to attractive interactions between the tip and sample. In the third step, the tip indents further into the sample, and the repulsive force exerted by the sample grows. In the fourth step, the maximum indentation depth has been reached, and the tip is now lifted away from the sample. In the final step, adhesive interactions between the

sample and tip attempt to pull the tip back down, until it is finally able to return to its original position above the sample.

To fit the data and determine the modulus of the sample in that local area, the Hertz model is commonly used [96]. This model was originally derived under the assumption that the tip was a sphere, and the sample is homogeneous and linearly elastic [97]. For an AFM probe that makes an indentation of depth h with a spherical tip of radius R, the resulting force curve can be fit with the following expression

$$F = \frac{4}{3}\frac{E}{1-\nu^2}R^{1/2}h^{3/2} \tag{3.20}$$

where E is the Young's modulus of the sample and ν is Poisson's ratio [96]. Furthermore, this expression also assumes that the indentation depth is much smaller than the radius of the probe.

For biological samples, which are often viscoelastic, the assumptions made for this model may not hold. However, the model has been shown to be accurate so long as the indentation depth is not greater than 10% of the sample thickness and >200nm [98, 99, 100]. Even so, modifications to this model have been made to describe different tip geometries. For soft samples, cone or pyramidal tips are often used as they offer higher spatial resolution than spherical tips, but still have some curvature at the tip that minimizes damage to the sample. For these tips, the Sneddon model was developed as an extension to the Hertz model, and accounts for the cone or pyramidal tip shape [96, 101]. This model can be fit to data utilizing a tip with a half angle θ with the following expression

$$F = \frac{2}{\pi}\frac{E\tan(\theta)}{1-\nu^2}h^2, \tag{3.21}$$

with the following expression used to calculate E:

$$E = \frac{\pi}{2}\frac{(1-\nu^2)F}{h^2 tan\theta}. \tag{3.22}$$

Besides the geometry of the tip, other factors including the frequency and spring constant of the AFM probe are important when performing force spectroscopy. The frequency of an AFM probe is its resonant frequency, and is important when using the alternating contact (AC) AFM imaging mode. This mode drives the probe at frequencies close to its resonant frequency to probe

the sample at a high rate, minimizing the contact time with surface of the sample. However, contact mode imaging is required for force spectroscopy, so the spring constant is of the probe is more important. The spring constant is a measure of how stiff the AFM probe is in units of N/m, and describes how much force is required to stretch or compress the spring. For soft samples, a low spring constant is essential, as it will minimize the force required to deform the cantilever and probe the sample. If the spring constant is too high, then the sample may become damaged.

The final parameter that must be accurately chosen for data fitting is the Poisson ratio (ν), described in the expression below

$$\nu = \frac{-\epsilon_t}{\epsilon_a} \tag{3.23}$$

where ϵ_t and ϵ_a denote the transverse and axial strain respectively. This constant is the ratio of transverse strain to axial strain in a stretched elastic body, offering a measure of the volumetric change as a material is compressed or stretched [102]. In many studies related to force spectroscopy on viscoelastic materials, this value is often assumed to be equal to 0.5, meaning that the material is incompressible. However, this may not be entirely accurate in many systems [103]. Polyacrylamide hydrogels have been found to have a Poisson ratio around 0.4 [104], and collagen hydrogels have been found to have a value between 0.35 and 0.45 [103, 105]. For perfectly elastic materials, where stress and strain are linearly related ν can be obtained from the shear and Young's moduli [102] by:

$$\nu = \frac{2G}{E} - 1. \tag{3.24}$$

However, this expression does not necessarily hold for viscoelastic materials, which often have nonlinear stress-strain relations. So, to calculate the Poisson ratio for a viscoelastic material, both the elastic and shear moduli must be determine in regimes of linear viscoelasticity. In particular, elastic moduli should be determined in a region with low hysteresis, often at low strain amplitudes. In practice, these moduli can be determined from the LVER, where their values are independent of strain amplitude.

3.3 Methods

3.3.1 Materials

EDC, NHS, riboflavin 5'-monophosphate sodium salt hydrate, SPS, genipin, 99% (3-Aminopropyl)triethoxysilane (APTES), 50 wt.% glutaraldehyde solution in water, silanization solution I (5% (dimethyldichlorosilane in heptane), 4-(2-Hydroxyethyl)piperazine-1-ethanesulfonic acid (HEPES), 2-(N-Morpholino)ethanesulfonic acid hydrate (MES), acrylamide, and N,N'-Methylenebis(acrylamide) were supplied by Sigma-Aldrich (Oakville, Ontario, Canada). 1X Phosphate buffered saline (PBS) was obtained from Gibco (Grand Island, NY, USA). Custom molds for hydrogel fabrication were created using Teflon sheets from McMaster Carr. PNP-TR-Au gold coated silicon nitride AFM probes were obtained from Nanosensors. A LZ4-40U600 UVA LED (365nm) was used for photocrosslinking. GYQ, GYQ-RGD, VB, and VB-RGD lyophilized collagen protein for UV and chemical crosslinking was synthesized by Dr. Fan Wan at the University of Ottawa.

Stock Solutions

Collagen solutions were prepared by dissolving lyophilized protein into 1X phosphate buffered saline (PBS) at the desired concentration. Stock solutions were prepared with only 80% of the desired final volume of PBS to allow for the subsequent addition of crosslinking agents and any extra PBS required to bring the solution to the final target concentration. These solutions were then vortexed, and left in a 4°C fridge until required. Stock solutions of riboflavin, SPS, were prepared in PBS at concentrations of 20mM and 50mM respectively, with the riboflavin solution requiring brief sonication to dissolve the solute.

Glass Coverslip Functionalization

18mmx18mm glass coverslips were first sonicated for 30min in acetone, and then washed several times with distilled water. Half of the coverslips were then silanized with a 5% dimethyldichlorosilane solution, to create the hydrophobic top coverslips for hydrogels. The other half were then

immersed in a solution of 0.1M NaOH for 1min. The coverslips were then air-dried, and subsequently immersed in a 5% solution of APTES in water for 15min. Each coverslip was then washed 20 times with distilled water to remove excess APTES. If any excess APTES is present, then an orange precipitate will form and the procedure must be restarted from the beginning. Following this, the coverslips were then covered with a 0.5% solution of glutaraldehyde in water. The functionalized coverslips were then used immediately or sealed under argon gas for up to one week.

Homogeneous Hydrogel Fabrication

For photocrosslinking, a small volume of riboflavin solution was added to the protein solution to the desired concentration. A small volume of SPS and PBS were subsequently added if required to reach the final concentration. This solution was then vortexed, and cast into a Teflon mold for crosslinking. The mold was then placed 10cm below the UV LED and irradiated for the desired amount of time. For chemical crosslinking, the desired amount of EDC, NHS, and or genipin were added to the protein solution kept at 4°C and thoroughly mixed. EDC and NHS were always added in an equimolar ratio. It is important to keep the protein solution cold during this process, as EDC/NHS crosslinking will begin immediately once introduced. Hydrogels to be used for rotational rheology or DMA were then cast into molds and allowed to crosslink overnight at 4°C shielded from light. Hydrogels for AFM were cast onto glutaraldehyde-APTES fixed coverslips and a hydrophobic coverslip was then placed on top to create a thin, flat layer of solution between the glass. Once crosslinked, the top coverslip was then removed, and PBS was added to the top to keep the sample hydrated.

DMA

DMA measurements were performed using a CellScale Univert mechanical testing system. All samples were first placed on the bottom plate, and then top plate was brought into contact with the sample to determine its initial position. This was determined by reading the live force display and recording when a positive normal force was measured. Tests were performed at a constant

frequency of 0.1Hz, under a compressive strain amplitude of 5%. This region was chosen as within this range the deformation of the samples is a linear function of applied force.

Rheology

An Anton Paar Physica MCR301 rheometer was used with a parallel plate configuration for all rotational rheological measurements. Hydrogels were glued to the surface of the top and bottom plates to prevent the sample from slipping. Frequency sweeps from 0.1 to 10 rad/s were performed to determine frequency dependence, while amplitude sweeps from 0.01% to 100% strain were done to determine the linear viscoelastic regime (LVER) at an angular frequency of 1 rad/s.

AFM

An Asylum Research MFP-3D-BIO AFM from Oxford Instruments was utilized to characterize the modulus gradients in hydrogels. Measurements were conducted using PNP-TR-Au pyramidal tip AFM probes. Initially, the AFM probe was calibrated to determine its spring constant. This calibration involved performing a single force curve on a hard calibration surface to determine the Inverse Optical Lever Sensitivity (InvOLS). This value relates the voltage change of the piezo driver to the displacement of the AFM probe in units of V/nm, thus allowing the displacement of the tip to be accurately monitored. Following this, the thermal calibration method was employed. By measuring the power spectral density of these thermal fluctuations, this method calculates the MSD of the cantilever's end. The spring constant k of the cantilever is then derived by relating the MSD to the thermal energy using the equipartition theorem. Following this, the calibration surface was then replaced with the sample, which is in an aqueous environment. The AFM probe was then lowered into the sample environment, and allowed to thermally equilibrate for 1 hour. The thermal method was then repeated, this time to recalibrate the InvOLS. When submerged in water, the frequency of the probe will change due to its interactions with the surrounding liquid, thereby changing the InvOLS.

Once calibration was complete, the AFM probe is lowered to the sample, and the sample is moved to the desired location. Figure 3.7 below shows qualitatively the description of the

following procedure. For the gradient hydrogels, the hydrogel was divided into a 10mm x 10mm grid, and the force map feature found in the AFM software Igor was used to take measurements. This feature takes individual force indentation measurements over a defined area, with an area of 100μm$\times 100\mu$m used for this analysis. Along the central y coordinates between 4mm-6mm, two force maps were taken in each 1mm step (dark grey squares), and all other 1mm steps had 1 force map (light grey squares). 2 force maps were taken in the middle as this is where the majority of the cell imaging would be done in later chapters. Perpendicular to the gradient direction, only one force map was obtained per mm. Each force map is further subdivided into a 5x5 grid with 1 force curve taken every 20 μm for 25 in total. Each force curve is then fit using Sneddon's modification of the Hertz model to determine the Young's modulus (E), and then all values are averaged together. The average modulus was then in one plotted in 1 of the 1mmx1mm squares on the heatmap to show the variation in substrate modulus across the material. To calculate the laterally averaged modulus ($\tilde{E}$), the effective modulus values obtained from each of the 10 force maps, taken perpendicular to the gradient, were averaged together. The Poisson ratio was calculated using Equation 3.22, utilizing the elastic and shear moduli derived from the homogeneous samples.

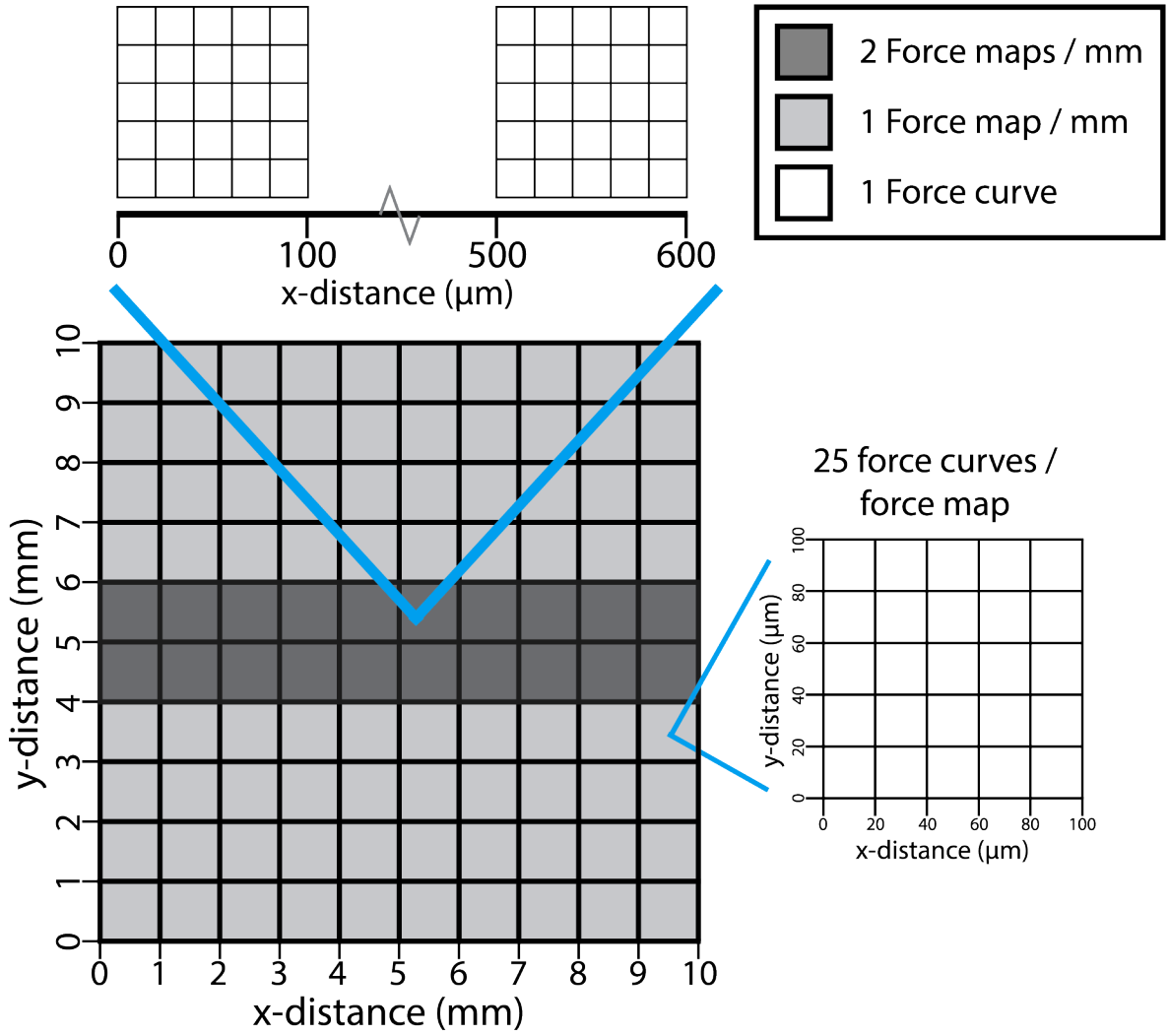

Figure 3.7: A qualitative representation of the AFM procedure. Hydrogels are subdivided into a 10mmx10mm grid, each of which has 2 force maps (dark grey), or 1 force map (light grey). Each force map is then subdivided into 100μmx100μm section which have 25 individual force curves performed within them. The modulus value plotted on the heatmap is then the average of all the force curves analyzed in that region.

3.4 Results and Discussion

We start by first determining the moduli of the protein hydrogels using DMA and rotational rheometry, to establish a baseline of the absolute range of stiffness we can obtain by altering the crosslinking method. Both versions of the collagen protein were tested, with and without the

addition of RGD. However, the insertion of the RGD sequence does not impact the chemical sites used for crosslinking, so there is a negligible difference in their mechanical properties. As such, the results for the version without RGD (VB), are shown below. Subsequently, we then explore the creation of stiffness gradients where we utilize photocrosslinking with masks and the diffusion of chemical crosslinkers.

3.4.1 Homogeneous Moduli Substrates

Riboflavin / SPS Substrates

The first method of crosslinking used to create homogeneous substrates was photocrosslinking with riboflavin using the GYQ protein with tyrosine residues. To characterize these materials, DMA tests were done at a frequency of 1Hz, with a strain amplitude of 10%. Rotational rheometry frequency and amplitude sweeps were also done to determine the frequency dependence and the LVER, as shown in Figure 3.8. Table 3.1 provides a summary of the storage moduli obtained from DMA and the rheology tests. The shear storage moduli reported in the table are the average values obtained the LVER of each tested sample.

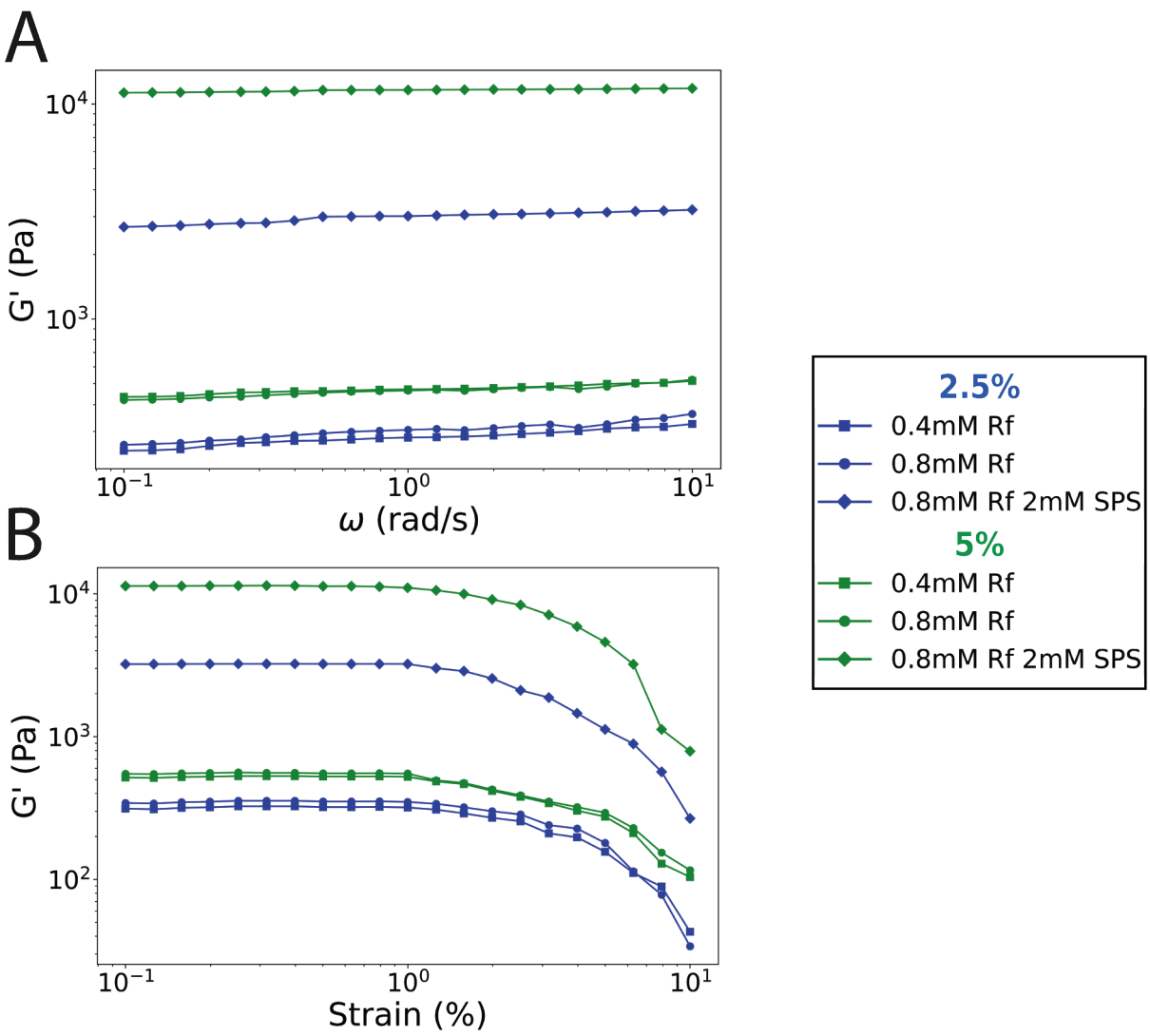

Figure 3.8: Frequency (A) and strain amplitude (B) sweeps of 2.5% and 5.0% protein hydrogels photo-crosslinked with riboflavin (Rf) and SPS. All plots are the average of N = 3 samples.

As shown in Figure 3.8A, the samples showed a minimal dependence on frequency over the tested range between 0.1rad/s and 10rad/s. In Figure 3.8B, amplitude sweeps at 1rad/s show the LVER is consistently between 0.1% and 1% for each of the tested samples. The use of only riboflavin for photocrosslinking resulted in a very weak gel, with storage moduli of only $E' = (760 \pm 60)$Pa and $G' = (260 \pm 80)$Pa for a riboflavin concentration of 0.4mM. Increasing the concentration of riboflavin to 0.8mM resulted in a minimal difference in the hydrogel moduli. The concentration of protein was then increased to 5.0%, and the storage moduli did increase, but not

	2.5% Protein		5.0% Protein	
Crosslinker	E' (Pa)	G' (Pa)	E' (Pa)	G' (Pa)
0.4mM Rf	760 ± 60	260 ± 30	1350 ± 130	470 ± 90
0.8mM Rf	780 ± 60	270 ± 30	1400 ± 130	500 ± 90
0.4mM Rf + 2mM SPS	9200 ± 300	3100 ± 200	33000 ± 1400	11500 ± 700
Poisson ratio (ν)	0.46 ± 0.02		0.43 ± 0.02	

Table 3.1: The shear and compressive storage moduli for GYQ protein hydrogels are shown for different concentrations of riboflavin (Rf) and SPS. All gels were irradiated with 365nm UV light for 10 minutes to ensure complete crosslinking. The results shown are the average of three samples. The Poisson ratio is the average of all samples for that concentration.

	2.5% Protein		5.0% Protein	
EDC / NHS Concentration	E' (kPa)	G' (kPa)	E' (kPa)	G' (kPa)
0.5%	1.5 ± 0.2	0.5 ± 0.2	5.6 ± 0.4	1.9 ± 0.3
1.0%	3.5 ± 0.2	1.2 ± 0.2	15.1 ± 0.5	5.2 ± 0.5
2.5%	9.8 ± 0.5	3.4 ± 0.4	51.6 ± 1.9	18.1 ± 1.2
5.0%	18.9 ± 0.8	6.5 ± 0.5	90.5 ±3.1	31.7 ± 1.7
10.0%	25.2 ± 1.1	8.7 ± 0.7	102 ± 4	35.3 ± 2.1
20.0%	26.8 ±1.3	9.1 ± 0.7	111 ± 5	38.2 ± 2.6
Poisson ratio (ν)	0.46 ± 0.02		0.45 ± 0.01	

Table 3.2: The shear and compressive storage moduli for VB protein hydrogels are shown for equal concentrations of EDC & NHS. All samples were allowed to crosslink for approximately 24h at 4°C to ensure complete crosslinking. All moduli are the average of N = 3 samples, and the Poisson ratio is the average of all samples with the same protein concentration.

by a large amount for the samples with only riboflavin. However, when SPS was introduced into the system, the moduli of the hydrogels had a dramatic increase for the same amount of riboflavin, with the 2.5% sample now having storage moduli of $E' = (9200 \pm 300)$Pa and $G' = (3100 \pm 200)$Pa and the 5.0% sample having storage moduli of $E' = (33000 \pm 1400)$Pa and $G' = (11500 \pm 700)$Pa. These results show that this crosslinking system can theoretically create a large range of moduli for creating gradient stiffness substrates. Furthermore, the calculated values of ν of 0.46 ± 0.02 and 0.43 ± 0.02 are consistent with values calculated for similar protein hydrogels [103].

EDC/NHS Substrates

Substrates were created using equal ratios of EDC/NHS to crosslink the VB protein. Results summarizing the storage moduli of 2.5% and 5.0% hydrogels are shown in Table 3.2, along with frequency and amplitude sweeps in Figure 3.9.

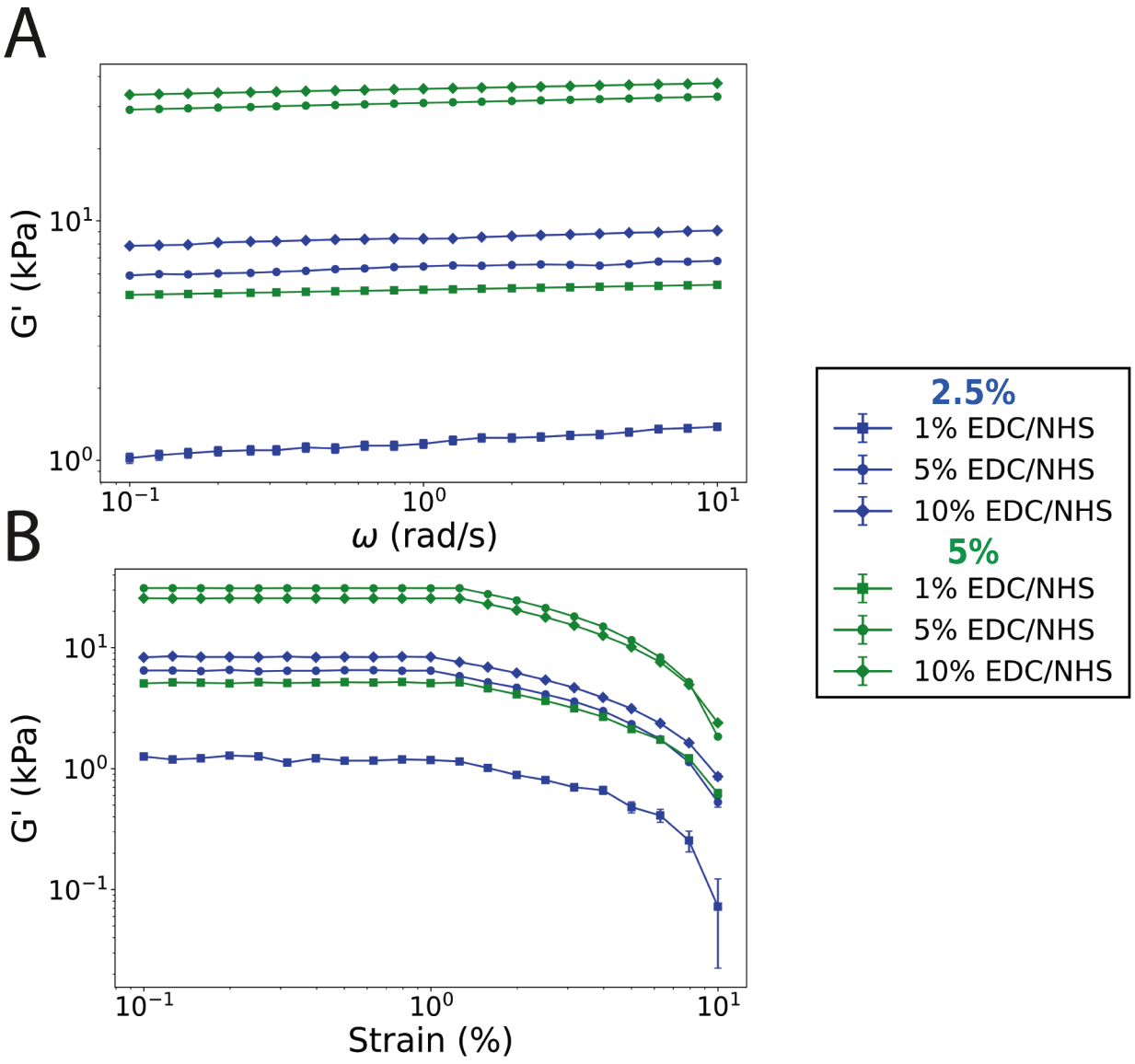

Figure 3.9: Frequency (A) and strain amplitude (B) sweeps of 2.5% and 5.0% protein hydrogels chemically crosslinked with EDC and NHS. The average of N = 3 samples are plotted for each curve.

As shown, the use of EDC and NHS to chemically crosslink the VB protein resulted in a large range of compressive storage modulus between $E' = 1.5$kPa and $E' = 111$kPa, depending on the concentration of crosslinkers and protein. For each protein concentration, these moduli monotonically increased with the concentration of EDC/NHS crosslinkers, with a plateau around 20%. The increase in moduli between the different protein concentrations was also nonlinear, with values of E' and G' typically being between 4-5 times larger in the 5% protein hydrogels than the 2.5% hydrogels. The calculated Poisson ratios were found to be 0.46 ± 0.02 and 0.45 ± 0.01 for the 2.5% and 5.0% protein concentrations respectively. The rheology revealed similar results to the substrates created with riboflavin. There was a minimal dependence on frequency, with the storage moduli of the samples increasing slowly with the angular frequency (Figure 3.8A). For the amplitude sweeps, the LVER of the 2.5% samples remained in the 0.1-1% range, while the 5.0% samples extended beyond that, to $\sim 3.0\%$ (Figure 3.9B).

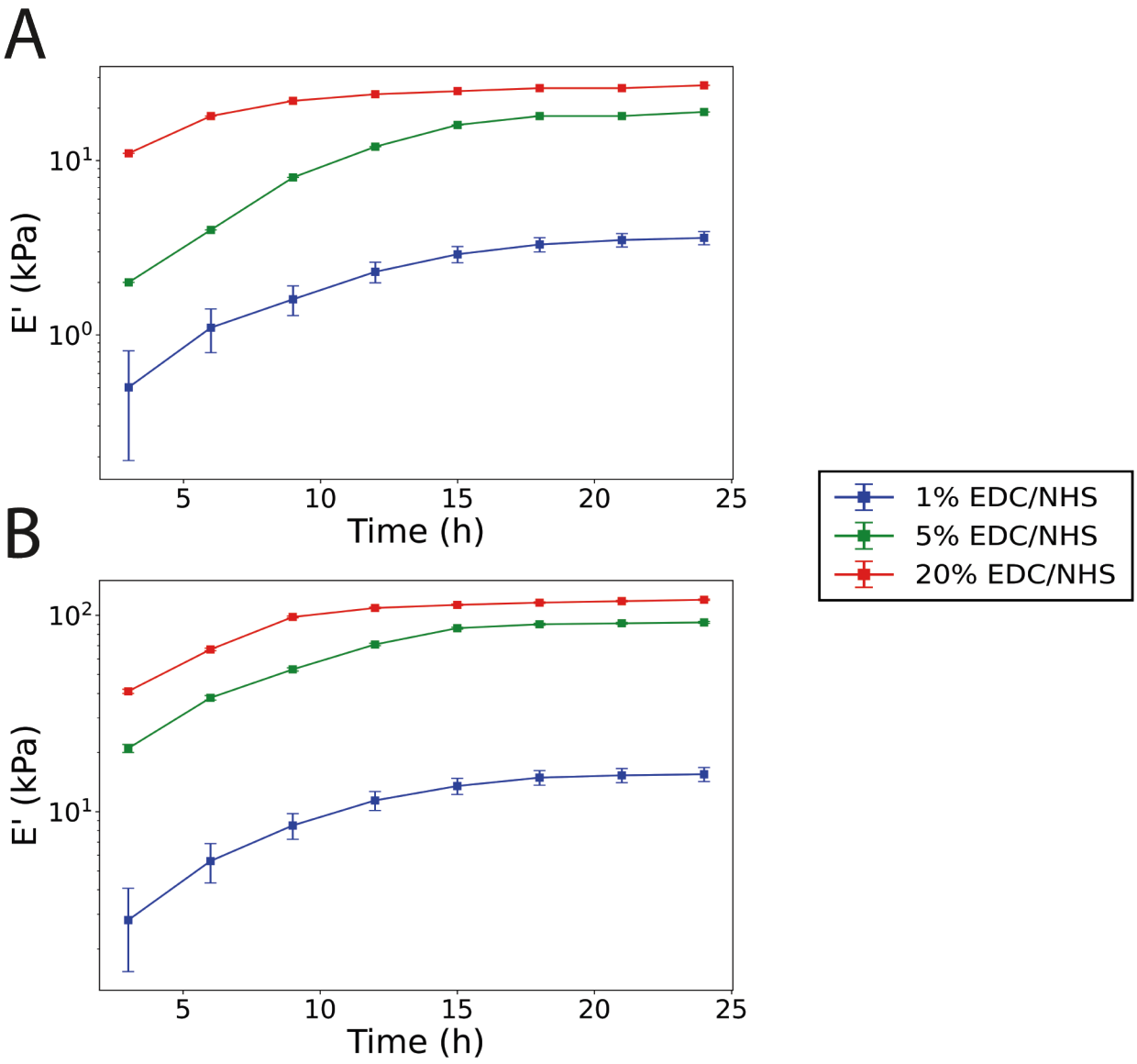

Figure 3.10: The time evolution of the storage modulus (E') obtained from DMA measurements at different times. Compression tests were done with an amplitude of 5% at a frequency of 0.1Hz. Results for 2.5% and 5.0% samples are shown in A and B respectively. All curves are the average of N = 3 samples.

To determine the time it takes to crosslink, DMA was used at different time intervals with different samples to see when the maximum modulus was reached, as shown in Figure 3.10. As expected, the higher concentrations of EDC & NHS took less time to crosslink than the lower concentrations. As well, these results show that allowing the gels to crosslink for 24 hours was

sufficient to ensure complete crosslinking for all samples.

Genipin Substrates

The final crosslinker tested for creating cell substrates was genipin. The results for their storage moduli are shown in Table 3.3, with frequency and amplitude sweeps shown in Figure 3.11.

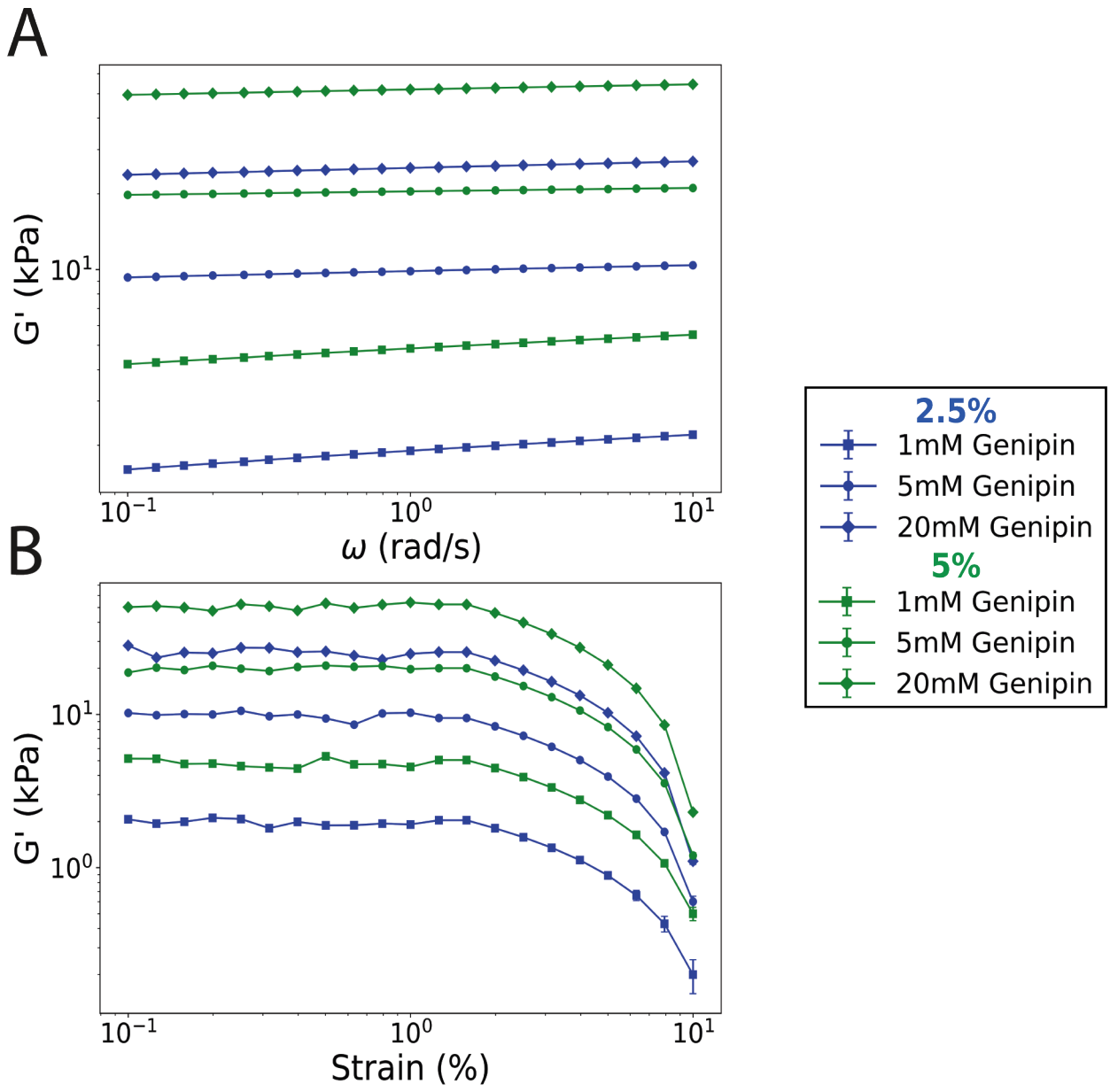

Figure 3.11: Frequency (A) and strain amplitude (B) sweeps of 2.5% and 5.0% protein hydrogels chemically crosslinked with genipin. The average of N = 3 samples are plotted for each curve.

The rotational rheometry was also consistent with the other samples using different crosslinkers. The storage moduli of all samples slowly increased over the tested angular frequency range from

	2.5% Protein		5.0% Protein	
Genipin	E' (kPa)	G' (kPa)	E' (kPa)	G' (kPa)
1mM	5.6 ± 0.5	1.9 ± 0.3	14.1 ± 1.2	4.8 ± 1.1
2.5mM	17.2 ± 1.4	5.9 ±0.9	33.4 ± 1.8	11.3 ± 1.4
5mM	28.9 ± 2.2	9.8 ± 1.6	58.9 ± 2.7	20.3 ± 1.9
10mM	50.3 ± 2.5	17.1 ±2.2	91.4 ± 4.1	31.7 ± 2.4
20mM	73.6 ± 3.7	25.1 ± 2.7	148 ± 7	51.2 ± 4.5
50mM	101 ± 6	34.9 ± 3.1	225 ± 9	78.3 ± 5.7
Poisson ratio (ν)	0.46 ± 0.02		0.45 ± 0.03	

Table 3.3: The shear and compressive storage moduli for VB protein hydrogels are shown for different concentrations of genipin. All samples were allowed to crosslink for 36 hours at 4°C. All calculated values are the average of N = 3 samples, and the Poisson ratio is the average of all values calculated for each protein concentration.

0.1-10 rad/s. Furthermore, the LVER of the 2.5% samples was once again between 0.1-1%, while the 5.0% samples extended a bit beyond this, to about 3.0%. The Poisson ratio for these samples were also identical to the samples crosslinked by EDC and NHS, at 0.46 ± 0.02 and 0.45 ± 0.03 for the 2.5% and 5.0% concentrations respectively. Following this, the dependence of the storage moduli of 2.5% and 5.0% samples on genipin concentration and time were also determined, as shown in Figures 3.12 and 3.13.

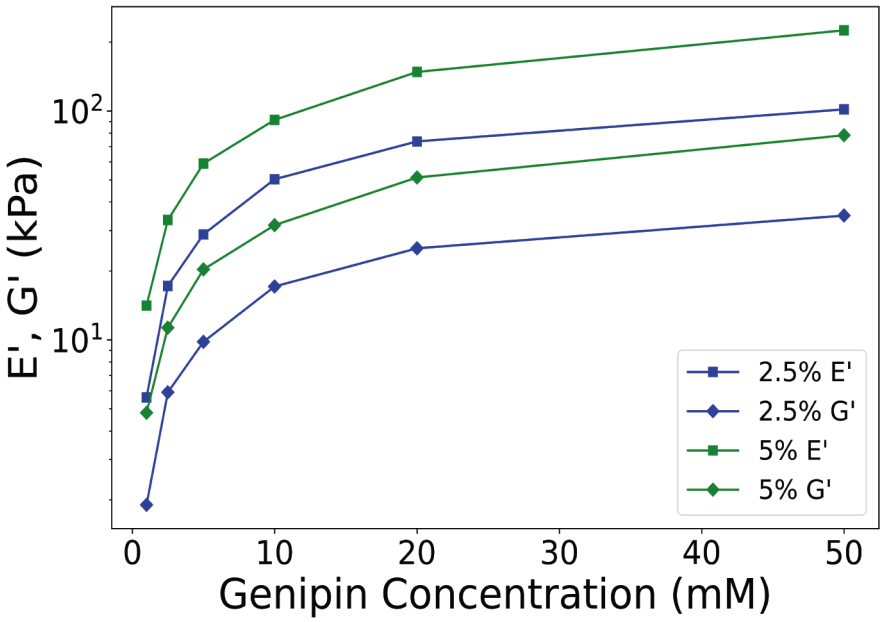

Figure 3.12: The storage moduli of 2.5% and 5.0% samples as a function of genipin concentration. The average of N = 3 samples are shown for each curve.

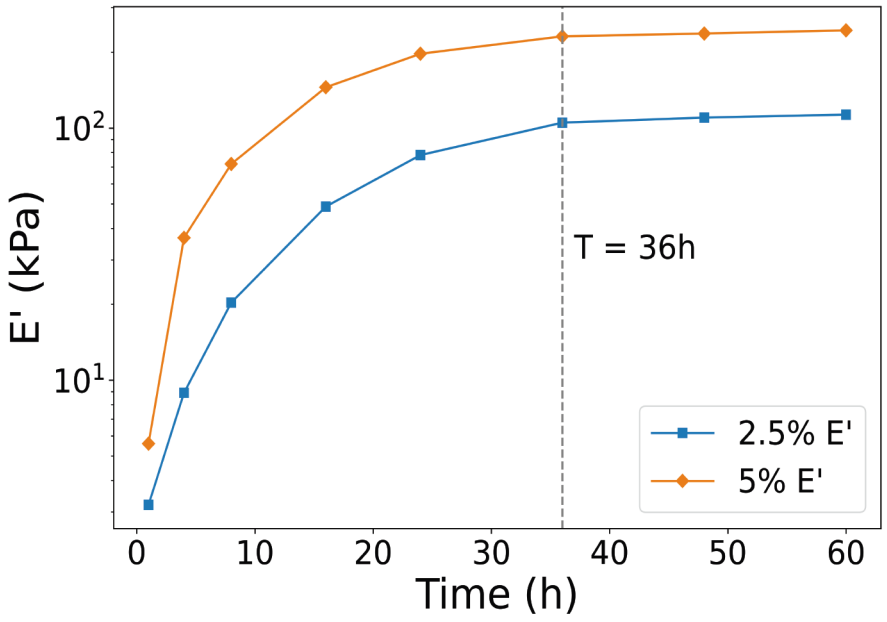

Figure 3.13: The storage moduli of 2.5% and 5.0% samples as a function of time. The average of N = 3 samples are shown for each curve.

Of the tested crosslinkers, genipin created the strongest hydrogel. At low molar concentrations, it was capable of producing hydrogels with moduli larger than the previously tested crosslinkers. The maximum modulus seemed to be achieved around a concentration of 50mM for both protein concentrations studied, as shown in Figure 3.12. However, genipin did take considerably longer to react than the other methods, as shown in Figure 3.13, where it took upwards of 36 hours for the modulus to reach a plateau for both of the tested protein concentrations. Ultimately though, the ability to produce substrates of higher moduli than the other crosslinkers made it the key crosslinker for producing a wide range of moduli. By varying the protein & genipin concentration and the crosslinking time, substrates of compressive storage modulus between 5.6kPa and 225kPa could be fabricated, larger than the range possible with the other crosslinkers.

3.4.2 UV Light Gradient Modulus Generation

Following the characterization of the homogeneous modulus substrates, the focus then turned to fabricating gradient modulus substrates using the crosslinkers from the previous section. The first method of creating gradient modulus substrates utilized a printed filter with a greyscale gradient

printed onto it with a range of 0-70%. A protein solution would receive a variable dose of UV light when the filter was placed on top. To do this, the protein solution was cast onto a glass coverslip, where it was then sealed off with a cover to prevent evaporation. The filter was then placed over the solution on top of the cover, and placed underneath the UV diode at a distance of 10cm. The protein solution was then irradiated for 10 minutes, which then created a gradient in the substrate modulus as every area of the solution received different doses of UV light. The results for a 10x10mm sample at 2.5% and 5.0% protein solution with 0.8mM riboflavin and 2mM SPS are shown in Figure 3.14.

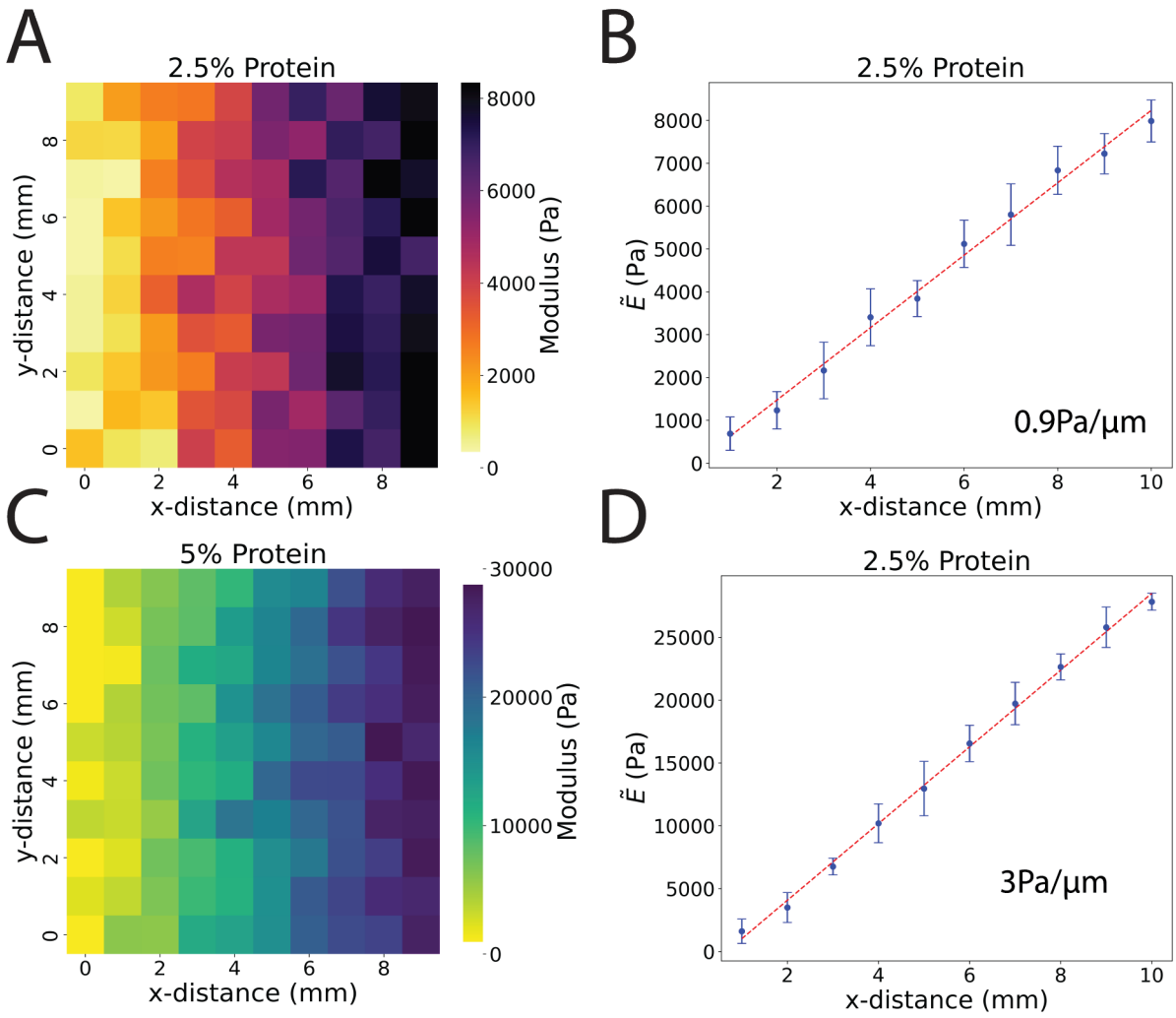

Figure 3.14: Heatmaps and the average modulus perpendicular to the gradient ($\tilde{E}$) for 2.5% and 5.0% samples crosslinked with 0.4mM riboflavin and 2mM SPS with a 0-70% filter and 10 minutes of exposure. A: The heatmap for the 2.5% sample. B: $\tilde{E}$ vs distance for the sample in A. C: A heatmap for the 5.0% sample. D: $\tilde{E}$ vs distance for the 5.0% sample in D.

As shown, a gradient in substrate modulus was successfully created utilizing photocrosslinking with riboflavin and SPS. Substrates were created that had a gradient in their modulus of approximately 0.9Pa/μm and 3Pa/μm for the 2.5% and 5.0% substrates respectively. As well, this method also resulted in linear gradients from the soft to stiff end of the hydrogel, as shown in Figure 3.14 B and D, which shows the average modulus over the 10mm range perpendicular to the gradient. Another concern when creating gradient substrates is simultaneously generating a significant height differential between the opposite stiffness ends of the substrate. This is due to

the differences in swelling that can occur in hydrogels of different moduli. For a hydrogel with a low degree of crosslinking, there are fewer bonds between the polymer chains, allowing more space for water molecules to penetrate and interact with the polymer network. The polymer chains can move thus more freely, resulting in greater water absorption and swelling. While the opposite would be true for hydrogels with more crosslinking, as the polymer chains would have more bonds restricting their movement thus allowing less water into the gel. To confirm that there were no significant height differences throughout the hydrogel, we used the AFM to measure the height of the sample from the stiff to soft end of the samples. As shown in Figure 3.15, there is a minimal height difference across the length of the hydrogel for both the 2.5% and 5.0% samples. This height difference corresponds to approximately $3\mu m_h$/mm and $14\mu m_h$/mm for the 2.5% and 5.0% samples respectively, where μm_h is the change in height of the substrate. This value is quite minimal when compared to the size of an individual cell (40μm - 80μm), and the distances that they travel over the course of 24 hours (100-500μm).

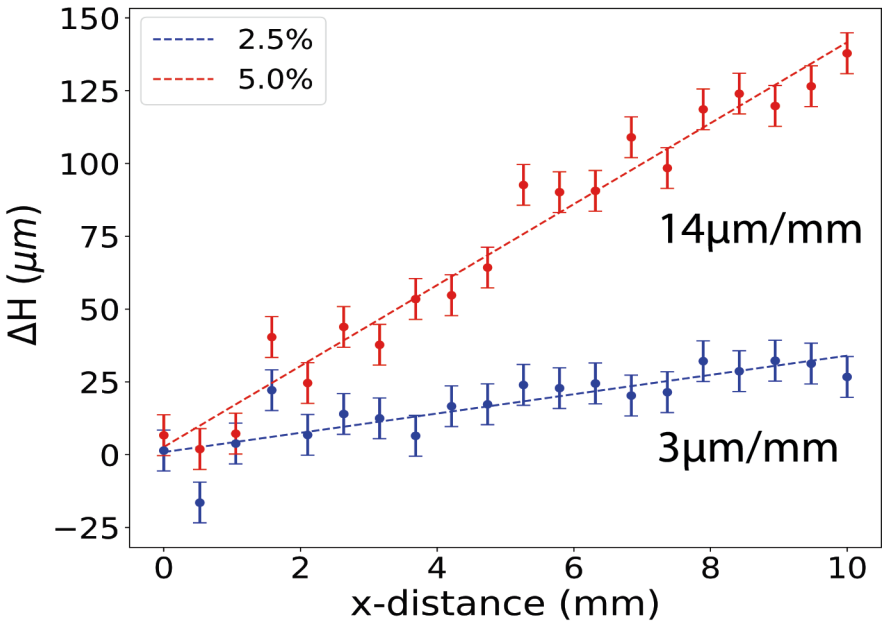

Figure 3.15: The height differential from the stiff to soft end of 2.5% and 5.0% hydrogels created by photocrosslinking.

The final test with these substrates was to compare their moduli at room temperature and at 37°C, as this is the temperature they would be at when cells are added to them. When this was

done, we found a major issue with these hydrogels when they were placed into the cell incubator and given time to equilibrate. After being in the incubator, the substrates seemed to melt, as the storage modulus of the sample would decrease dramatically. The table below shows the moduli of these substrates before and after leaving them in the cell incubator. As shown, all of the gels created with both riboflavin and SPS would lose their strength after being in the incubator. Interestingly, the value of the storage modulus after being in the incubator was roughly the same as the hydrogels that had been made with only riboflavin. This behavior indicates that the incubator environment was disrupting the crosslinks created by the SPS, but not those created by only the riboflavin. This result leads us to believe that there is an additional transient crosslinking mechanism for SPS does not involve formation of dityrosine bonds, as these are strong covalent bonds that would be unlikely to break by the increase in temperature.

To test this, we qualitatively observed what would happen if SPS was added to a protein solution without riboflavin and exposed to UV light. When we did this, there was no noticeable crosslinking. However, when SPS was added to a protein solution and incubated overnight, the SPS crosslinked the hydrogel without any UV light. When this hydrogel was added to the incubator, it would then irreversibly melt. This indicates that the SPS was crosslinking the protein on its own, rather than enhancing the activity of the riboflavin photocatalyst. This result was further corroborated by adding riboflavin and SPS to 0.4% (m/V) Type 1 rat tail collagen and exposing it to UV light. Normal collagen does not contain many tyrosine residues, and thus if riboflavin / SPS crosslinking worked by forming dityrosine bonds, then they would be very minimal crosslinking with this collagen, especially due to its low concentration. However, the opposite occurred, and a crosslinked gel formed, which would then irreversibly melt when placed into the cell incubator.

Other means of stabilizing these hydrogels after UV exposure were tested, however they either did not stop the breaking of the SPS crosslinks or they would remove the gradient generated in the substrate. Due to this, the use of riboflavin and SPS as crosslinkers had to be abandoned and other options were explored.

3.4.3 Diffusion Based Gradient Generation

EDC/NHS Diffusion

With the generation of gradients by photocrosslinking no longer a reliable option, we then explored using the chemical crosslinkers EDC and NHS to create stiffness gradients. For these substrates, we used the protein VB as GYQ was no longer required. We began by creating a protein solution with equal concentrations of EDC and NHS, then cast it onto glass coverslips. This was allowed to crosslink overnight, forming a soft, uniform modulus hydrogel. Following this, we introduced a reservoir of concentrated EDC/NHS solution, allowing it to diffuse through the hydrogel to create a stiffness gradient. The first aspect of this method we tuned was the diffusion time. To halt crosslinking, the reservoir was removed, and the sample was quickly rinsed multiple times to remove excess EDC and NHS.

Figure 3.16 shows the time evolution of multiple 5% VB hydrogels crosslinked by EDC and NHS diffusion. These hydrogels were first crosslinked with 0.5% EDC and NHS and allowed to crosslink overnight before adding a 20% EDC/NHS reservoir. Each plot represents a separate sample at different times. The curves shown are the laterally averaged modulus along the hydrogel perpendicular to the gradient. Table 3.4 summarizes the results for these gradient substrates.

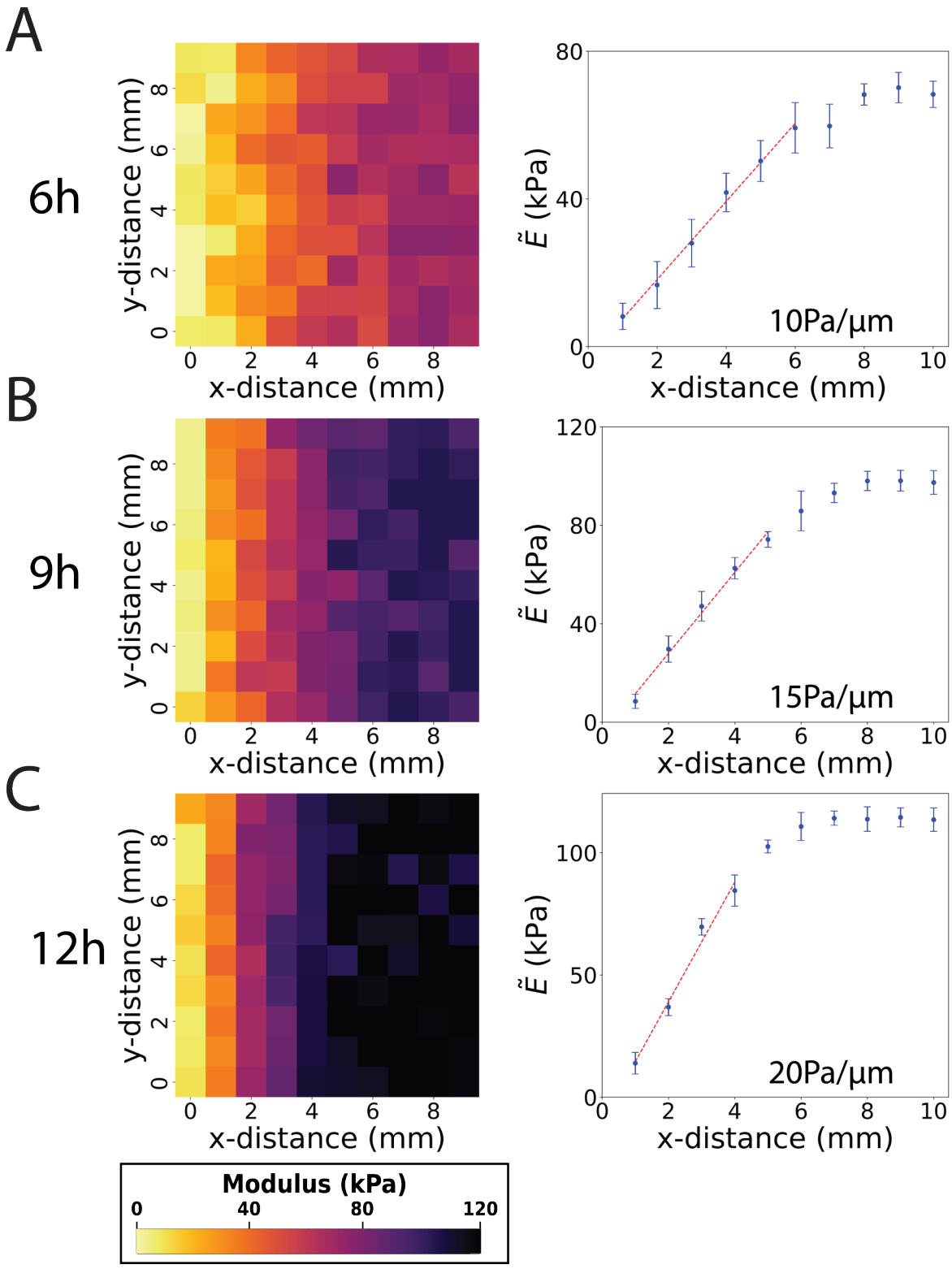

Figure 3.16: The time evolution of the modulus of 5% VB hydrogels crosslinked by EDC/NHS diffusion. Heatmaps after 6, 9, and 12 hours are shown in A, B, and C respectively, with a corresponding plot of $\tilde{E}$ vs time. The magnitude of the gradient is displayed on each plot.

2.5%			
Time (h)	Soft Region (kPa)	Stiff Region (kPa)	Gradient Strength (Pa/μm)
3	2	11	1
6	3	17	1.4
9	5	22	1.5
12	7	29	1.8
5.0%			
Time (h)	Soft Region (kPa)	Stiff Region (kPa)	Gradient Strength (Pa/μm)
3	8	51	5
6	9	70	10
9	15	98	15
12	17	115	20

Table 3.4: 2.5% and 5.0% substrates created through EDC/NHS diffusion. Samples were homogeneously crosslinked with 0.5% EDC/NHS, with the gradient created with a 20% reservoir. The gradient strengths are obtained from a linear regression in the linear regions of the samples.

As shown, this method creates gradient substrates with nonlinear gradients. At the stiffer end, the modulus gradually increases until it reaches a plateau at longer diffusion times. At the soft end, the modulus increases at a slower rate. This behavior likely occurs because the diffusion of the crosslinkers from the stiffer end slows as the sample becomes more crosslinked. This gradually slows the diffusion of the crosslinkers to the soft end over time. However, the regions from the soft end towards the middle are approximately linear, allowing us to halt the diffusion of the crosslinkers and study cell motion in these linear regions. By performing a linear regression in these linear regions, we achieve different gradient strengths between 5 Pa/μm and 20 Pa/μm, depending on the diffusion time. While the region available for studying cells becomes smaller with higher gradient strengths, it remains sufficient for most studies. One issue with this method is that creating the highest gradient strength increases the modulus at the soft end to above 10 kPa, making it unsuitable for studying cell motion in the softest regions.

Following this, gradient substrates with 2.5% protein concentration were created using the same procedure. The range of stiffness and gradient strength created by these substrates was lower, as summarized in Table 3.4.

We also confirmed with these samples that no significant height differentials were created due to the difference in crosslinking density across the sample. The height across the samples with the largest change in modulus was measured in the linear gradient region to see if any large height

differentials were present (Figure 3.17). The height average change in height across the 2.5% and 5.0% samples were found to be $5\mu m_h$/mm and $12\mu m_h$/mm respectively. These values are small, and would be unlikely to affect a cell's motion in any way.

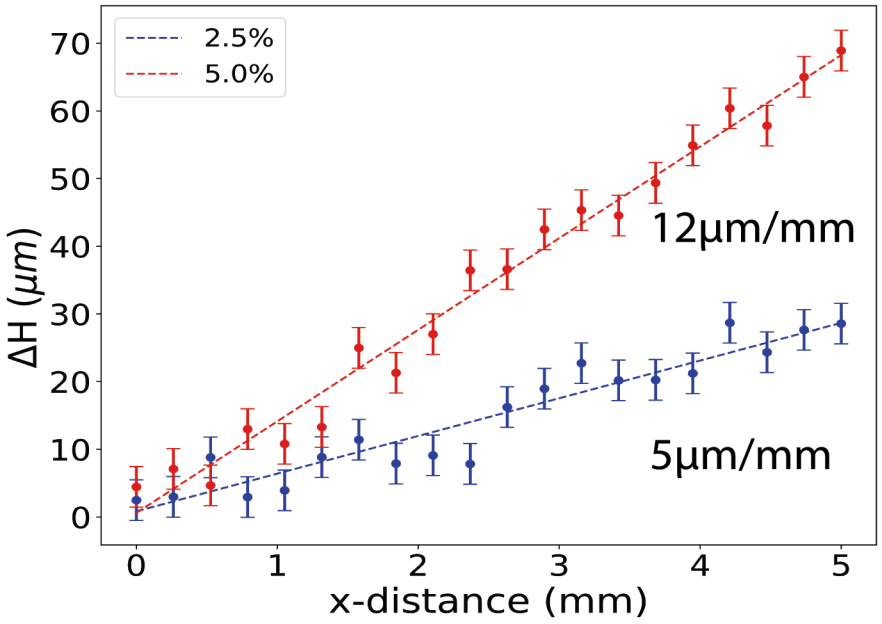

Figure 3.17: The height differential from the stiff to soft end of 2.5% and 5.0% hydrogels created with EDC and NHS diffusion.

As summarized in Table 3.4, using a protein concentration of 2.5% created lower gradient strengths. However, the softest regions were lower than those found in the 5% samples, allowing for the characterization of cell motion in these soft regions. Although large gradient strengths could not be created, these substrates enable us to establish a minimum gradient strength for these cells and determine how cells respond to weak modulus gradients.

Genipin Diffusion

Following the use of EDC and NHS, we then attempted to create gradients with genipin due to its low cytotoxicity, slow crosslinking rate, and the large range of moduli it could create. These samples were created using a similar method as the EDC/NHS samples. The samples were first crosslinked with 0.5% EDC/NHS and allowed to crosslink for 24 hours at 4°C. A concentrated genipin reservoir was then introduced at one end, and allowed to diffuse through the sample. The

results of 5.0% samples with a 50mM genipin reservoir are shown in Figure 3.18. Due to the slower reaction rate of genipin, measurements were done on the samples at 6 hour intervals. A summary of the results from the 2.5% and 5.0% samples are shown in Table 3.5.

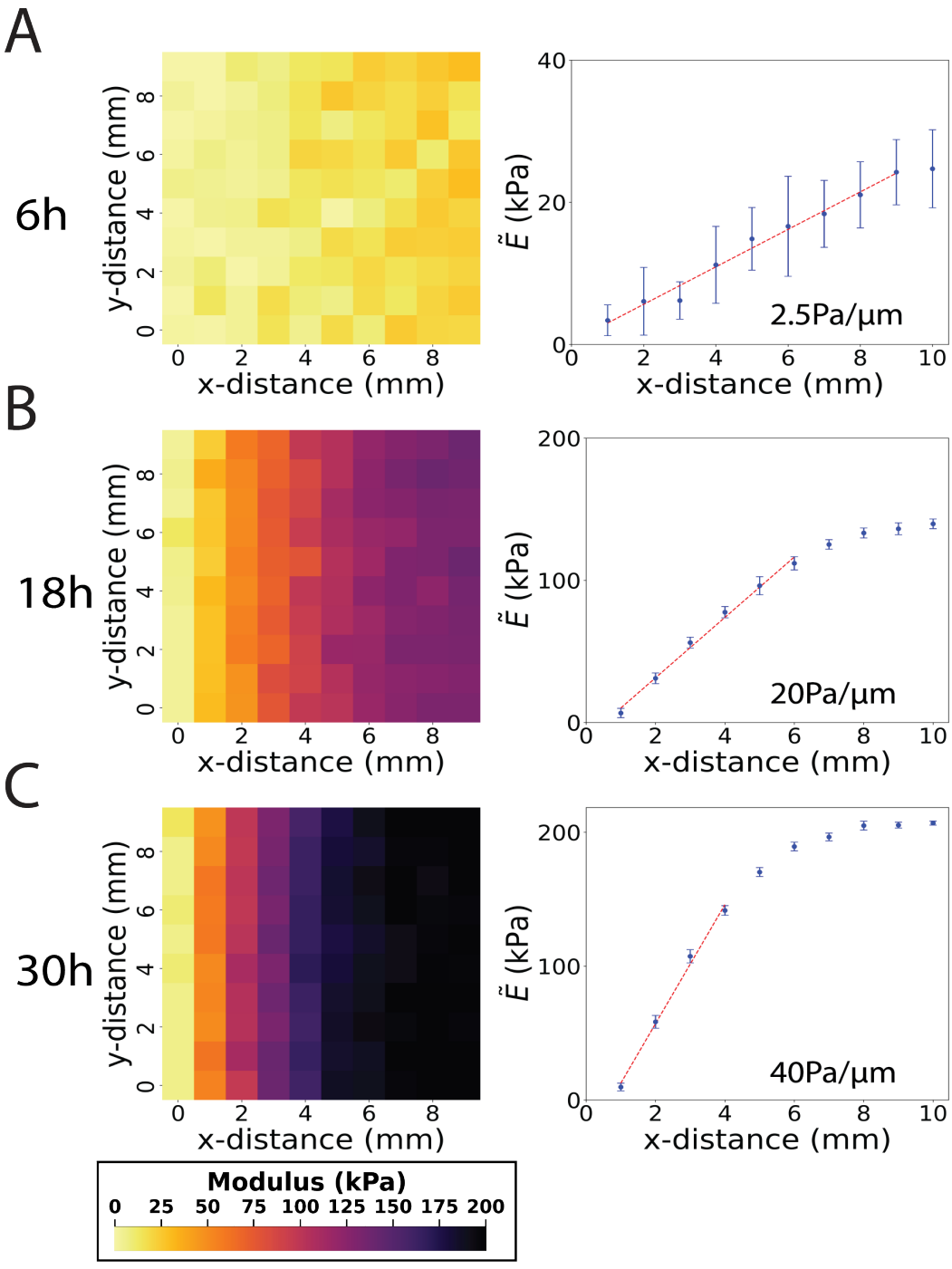

Figure 3.18: The time evolution of genipin crosslinker diffusion through 5% samples with a 50mM reservoir. AFM Heatmaps of samples after 6, 18, and 30 hours are shown in A, B, and C respectively, with a corresponding plot of $\tilde{E}$ vs time.

2.5%			
Time (h)	Soft Region (kPa)	Stiff Region (kPa)	Gradient Strength (Pa/μm)
6	1	14	1
12	2	21	1.5
18	3	41	3
24	4	75	8
30	6	90	10
5.0%			
Time (h)	Soft Region (kPa)	Stiff Region (kPa)	Gradient Strength (Pa/μm)
6	5	25	2.5
12	7	85	10
18	8	140	20
24	9	190	35
30	11	210	40

Table 3.5: 2.5% and 5.0% substrates created through genipin diffusion with a 50mM reservoir. Samples were first homogeneously crosslinked with 0.5% EDC/NHS, followed by the diffusion of genipin. The gradient strengths are obtained from a linear regression in the linear regions of the samples.

Similar to the gradients created through EDC & NHS diffusion, the resulting samples had nonlinear behavior in their stiffness, with a plateau in their moduli occurring in the stiffer regions of the samples. A benefit of using genipin over EDC/NHS was that larger gradient strengths could be created. As well, the soft regions consistently had a lower modulus than the large gradient strength samples created with EDC and NHS. This is likely due to the differences in the crosslinking mechanisms between these samples. EDC and NHS do not integrate themselves into the final structure of the sample, and are able to continue diffusing and crosslinking. Whereas genipin integrates itself into the proteins structure in the final step of crosslinking, which prevents it from diffusing afterwards. So, with genipin crosslinking the diffusion of genipin is slowly decreasing with time due to both the affects of the crosslinks creating a restrictive network and the concentration of genipin available to react decreasing. We also confirmed that these substrates do not have any significant changes in height due to differences in swelling. As shown in Figure 3.19, the rate at which the height of the sample was increasing was minimal for each concentration, at $6\mu m_h$/mm and $13\mu m_h$/mm for the 2.5% and 5.0% concentrations respectively.

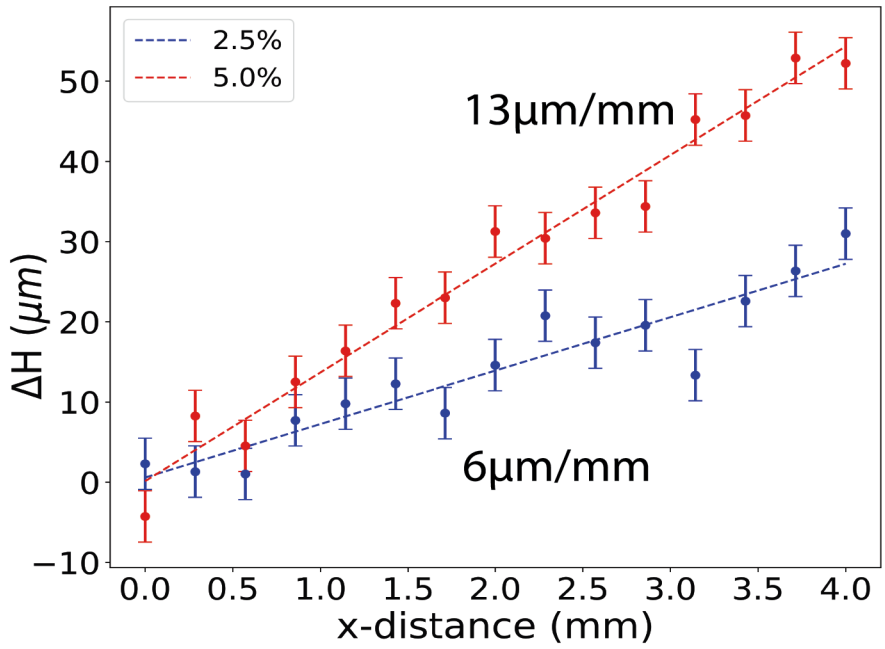

Figure 3.19: The height differential in the linear region of the samples from the stiff to soft end of 2.5% and 5.0% hydrogels created with genipin diffusion.

Due to the wide range of gradient strengths from 1-40 Pa/μm, and the large range of absolute stiffness that can be studied, the samples created by genipin diffusion are the best candidate for cell motility studies. Furthermore, these substrates did not have any noticeable degradation or structural changes when acclimated to the environment that cells require.

3.5 Conclusion

To investigate the durotactic behavior of cells, substrates are required to have a gradient in their modulus that is discernible across the length of their body. The purpose of these studies was to fabricate substrates that are biologically relevant to then study the durotactic behavior of cells.

To create these substrates, we first attempted to use a bio-mimetic collagen protein with additional tyrosine residues to facilitate the formation of dityrosine crosslinks. We utilized the crosslinkers riboflavin and SPS, that when exposed to UV light, will create dityrosine links and form a hydrogel. By using a photomask, we successfully created linear stiffness gradients with

different strengths. However, when they were placed into a cell culture incubator, the samples would degrade, meaning they could not be used for cell motility experiments. While the exact reason for this is still not clear, we hypothesize that the use of SPS created transient crosslinks that were not thermally stable.

Following the creation of substrates using photocrosslinking, we then attempted to make substrates using the diffusion of EDC and NHS crosslinkers. We utilized a high concentration reservoir of the crosslinkers at one end of the sample, and then varied the allowed diffusion time to successfully create samples with different gradient strengths from 1-20Pa/μm. Furthermore, these samples are stable in cell culture environments. While the gradients were not linear from end-to-end, all of them did have linear regions that were sufficient to study cell motion. However, the samples with the largest gradient strengths also raised the modulus of the soft end above 10kPa. Some cancerous cell lines have been previously shown to have the strongest durotactic motion in regions below this value [24].

The final method for creating these substrates was the diffusion of genipin. This crosslinker was slower to react than EDC and NHS, but it created substrates with a larger range of moduli, up to 220kPa. Using a reservoir of genipin, substrates with a range of gradient strengths were created from 1-40Pa/μm depending on the allowed diffusion time and crosslinker concentration, a larger range than those created by EDC and NHS diffusion. While nonlinear behavior was seen in the gradient, linear regions were created which could be used for studying cell motion. Furthermore, the soft end of these samples were consistently below 10kPa. So, due to the larger range of gradient strengths and regions of absolute stiffness, this method was optimal for creating substrates for studying durotaxis.

Chapter 4

Cell Motion on Homogeneous Substrates

The section of this chapter related to cell behavior on silicone substrates adapted from: Clugston, J. Fox, S., Harden, J.L., Copeland, J. A role for the formin FMNL2 in the response of melanoma cells to substrate stiffness, submitted to *BMC Molecular and Cell Biology*.

4.1 Introduction

Cell motion has been shown to be dependent on the stiffness of the substrate they reside on. Their morphology and motility can change depending on the mechanical properties of their environment [106]. Previous studies have indicated that cell area, or how spread out they are, will often increase on stiffer substrates due to the formation of focal adhesions [106, 49, 107]. As described in chapter 2, the formation of focal adhesions is dependent on the generation of tensile forces with the substrate, with stiffer substrates facilitating larger forces [108, 109, 8, 110]. The increase in force generation leads to an increase in focal adhesion formation, which is often cited as the reason for morphological changes. The dependence of focal adhesion formation on substrate stiffness thus impacts cell motility, as the primary mechanisms for cell motion involve the focal adhesion formation and turnover [108]. As described previously, motor clutch theory predicts that cells will move in the direction that maximizes force generation with the substrate. In the case of positive durotaxis, this would be in the direction of increasing substrate stiffness. However, some cells may not achieve maximum force generation on the stiffest areas of the substrate, but rather at an

optimal stiffness region [25], as is the case for negative durotaxis observed for cells on substrates that are stiffer than their optimal value.

To sense their environment, cells utilize actin-based protrusions that probe their environment in a process called mechanosensing. This process is dependent on many different proteins, and one specific group are formin proteins. These proteins are involved in actin polymerization as well as the formation of F-actin fibers [55, 56, 57, 58, 59]. Specifically, the formin FMNL2 is linked to the formation of filopodia in melanoma and other cancerous cell lines [59, 58]. Furthermore, FMNL2 is also linked to the formation of lamellipodia, and the forces they can exert on their environment in melanoma cells [64]. These observations suggest that FMNL2 is also linked to the formation of cell-cell adhesion sites and focal adhesion formation [61, 62].

To shed more light on the role of substrate stiffness in melanoma cell motility, we characterized the behaviour of A2058 human melanoma cells plated on substrates with biologically relevant moduli. The substrates utilized were (1) fibronectin-functionalized silicone materials and (2) bio-mimetic collagen hydrogels with sequence embedded RGD integrin binding sites. We found that A2058 cells adopted more elongated morphologies with increased area per cell with increasing substrate stiffness. We also found that these cells exhibit a bimodal mode of cell motility, consisting of alternating, intermittent periods of motion and cell arrest. In particular, we found that the cells became less motile and spent less time moving on the stiffer substrates. Interestingly, the displacement and velocities of the cells were maximized on substrates between 2-20kPa, indicating an optimal stiffness region. We also studied the effect of silencing the protein FMNL2 in A2058 cells. FMNL2 knockdown showed similar results, but when compared to the control cells, they were less motile and more elongated than the control cells on the same substrate. Moreover, we found that suppressing FMNL2 resulted in the cells on the stiffer substrates spending less time in motion, which resulted in the average net distance travelled and displacement being smaller than the controls. Our results are consistent with other studies in the literature that show trends for adherent cells to become more elongated and less motile with increasing substrate stiffness beyond their optimal region. Furthermore, the results indicate that the suppression of FMNL2 plays a role in modulating cell morphology and motility on substrates of different moduli, and

that FMNL2 may play a role in a cells ability to initiate motion and migrate.

4.2 Methodology

4.2.1 Cell Culture

A2058 (CRL-11147) metastatic melanoma cells were obtained from the Copeland lab in the Faculty of Medicine at the University of Ottawa. The cells were cultured in Dulbecco's modified Eagle's medium containing 10% fetal bovine serum. Cells were kept at $37°C$ in 5% CO_2. Cells were used for experiments until passage number 12.

siRNA-mediated knockdown was performed by Sarah Fox from the Copeland lab, as previously described [59] using Dharmafect1 (Horizon Discovery Ltd; T-2001-03) and the following siRNA duplexes: FMNL2 siRNA Duplex1 (IDT; hs.Ri.FMNL2.13.1); FMNL2 siRNA duplex2 (IDT; hs.Ri.FMNL2.13.2).

4.2.2 Hydrogel Preparation

Silicone substrates were obtained and prepared by Sarah Fox from the Copeland lab, as follows. Advanced Biomatrix CytoSoft 6-well plates discovery kit #5190, consisting of an Eppendorf 6-well cell culture plate (Eppendorf 0030.720.113) filled with 0.5mm layers of activated biocompatible silicone of defined elastic modulus, were used for all live-cell imaging. Advanced Biomatrix CytoSoft Imaging 24-well Plates 0.2kPa (#5183) and 64kPa (#5189), consisting of an Eppendorf 24 well cell imaging plate (0030.741.021) with #1.5 glass bottom filled with a $\sim$ 0.03mm layer of activated biocompatible silicone of defined elastic modulus, were used for fixed cell imaging. Silicone surfaces were coated with a Fibronectin solution (bovine plasma, Sigma; F1141) at a final concentration of 10µg/ml in DPBS (Wisent; 311-425 CL) for 1 hour at room temperature. The fibronectin solution was removed, and the plates maintained in DPBS until the cells were added.

Homogeneous moduli collagen hydrogel substrates were prepared as described in Chapter 3.3. After crosslinking, the hydrogels were washed in PBS three times, and then placed onto a shaker plate with fresh PBS overnight. The following day, the hydrogels were then rinsed with PBS

again, and then cell culture media was added and the hydrogel was placed into a cell incubator for 3 hours prior to the addition of cells.

4.2.3 Live Cell Imaging

On the silicone substrates, live cell imaging was performed on an Incucyte S3 Live-Cell Analysis System at 37°C at 5% CO_2. A 10X/NA 0.3 objective lens was used to capture phase contrast images with a spatial resolution of 1.2μm/pixel at an interval of 20 minutes for 24 hours. For the bio-mimetic collagen substrates, imaging was performed using a Nikon Eclipse Ti-S microscope with an in-house designed image acquisition system. A 4X and 10X lens were used to acquire images at an interval of 10 minutes for up to 48 hours.

4.2.4 Morphology Analysis

Using the Python package OpenCV [111], the tiff stacks were first thresholded, a process where the pixels are binarized based on their intensity, and then pixels with a value less than the defined threshold are assigned to white, while the values above the threshold were assigned to black. The tiff stacks are subsequently filtered using a Gaussian blur to reduce noise in the image. To quantify the morphology of cells, the cells were first located using the opencv function "findContours", which identifies the boundary of objects in binarized images by looking for sharp increases or decreases in adjacent pixel values. Following this, the function "fitEllipse" was then used to fit an ellipse to the contours identified in the previous step. Using the contours, a mask is then created by converting all the pixels populating the inside of the contour into a binary image. The major and minor axis of the ellipse were then extracted and exported to a csv file, as well as the area, perimeter, and spatial coordinates of the boundary of the mask. With these values, we can calculate the roundness of each cell (r) as the ratio of the minor to major axis of the fitted ellipse. We can then average over all cells on the substrate to obtain the group average roundness (R). To calculate the Feret diameter (FD), a Python script calculates the distance between all points around the boundary of the mask, and then extracts the maximum value.

4.2.5 Motility Analysis

To track the cells, they were located using OpenCV's contour finding function, and then tracked for the entire tiff stack with the Discriminative Correlation Filter with Channel and Spatial Reliability (CSRT) tracker in OpenCV. This object tracking algorithm works by applying discriminative correlation filters to different feature channels of the image (color, texture, etc) to determine their reliability. Each channel is weighted independently of the other based off how reliable they're deemed to be. The tracker also learns to discriminate between the object and its background to enhance accuracy when the background may contain distracting elements. At each time point, the x and y coordinates of each cell along were recorded and exported as a csv file, and subsequently analyzed to determine all motility measurements once tracking was complete. The net distance travelled by each cell was then calculated by summing the distance travelled in each dimension.

The speed of each cell between each time step was also calculated to determine if and how fast the cell was moving. If the speed of the cell was less than 5μm/h, than it was classified as not moving, as speeds less than this were often due to morphological changes in the cell that changed its center of mass, and not true movement. The time spent stationary (t_s) and moving (t_m) were then calculated for each cell using this restriction.

4.2.6 Statistical & error analysis

All experimental measurements were recorded, and the mean and standard deviation (SD) of these values were calculated. The uncertainty associated with each mean value was calculated using the standard error of the mean (SEM). For calculating the uncertainty on measurements using the calculated mean values, propagation of error was used to determine their associated error. To determine statistical significance between two measured values, Analysis of Variance (ANOVA) testing was performed to discern any statistically significant differences between the groups. Tukey's post hoc analysis was then performed to identify significant results between the mean values of different groups. All statistical analyses were conducted with a pre-established alpha level of 0.05, denoting the threshold for statistical significance.

4.3 Results

4.3.1 A2058 Behavior on Homogeneous Silicone Substrates

Previous studies have shown that substrate stiffness can have noticeable effects on melanoma cell morphology and motility. To more accurately reflect the in vivo environment in which melanoma cells reside, wild type A2058 cells were plated on fibronectin functionalized silicone hydrogels characterized by varying stiffness levels, characterized by Young's modulus E of 0.2kPa, 0.5kPa, 2.0kPa, 8.0kPa, and 64.0kPa. FMNL2 knockdown cells were also plated simultaneously, and the analysis below presents the data for both the control and knockdown cells.

Morphology

In both the control and knockdown cell populations, the cells adopted a more circular morphology on the soft substrates (0.2kPa and 0.5kPa), and became progressively more elongated as the substrate stiffness increased, shown qualitatively in Figure 4.1 A. This behavior is reflected quantitatively in Figure 4.1 B and Table 4.1 by the average roundness value, R, which was found to decrease as the substrate modulus increased. R for the native A2058 cells decreased from 0.763 ± 0.002 on the 0.2kPa substrate to 0.615 ± 0.001 on the 64.0kPa substrate. The FMNL2 knockdown cells showed similar behavior, with R decreasing from 0.714 ± 0.002 on the 0.2kPa substrate to 0.534 ± 0.001 on the 64.0kPa substrate. The net average roundness change, ΔR, defined as the difference between the R value of the current substrate modulus and the 0.2kPa substrate value (given in Table 4.2), becomes progressively more negative with increasing substrate modulus for both control and FMNL2 knockdown cells.

The area (A), perimeter (P), and Feret diameter (FD), were also calculated for each cell and averaged over the cell population to further characterize the effect of substrate stiffness on cell morphology. All values were found to monotonically increase as the substrate got stiffer, as shown in Table 4.1. The net average area increase, ΔA, between the 0.2kPa substrate and the 64.0kPa substrate was $\Delta A = 129 \pm 11$ µm^2 for the native A2058 cells and $\Delta A = 107 \pm 9$µm^2 for the FMNL2 knockdown cells as shown in Table 4.2. Likewise, the net average cell perimeter and FD increases

between the 0.2kPa and 64.0kPa substrates, with ΔP= 30.1 $\pm$ 1.1µm and ΔFD = 14 $\pm$ 0.3µm for the native cells and with ΔP= 32.4 $\pm$ 1.1µm and ΔFD = 14.2 $\pm$ 0.2µm. The area and perimeter increasing indicates that the cells became more spread out as the substrate got stiffer, and the increase in FD shows that the cells became more elongated as the substrate got stiffer.

Notably, when compared to the control A2058 cells, FMNL2 knockdown cells showed smaller values of roundness R, and larger average values of cell area A, average cell perimeter P and Feret diameter FD on equivalent stiffness substrates. We quantify this by defining a difference δX between FMNL2 knockdown (KD) and control cells, $\delta X = X_{kd}\text{-}X_{con}$ for X=R,A,P or FD, as shown in Table 4.3. The trends of δA decreasing (becoming more negative) and δP and δFD increasing with substrate modulus further corroborates the decrease in δR with increasing modulus, as these changes indicate that the knockdown cells became more elongated than the control cells on the same substrate.

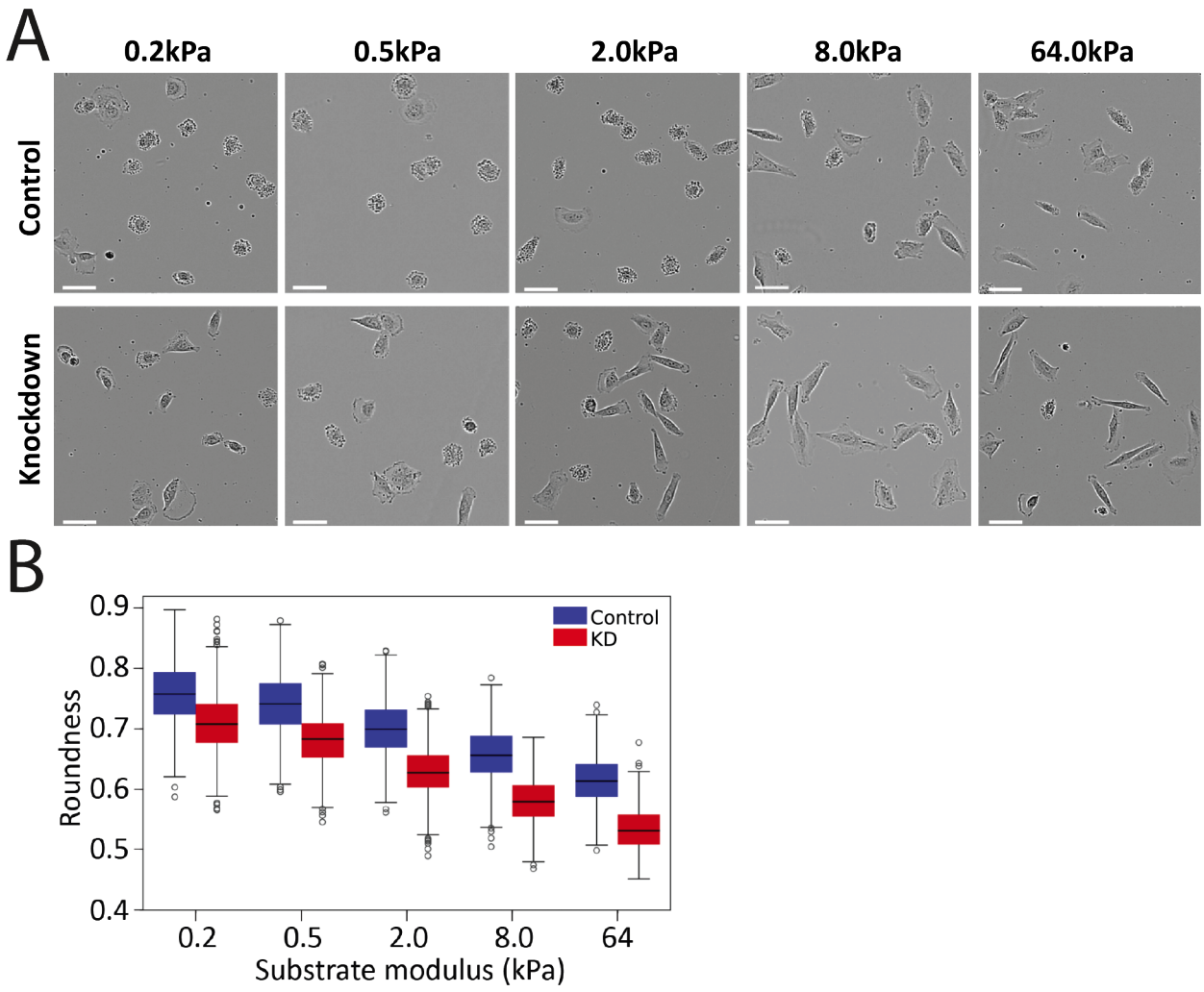

Figure 4.1: A2058 morphology changes across substrates with increasing modulus. 10X magnification images of A2058 control and knockdown cells on 0.2kPa, 0.5kPa, 2.0kPa, 8.0kPa, and 64.0kPa substrates (A). The average roundness value for control and knockdown A2058 cells across all substrates (B). FMNL2 knockdown cells have a lower roundness value than the controls across all substrates.

	Control				Knockdown			
Modulus (kPa)	A (μm^2)	P (μm)	FD (μm)	R	A (μm^2)	P (μm)	FD (μm)	R
0.2	951 ± 8	144.9 ± 0.8	44.1 ± 0.2	0.763 ± 0.002	897 ± 7	149.5 ± 0.8	46.7 ± 0.1	0.714 ± 0.002
0.5	947 ± 9	143.7 ± 0.7	44.2 ± 0.2	0.742 ± 0.002	910 ± 6	150.4 ± 0.9	47.5 ± 0.1	0.683 ± 0.002
2.0	1030 ± 8	154.7 ± 0.7	47.5 ± 0.1	0.704 ± 0.001	923 ± 7	158.3 ± 0.8	50.6 ± 0.2	0.633 ± 0.001
8.0	1050 ± 8	165 ± 0.8	52.9 ± 0.1	0.663 ± 0.001	961 ± 6	171.3 ± 0.9	55.8 ± 0.2	0.583 ± 0.001
64.0	1080 ± 7	175 ± 0.8	56.5 ± 0.2	0.615 ± 0.001	1004 ± 6	181.9 ± 0.8	60.9 ± 0.2	0.534 ± 0.001

Table 4.1: Morphological changes in A2058 cells on increasing moduli substrates. The average area (A), perimeter (P), Feret diameter (FD), and roundness (R) are shown for the control and knockdown cells on each substrate. The error on each value is the standard error of the mean.

	Control				Knockdown			
Modulus (kPa)	ΔA (μm^2)	ΔP (μm)	ΔFD (μm)	ΔR	ΔA (μm^2)	ΔP (μm)	ΔFD (μm)	ΔR
0.2 – 0.5	-4 ± 10	-1.2 ± 1.1	0.1 ± 0.2	-0.021 ± 0.003*	13 ± 9	0.9 ± 1.2	0.8 ± 0.1*	-0.031 ± 0.003*
0.2 – 2.0	79 ± 11*	9.8 ± 1.1*	3.4 ± 0.2*	-0.059 ± 0.002*	26 ± 10*	8.8 ± 1.1*	3.9 ± 0.2*	-0.081 ± 0.002*
0.2 – 8.0	99 ± 11*	20.1 ± 1.1*	8.8 ± 0.2*	-0.100 ± 0.002*	64 ± 9*	21.8 ± 1.2*	9.1 ± 0.2*	-0.131 ± 0.002*
0.2 - 64.0	129 ± 11*	30.1 ± 1.1*	12.4 ± 0.3*	-0.148 ± 0.002*	107 ± 9*	32.4 ± 1.1*	14.2 ± 0.2*	-0.180 ± 0.002*

Table 4.2: Net morphological changes of control and knockdown cells between the 0.2kPa substrate and 0.5, 2.0, 8.0, and 64 kPa substrates for average area (ΔA), perimeter (ΔP), Feret diameter (ΔFD), and roundness (ΔR), *p<0.0001.

Modulus (kPa)	δA (μm^2)	δP (μm)	δFD (μm)	δR
0.2	-54 ± 11*	4.6 ± 1.1*	2.6 ± 0.2*	-0.049 ± 0.003*
0.5	-37 ± 11*	6.7 ± 1.1*	3.3 ± 0.2*	-0.059 ± 0.003*
2.0	-107 ± 11*	3.6 ± 1.1*	3.1 ± 0.2*	-0.071 ± 0.001*
8.0	-89 ± 10*	6.3 ± 1.2*	2.9 ± 0.2*	-0.080 ± 0.001*
64.0	-76 ± 9*	6.9 ± 1.1*	4.4 ± 0.3*	-0.081 ± 0.001*

Table 4.3: Net morphological changes between control and knockdown A2058 cells. The average changes relative to control cells for area (δA), perimeter (δP), Feret diameter (δFD), and roundness (δR), were calculated by taking the difference between the control and knockdown values on the same substrate, *p<0.0001.

Motility

To assess the motility of A2058 cells on these substrates, they were tracked for 24 hours to determine if the substrate stiffness and FMNL2 knockdown impacted their motion. From this data, we first calculated the cells displacement, and plotted the results in figure 4.2 below as histograms. The average overall displacements are summarized in Table 4.4.

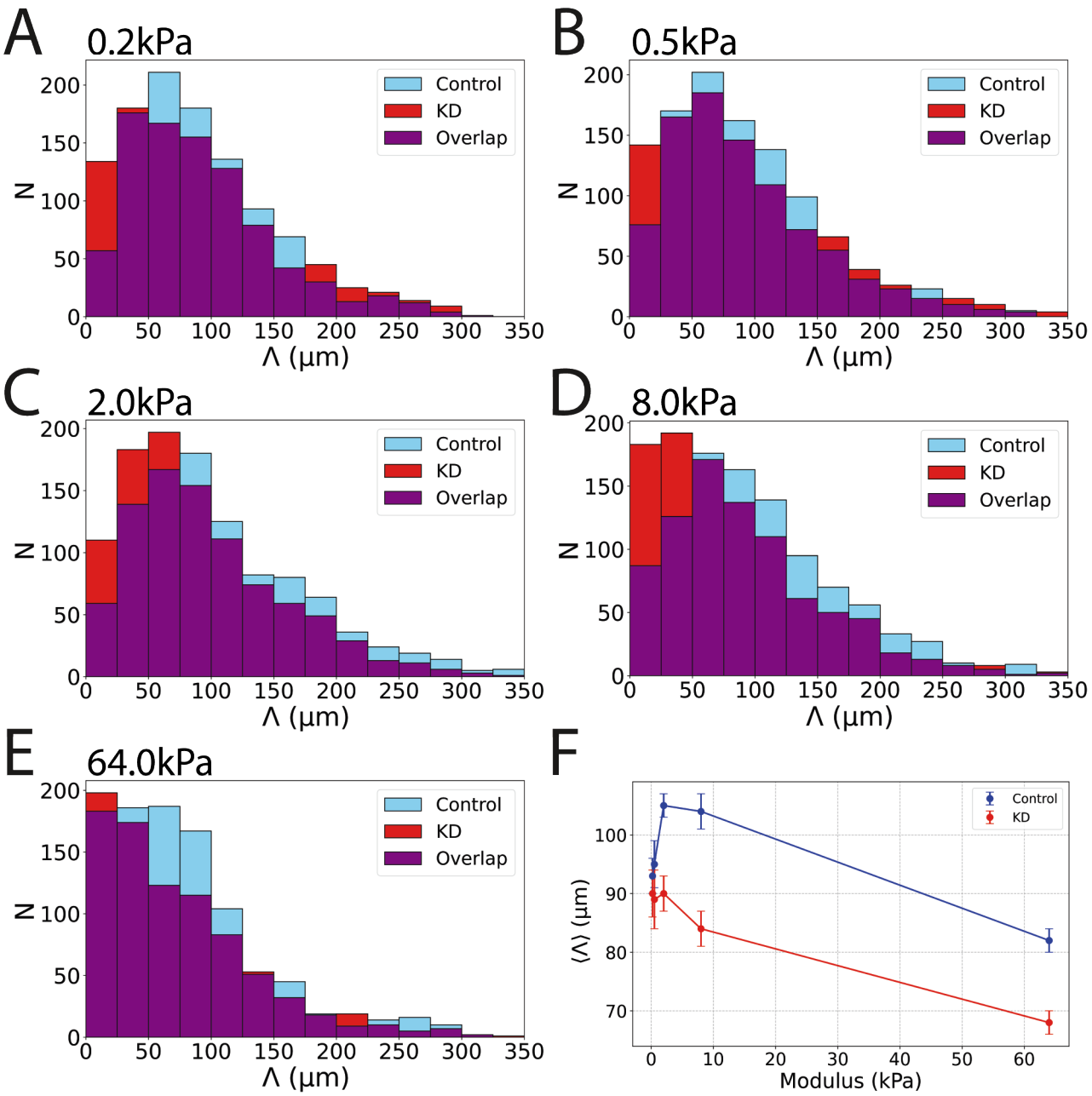

Figure 4.2: Histograms of cell displacement magnitude (Λ) for control and KD cells substrates of different moduli. Panels A, B, C, D, and E, refer to the 0.2kPa, 0.5kPa, 2.0kPa, 8.0kPa, and 64.0kPa substrates respectively. Panel F is the ensemble-averaged cell displacement magnitude $\langle\Lambda\rangle$ as a function of substrate modulus for the control and KD cells (H).

The Ensemble-averaged cell displacement $\langle\Lambda\rangle$ for both the control and knockdown cells increased from the 0.2kPa up to the 2kPa substrates, and then had a pronounced decrease afterwards. The ensemble-averaged x and y components of the displacement vector $\vec{\Lambda}$,were close to

	Control			Knockdown			
Modulus (kPa)	$\langle\Lambda_x\rangle$ (μm)	$\langle\Lambda_y\rangle$ (μm)	$\langle\Lambda\rangle$ (μm)	$\langle\Lambda_x\rangle$ (μm)	$\langle\Lambda_y\rangle$ (μm)	$\langle\Lambda\rangle$ (μm)	$\Delta\Lambda$ (μm)
0.2	2 ± 2	-1 ± 2	93 ± 2	-5 ± 3	-1 ± 2	90 ± 3	3
0.5	-1 ± 2	-1 ± 2	95 ± 2	3 ± 2	-3 ± 2	89 ± 1	6*
2.0	1 ± 2	-2 ± 2	105 ± 3	6 ± 2	0 ± 2	90 ± 2	15***
8.0	-2 ± 2	2 ± 2	104 ± 2	2 ± 2	-2 ± 2	84 ± 2	20****
64.0	0 ± 1	0 ± 1	82 ± 1	-1 ± 1	1 ± 1	68 ± 1	14***

Table 4.4: Ensemble-averaged cell displacement magnitude ($\langle\Lambda\rangle$) and the corresponding ensemble-averaged cell displacement components (as signed numbers) with their standard error on the mean (SEM) for control and knockdown A2058 cells. The last column shows the difference between the control and knockdown average cell displacement magnitudes. *p<0.05, **p<0.01, ***p<0.001, ****p<0.0001

zero for all substrates, indicating that there was no preferential direction of cell motion on these substrates. Furthermore, when we compare the motion between the control and knockdown cells on the same substrate, we can see that the knockdown cells had a lower average displacement, with the difference being statistically significant on the 0.5kPa, 2.0kPa, 8.0kPa, and 64.0kPa substrates. So, these cells seemed to have the largest motion on the substrates in the intermediate range of tested stiffness.

We next determined the average velocity of all of the cells on each substrate (Table 4.5). These quantities further corroborate the average displacement results above, as the velocities had their largest value on the substrates in the intermediate modulus region. Interestingly, there were also statistically significant decreases in the average velocity on the 2.0kPa, 8.0kPa, and 64.0kPa substrates between the control and knockdown cell populations.

Following this, the MSD of each cell was then calculated and used to determine the diffusive behavior of the control and knockdown cells on these substrates. Specifically, we calculated cumulative diffusion coefficient and the anomalous exponent, the exponent obtained from a power law regression of the MSD, from t = 0 to the time at the plotted data point for each sample condition. In figure 4.3A, the ensemble-averaged MSD is plotted for each of the substrates. In Figure 4.3B, the corresponding cumulative anomalous diffusion exponent was plotted as a function of time. A quantitative summary of the diffusive behavior is given in Table 4.6.

	Control			Knockdown			
Modulus (kPa)	v_x (μm/h)	v_y (μm/h)	v (μm/h)	v_x (μm/h)	v_y (μm/h)	v (μm/h)	Δv (μm/h)
0.2	0.2 $\pm$ 0.1	-0.1 $\pm$ 0.05	26 $\pm$ 1	-0.5 $\pm$ 0.2	-0.1 $\pm$ 0.05	25 $\pm$ 1	1
0.5	-0.1 $\pm$ 0.05	-0.1 $\pm$ 0.05	25 $\pm$ 2	0.3 $\pm$ 0.1	-0.3 $\pm$ 0.1	25 $\pm$ 1	0
2.0	0 $\pm$ 0.05	0.1 $\pm$ 0.05	28 $\pm$ 2	0.7 $\pm$ 0.2	0 $\pm$ 0.05	25 $\pm$ 1	3*
8.0	-0.1 $\pm$ 0.05	0.2 $\pm$ 0.1	29 $\pm$ 2	0.2 $\pm$ 0.1	-0.2 $\pm$ 0.1	22 $\pm$ 2	7***
64.0	0 $\pm$ 0.05	-0.2 $\pm$ 0.1	23 $\pm$ 1	0 $\pm$ 0.05	0 $\pm$ 0.05	19 $\pm$ 1	4**

Table 4.5: The average velocity components, v_x and v_y, and the magnitude of the velocity v of the cells on all of the tested substrates for the control and knockdown cell populations. *p<0.05, **p<0.01, ***p<0.001

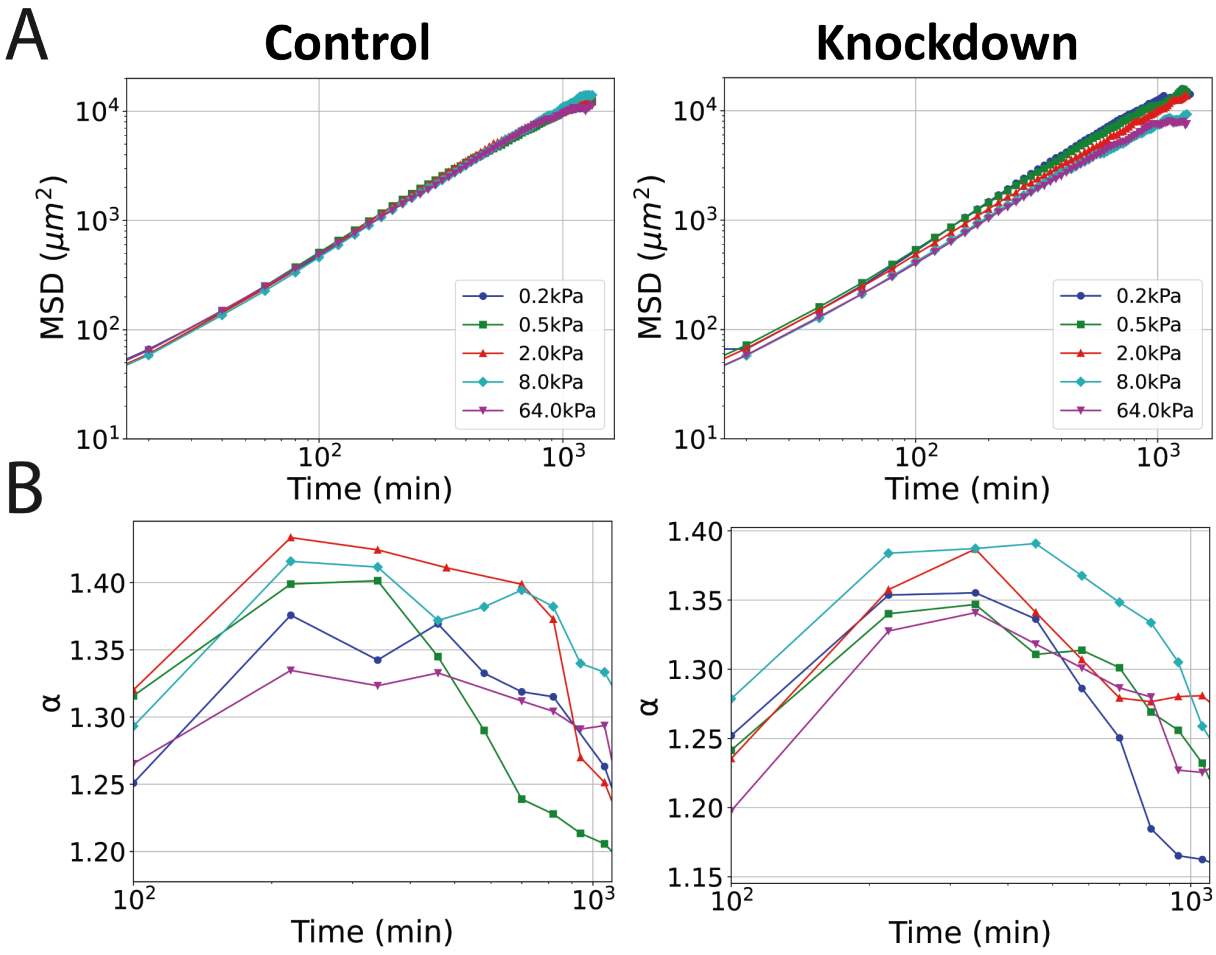

Figure 4.3: The ensemble-averaged MSD of control and knockdown cells on all tested substrates (A). The cumulative anomalous diffusion exponent as a function of time for both groups of cells (B).

As shown in Figure 4.3A, the MSD of the cells on the silicone substrates were not indicative of simple diffusion. Rather, they all suggest a regime of superdiffusive behavior with MSD curves that gradually slow as if approaching a plateau at large lag times. This slowing is more noticeable in the knockdown cells than it is in the control cells. In Figure 4.3B we see that the cumulative exponent corroborates this behavior, with most of the curves increasing up to a maximum value of α, and then decreasing at large lag times. Interestingly, the 2.0kPa and 8.0kPa substrates had the largest exponent in both the control and knockdown cell populations.

To further assess the impact of substrate stiffness and the protein knockdown on cell motion, we next examined several scalar quantifiers of motility described in Chapter 2: the total distance travelled L, the average time spent in motion t_m, and the average moving speed s_m of each cell. Histograms of the total distance L travelled by control and knockdown cells are plotted together in Figure 4.4 below, from which we may calculate an ensemble-averaged value of the total distance travelled, $\langle L \rangle$. A summary of the data is presented in Table 4.6.

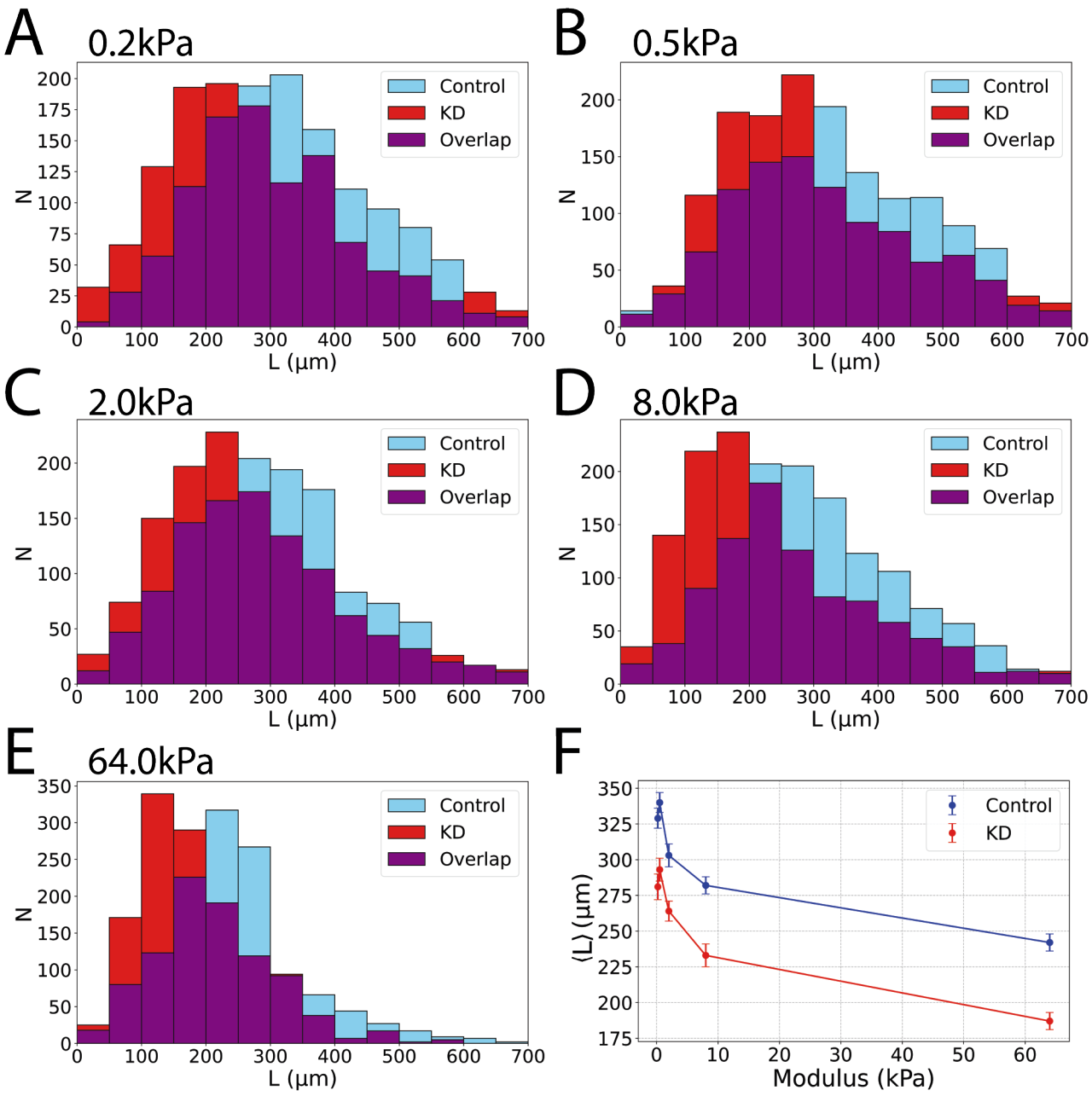

Figure 4.4: Histograms of cell path distance (L) for the control and KD cells. Figures A-E, represent the 0.2kPa, 0.5kPa, 2.0kPa, 8.0kPa, and 64.0kPA substrates respectively. Figure F shows the ensemble-averaged value ⟨L⟩ plotted against substrate modulus.

Overall, both A2058 cell types were found to travel less on the stiffer substrates, as shown in the histogram data in Figure 4.4. In particular, the ensemble-averaged total distance travelled, ⟨L⟩, decreased with increasing substrate modulus. For the control cells, ⟨L⟩ decreased from 329 ± 4 μm on the 0.2kPa substrate to 242 ± 4 μm on the 64.0kPa substrate, while for the knockdown

Modulus (kPa)	Control $\langle L \rangle$ (μm)	KD $\langle L \rangle$ (μm)	Difference $\langle \Delta L \rangle$ (μm)
0.2	329 ± 4	281 ± 4	-48 ± 6****
0.5	340 ± 4	293 ± 4	-47 ± 6****
2.0	303 ± 4	264 ± 4	-39 ± 6****
8.0	282 ± 3	233 ± 4	-49 ± 5****
64.0	242 ± 3	187 ± 3	-55 ± 4****

Table 4.6: The ensemble-averaged distances travelled $\langle L \rangle$ with their standard errors of the mean (SEM) for control and knockdown A2058 cells. The last column shows the difference between the control and knockdown means. ****p<0.0001

cells $\langle L \rangle$ decreased from 282 ± 4 µm to 187 ± 3 µm, as shown in Table 4.6. Across all five substrates tested, the knockdown cells consistently had an average total distance between 39 ± 3 µm and 55 ± 4 µm less than the control cells. The distribution for the knockdown cells on all substrates was shifted towards a smaller average value on every histogram, indicating that the knockdown cells travelled less on average than the control cells.

These cells adopted a bimodal pattern of cell motility characterized by alternating periods of motion and arrest, as can be seen by examining the average time spent moving by each cell, t_m. In these experiments, the cells were imaged for 24 hours, and t_m is the proportion of that time that tracked cells spent moving. Moreover, using the data for t_m, an average moving speed of each cell, s_m, can be calculated for each substrate modulus and cell type, and used to compute ensemble-averaged values, $\langle t_m \rangle$ and $\langle s_m \rangle$. This analysis allowed us to determine whether cell motility is intrinsically slower on stiffer substrates, or rather if cells remained stationary for longer periods of times on these substrates. For instance, if the value of s_m between the control and knockdown substrates are similar, then the knockdown cells, with a relatively smaller L, would have spent more time in the arrested state. In Figure 4.5 A-E, both t_m and s_m are plotted as histograms with the control and knockdown distributions on the same plot for each substrate. We found that the distributions of these curves seemed to follow a normal distribution, so we then standardized the control and knockdown datasets on all substrates into master curve distributions with a mean of 0 and standard deviation of 1 (Figure 4.5 F-G). A summary of the data sets is given in Table 4.7 for $\langle t_m \rangle$. As shown, both the control and knockdown cells spent less time in motion as the substrate modulus increased. Between the softest substrates (0.2kPa and 0.5kPa), the effect was

not statistically significant. However, for the 2.0kPa, 8.0kPa, and 64.0kPa substrates, there are noticeable shifts in their distributions towards a lower average value (shown in Table 4.7). Next, comparing the time spent moving between the control and knockdown cells, we can see that the knockdown cells did in fact spend less time moving than the control cells on the 2.0kPa, 8.0kPa, and 64.0kPa substrates, while the moving time was found to be statistically equivalent between native and knockdown cells on the 0.2kPa and 0.5kPa substrates. We also note a particularly strong decrease in the moving time of both cells on the 2.0kPa substrates. When we looked closer at the data in this section, we found that there were cells in specific ROI's from the second trial that were moving abnormally slow, which is what caused there to be a small peak in their distributions at a value lower than the mean.

Comparing moving speed between the two cell types on equivalent substrates, the knockdown cells appear to move more slowly than the native A2058 cells, but the differences are less pronounced than those seen in the time spent moving. A summary of the values for the ensemble-averaged cell speed $\langle s_m \rangle$ is given in Table 4.8. This indicates that the knockdown of FMNL2 could affect the overall speed of these cells, but on the stiffer substrates, the decreases seen in the average distance travelled are most likely due to their time spent in the arrested state of their motion. Note also that the behavior on the 2.0kPa substrate, with $\langle s_m \rangle$ values that were lower than those on the 8.0kPa substrate, is likely due to the groups of cells that were moving abnormally slower in the second trial, which cause the average to shift to a lower value.

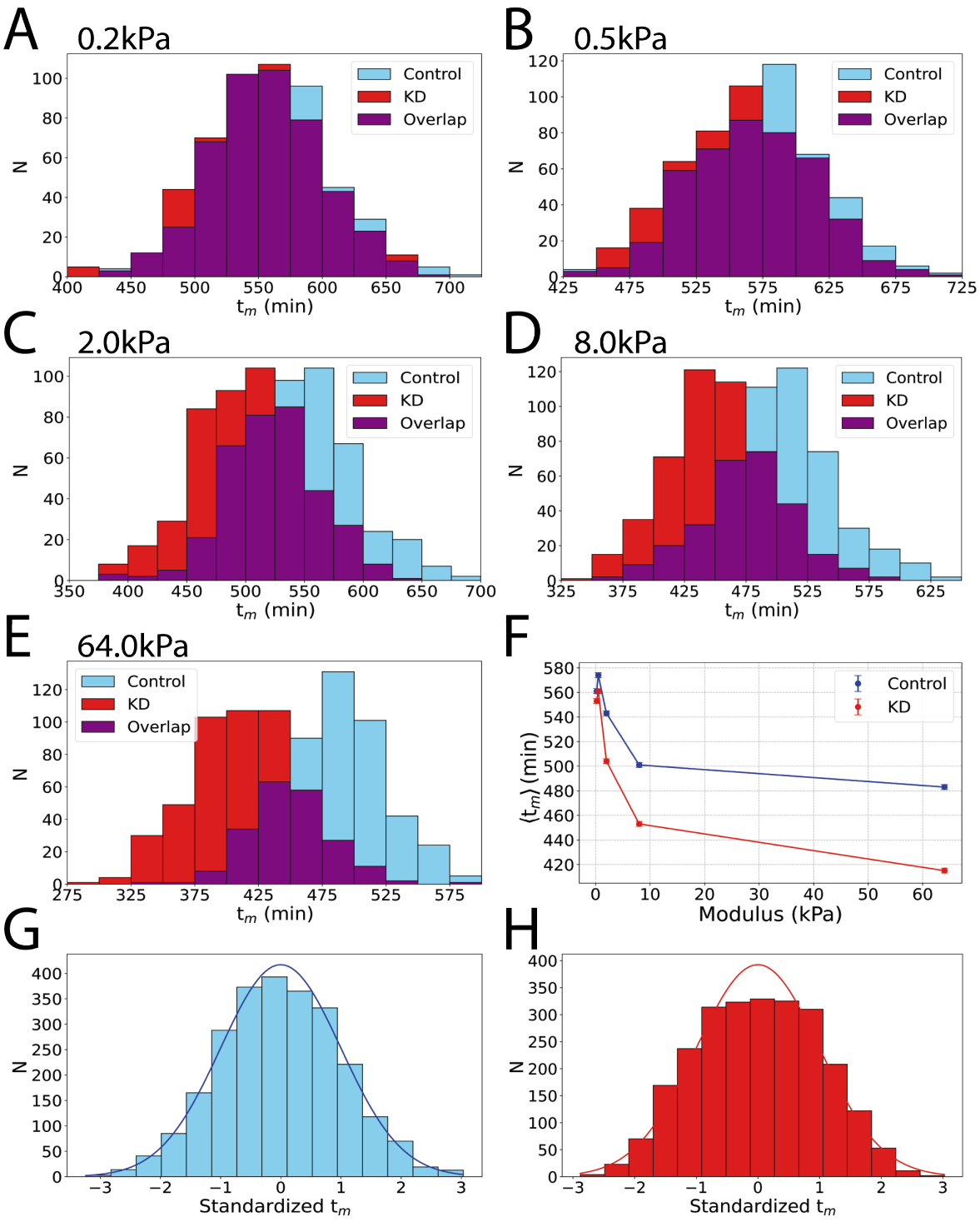

Figure 4.5: Histograms of the time spent moving t_m for the control (blue) and knockdown (KD - red) cells on the 5 tested substrates. Figures A-E are the distributions for both groups on the 0.2kPa, 0.5kPa, 2.0kPa, 8.0kPa, and 64.0kPa substrates respectively. Figures F shows $\langle t_m \rangle$ vs substrate modulus, and G-H are standardized distributions of t_m for the control and KD cells respectively.

Modulus (kPa)	Control $\langle t_m \rangle$ (min)	KD $\langle t_m \rangle$ (min)	Difference $\langle \Delta t_m \rangle$ (min)
0.2	561 ± 2	553 ± 2	-8 ± 3*
0.5	574 ± 2	561 ± 2	-13 ± 3****
2.0	543 ± 2	504 ± 2	-39 ± 3****
8.0	501 ± 2	453 ± 2	-48 ± 3****
64.0	483 ± 2	415 ± 2	-68 ± 3****
Master Curve	Mean	StDev	SEM
Control	530	50	2
KD	500	70	2

Table 4.7: A summary of the ensemble-averaged time spent in motion ($\langle t_m \rangle$) for the control and knockdown (KD) cells on the silicone substrates. The error shown is the SEM. The final column is the difference of the control and KD mean values. *p<0.05, ****p<0.0001

Modulus (kPa)	Control $\langle s_m \rangle$ (μm/h)	KD $\langle s_m \rangle$ (μm/h)	$\langle \Delta s_m \rangle$ (μm/h)
0.2	35.5 ± 0.2	34.9 ± 0.3	-0.6 ± 0.4**
0.5	36.1 ± 0.3	35.4 ± 0.3	-0.7 ± 0.4**
2.0	32.7 ± 0.3	30.9 ± 0.3	-1.8 ± 0.4****
8.0	33.6 ± 0.3	30.8 ± 0.3	-2.8 ± 0.4****
64.0	29.6 ± 0.2	28.4 ± 0.3	-1.2 ± 0.4****

Table 4.8: A summary of the ensemble-averaged moving speed ($\langle s_m \rangle$) for the control and knockdown (KD) cells on the silicone substrates. The error shown is the SEM. The final column is the difference of the control and KD mean values. **p<0.01, ****p<0.0001

4.3.2 A2058 Behavior on Homogeneous Collagen Substrates

Morphology

Similar to the silicone substrates, A2058 cells on the collagen hydrogel substrates also experienced pronounced morphological changes as the substrate stiffness was changed. In particular, the same trend was noticed as on the silicone substrates where the cells became progressively more elongated as the substrate stiffness increased, as shown in Figure 4.6. On the softest substrates (∼2kPa), the cells had an average roundness value of R = 0.68 ± 0.03. While on the stiffest substrates (∼50kPa), the cells had a value of R = 0.59 ± 0.03. The average FD and perimeter P were also found to increase, further indicating increased elongation on these substrates. The knockdown cells also showed similar behaviors, becoming more elongated with increasing substrate stiffness. Furthermore, the knockdown cells were also more elongated than the control cells on the same modulus substrate, consistent with the results from the silicone substrates. Data summarizing the average cell area, perimeter, Feret diameter, and roundness across all tested substrates is given in Table 4.9. Data showing the differences of these averaged parameters between the 1kPa and all other moduli for both the control and knockdown cells are given in Table 4.10. Finally, Table 4.11, shows the differences in these averaged parameters between the control and knockdown cells on the same substrate.

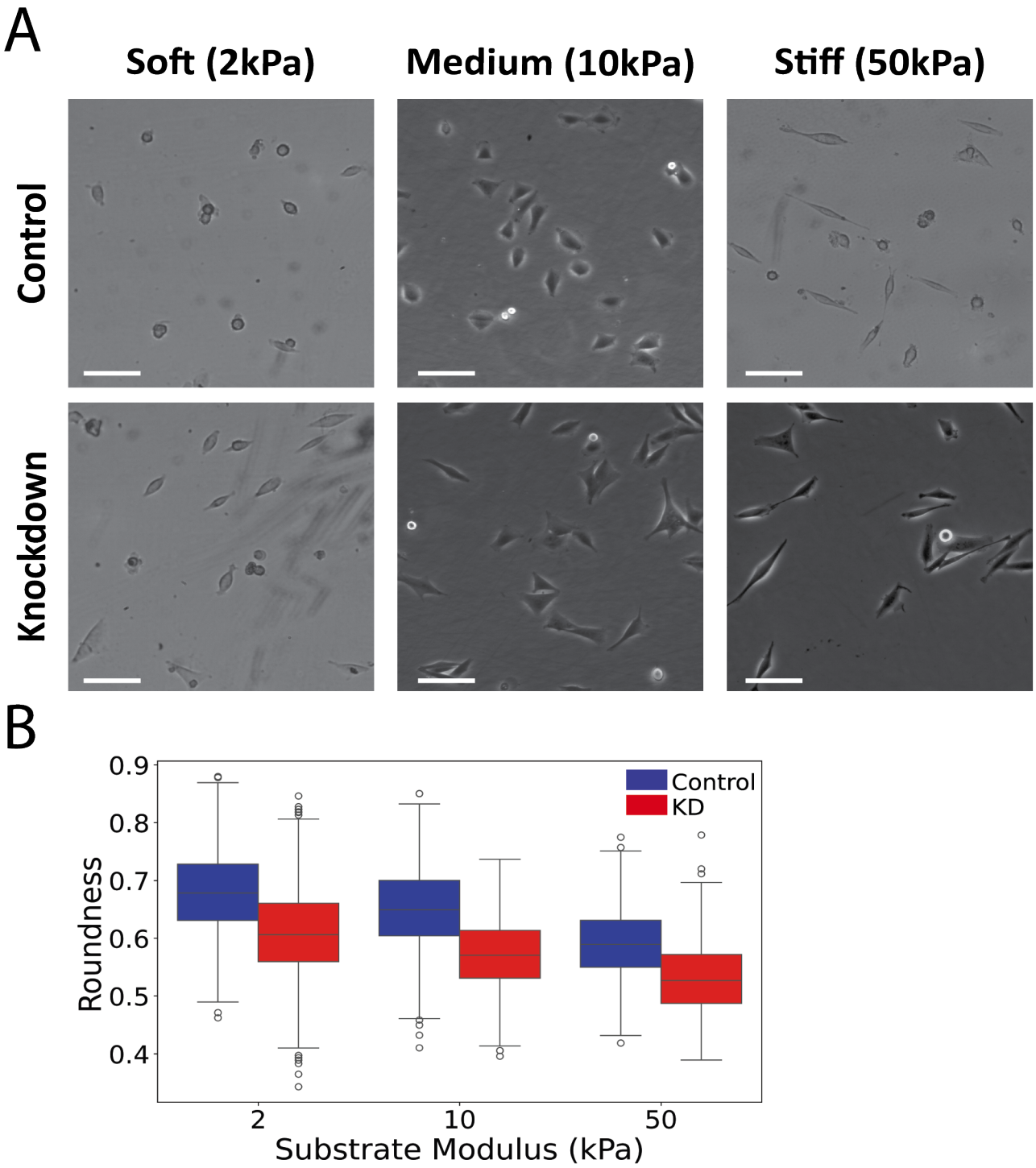

Figure 4.6: A2058 control and knockdown cells on select collagen hydrogel substrates of approximately 2kPa, 20kPa, and 50kPa (A). A boxplot of the average roundness on each of these substrates is shown in B. The scale bar is 100 μm.

	Control				Knockdown			
Modulus (kPa)	A (μm^2)	P (μm)	FD (μm)	R	A (μm^2)	P (μm)	FD (μm)	R
1	980 ± 9	142 ± 2	42 ± 1	0.71 ± 0.01	960 ± 9	144 ± 2	46.7 ± 0.1	0.65 ± 0.03
2	1020 ± 10	147 ± 3	45 ± 2	0.68 ± 0.01	970 ± 10	148 ± 2	47.5 ± 0.1	0.61 ± 0.04
5	1040 ± 10	160 ± 3	47 ± 1	0.67 ± 0.01	980 ± 9	163 ± 0.8	50.6 ± 0.2	0.60 ± 0.03
10	1070 ± 10	163 ± 4	51 ± 2	0.65 ± 0.01	1020 ± 8	167 ± 3	55.8 ± 0.2	0.57 ± 0.03
20	1100 ± 10	172 ± 3	52 ± 1	0.64 ± 0.02	1030 ± 10	178 ± 3	60.9 ± 0.2	0.54 ± 0.03
50	1120 ± 10	174 ± 3	54 ± 1	0.59 ± 0.03	1040 ± 9	181 ± 3	60.9 ± 0.2	0.53 ± 0.05
100	1140 ± 11	179 ± 4	55 ± 1	0.56 ± 0.03	1060 ± 9	183 ± 2	60.9 ± 0.2	0.52 ± 0.04

Table 4.9: Morphological changes in A2058 cells on increasing moduli substrates. The average area (A), perimeter (P), Feret diameter (FD), and roundness (R) are shown for the control and knockdown cells on each substrate. The error on each value is the standard error of the mean.

	Control				Knockdown			
Modulus (kPa)	ΔA (μm^2)	ΔP (μm)	ΔFD (μm)	ΔR	ΔA (μm^2)	ΔP (μm)	ΔFD (μm)	ΔR
1 – 2	40 ± 14*	5 ± 3.6	3 ± 2.2	-0.03 ± 0.01	10 ± 13	4 ± 2.8	0.8 ± 0.1**	-0.04 ± 0.04
1 – 5	60 ± 14*	18 ± 3.6*	5 ± 2.2*	-0.04 ± 0.01*	20 ± 13**	19 ± 2.2*	3.9 ± 0.2**	-0.05 ± 0.04**
1 – 10	90 ± 14**	21 ± 4.5*	9 ± 2.2**	-0.06 ± 0.01**	60 ± 12**	23 ± 3.6*	9.1 ± 0.2***	-0.08 ± 0.04***
1 - 20	120 ± 14***	30 ± 3.6**	10 ± 2.2**	-0.07 ± 0.02**	70 ± 14***	34 ± 3.6*	14.2 ± 0.2***	-0.11 ± 0.04****
1 - 50	140 ± 14****	32 ± 3.6***	12 ± 2.2***	-0.12 ± 0.03****	80 ± 13***	37 ± 3.6*	14.2 ± 0.2****	-0.12 ± 0.04****
1 - 100	160 ± 14****	37 ± 4.5****	13 ± 2.2****	-0.15 ± 0.03****	100 ± 13***	39 ± 2.8****	14.2 ± 0.2****	-0.13 ± 0.04****

Table 4.10: Net morphological changes of control and knockdown cells between the 1 kPa substrate and other modulus values for average area (ΔA), perimeter (ΔP), Feret diameter (ΔFD), and roundness (ΔR). *p<0.05, **p<0.01, ***p <0.001, ****p<0.0001.

Modulus (kPa)	δA (μm^2)	δP (μm)	δFD (μm)	δR
1	20 ± 12**	-2 ± 1	-4.7 ± 0.1**	0.06 ± 0.02*
2	50 ± 14***	-1 ± 2	-2.5 ± 0.2**	0.07 ± 0.03*
5	60 ± 13***	-3 ± 2*	-3.6 ± 0.2***	0.07 ± 0.03***
10	50 ± 12**	-4 ± 2**	-4.8 ± 0.2***	0.08 ± 0.03***
20	70 ± 14***	-6 ± 2**	-8.9 ± 0.2****	0.10 ± 0.04***
50	80 ± 13****	-7 ± 2***	-6.9 ± 0.2****	0.06 ± 0.02***
100	80 ± 14****	-4 ± 1**	-5.9 ± 0.2****	0.04 ± 0.02***

Table 4.11: Net morphological changes between control and knockdown A2058 cells. The average changes relative to control cells for area (δA), perimeter (δP), Feret diameter (δFD), and roundness (δR), were calculated by taking the difference between the control and knockdown values on the same substrate, *p<0.05, **p<0.01, ***p <0.001, ****p<0.0001.

Motility

Similar to the analysis for the silicone substrates, we followed the same analysis workflow for the collagen substrates, so the presentation here will be substantially streamlined. We began by determining the displacements of the cells on all of the tested substrates and creating histograms of the control and knockdown results (Figure 4.7). The results we obtained, while qualitatively similar to the those on the silicone substrates, showed some modest quantitative differences. For the silicone substrates, the maximum in the ensemble-averaged displacement was found on the 2kPa substrate $\langle\Lambda\rangle = 105 \pm 3\mu$m), where it then decreased on either side. Whereas on the collagen substrates, we found that the average displacement reached a maximum value of $\langle\Lambda\rangle = 110 \pm 2\mu$m on the 10kPa substrate, and on either side of this the displacement decreased. In the knockdown cells, the maximum displacement $\langle\Lambda\rangle$ was $95\pm2\mu$m on the 5kPa substrate. However, as the stiffness increased, the displacement did drop in the same way as the silicone substrates, with the lowest values being $\langle\Lambda\rangle = 85 \pm 1\mu$m and $\langle\Lambda\rangle = 70 \pm 1\mu$m for the control and knockdown cells, respectively, on the 100kPa substrate. Another notable difference is that these average values of displacement are larger than the average displacements for both groups of cells on the 64kPa silicone substrate (82 ± 1 μm and $68 \pm 1\mu$m), even though this substrate was stiffer by 36kPa. Nevertheless, when we compare the control and knockdown averages on the same substrate, we see that the average displacement for the knockdown cells was always smaller than the control cell displacements, similar to the results on the silicone substrates. The differences between the averages were statistically significant for all substrates $\geq$ 2kPa (Table 4.12). As expected, the displacement components along x and y were always close to 0, as with the silicone substrates, indicating no directed motion. Finally, the average cell velocity data (Table 4.13) also further corroborated these results, showing a maximum of $v = 29 \pm 2$ μm/h on the 10kPa substrate for the control cells, and $v = 26 \pm 1$ μm/h on the 5kPa substrate for the knockdown cells.

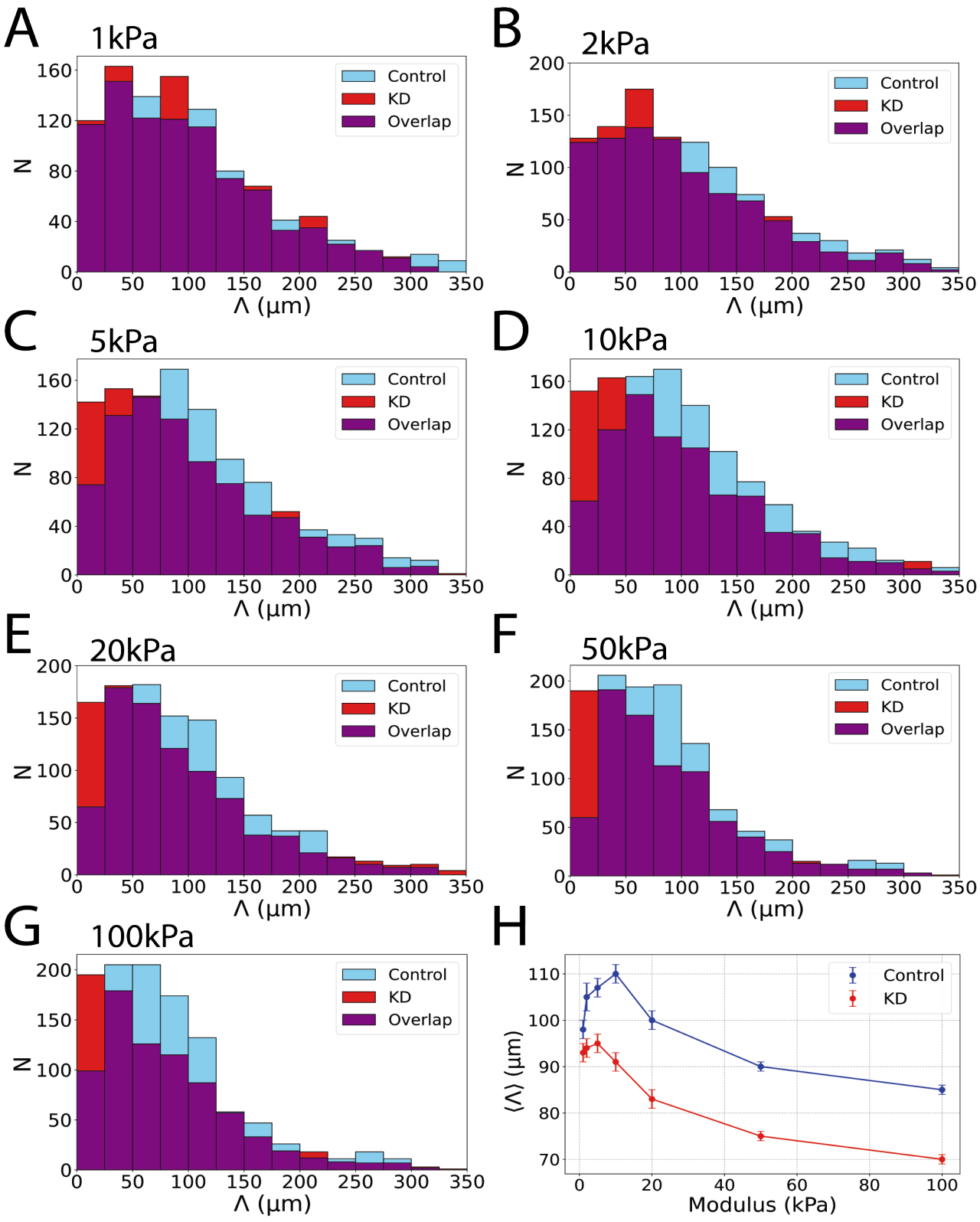

Figure 4.7: Histograms of the net displacement (Λ) of control (Blue) and knockdown (KD - Red) cells on all tested substrates (A-G). Ensemble-averaged cell displacement magnitude $\langle\Lambda\rangle$ as a function of substrate modulus for the control and KD cells (H).

	Control			Knockdown			
Modulus (kPa)	$\langle\Lambda_x\rangle$ (μm)	$\langle\Lambda_y\rangle$ (μm)	$\langle\Lambda\rangle$ (μm)	$\langle\Lambda_x\rangle$ (μm)	$\langle\Lambda_y\rangle$ (μm)	$\langle\Lambda\rangle$ (μm)	$\Delta\Lambda$ (μm)
1	1 ± 2	0 ± 2	98 ± 2	0 ± 2	-1 ± 2	93 ± 2	5
2	1 ± 2	-2 ± 2	105 ± 3	6 ± 2	0 ± 2	94 ± 2	11*
5	0 ± 1	1 ± 2	107 ± 2	3 ± 2	-1 ± 2	95 ± 2	12**
10	-1 ± 2	2 ± 2	110 ± 2	2 ± 2	-1 ± 2	91 ± 2	19***
20	0 ± 1	1 ± 1	100 ± 2	1 ± 1	0 ± 1	83 ± 2	17***
50	-1 ± 1	0 ± 1	90 ± 1	0 ± 1	-1 ± 1	75 ± 1	15***
100	0 ± 1	0 ± 1	85 ± 1	-1 ± 1	1 ± 1	70 ± 1	15***

Table 4.12: Ensemble-averaged cell displacement magnitude ($\langle\Lambda\rangle$) and the corresponding ensemble-averaged cell displacement components ($\langle\Lambda_x\rangle$ and $\langle\Lambda_y\rangle$, as signed numbers) with their standard error of the mean (SEM) for control and knockdown A2058 cells across different substrate moduli. The last column shows the differences between control and knockdown values of $\langle\Lambda\rangle$. *p<0.05, **p<0.01, ***p<0.001

	Control			Knockdown			
Modulus (kPa)	v_x (μm/h)	v_y (μm/h)	v (μm/h)	v_x (μm/h)	v_y (μm/h)	v (μm/h)	Δv (μm/h)
1	0.1 ± 0.05	0 ± 0.05	27 ± 1	-0.1 ± 0.1	-0.1 ± 0.05	24 ± 1	1
2	0 ± 0.05	0.1 ± 0.05	28 ± 2	0.7 ± 0.2	0 ± 0.05	25 ± 1	3*
5	-0.05 ± 0.05	0.15 ± 0.05	27 ± 2	0.5 ± 0.1	-0.1 ± 0.05	26 ± 1	3*
10	-0.1 ± 0.05	0.2 ± 0.1	29 ± 2	0.2 ± 0.1	-0.2 ± 0.1	22 ± 2	7***
20	0 ± 0.05	0.1 ± 0.05	28 ± 2	0.1 ± 0.05	-0.1 ± 0.05	21 ± 1	7***
50	0 ± 0.05	-0.1 ± 0.05	25 ± 1	0.1 ± 0.05	0 ± 0.05	20 ± 1	5**
100	0 ± 0.05	-0.2 ± 0.1	23 ± 1	0 ± 0.05	0 ± 0.05	19 ± 1	4**

Table 4.13: The average velocity components, v_x and v_y, and the magnitude of the velocity v of the cells with their standard error of the mean (SEM) for control and knockdown A2058 cells across different substrate moduli. The last column shows the differences in the average velocity between the control and knockdown cell populations.

Following this, the diffusive behavior of the cells was analyzed by plotting their MSD (Figure 4.8A) alongside the cumulative diffusion exponent (Figure 4.8B). Similar to the silicone substrates, the cells exhibited superdiffusive behavior on all substrates, as characterized by the cumulative diffusion exponent consistently being greater than 1. Furthermore, the control cells had the most superdiffusive behavior on the 10kPa substrate. The cells also showed the same behavior of slowing down at large time scales, as characterized by the decrease in the cumulative exponent functions towards larger lag times.

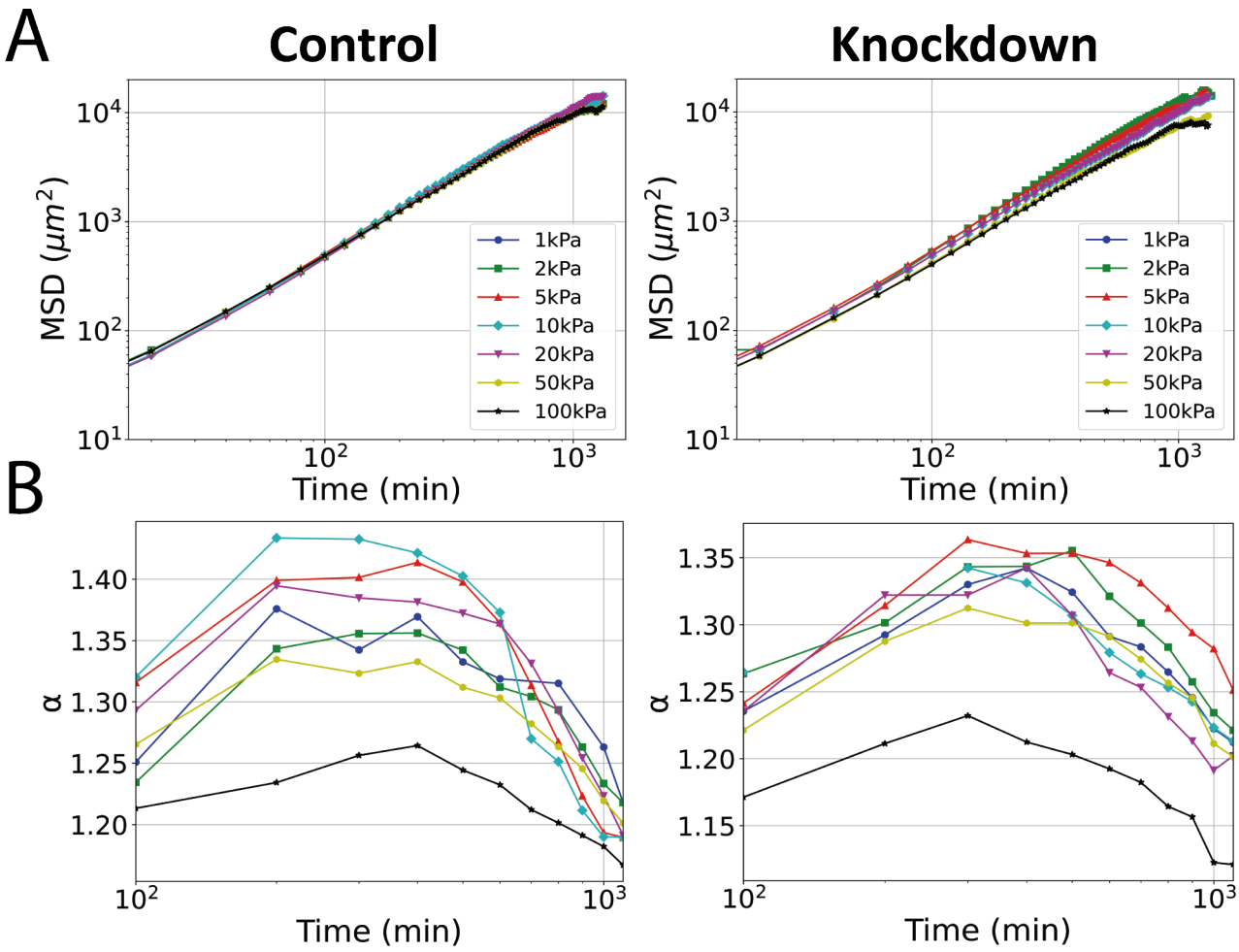

Figure 4.8: The ensemble MSD of control and knockdown cells on all tested collagen substrates(A). The cumulative anomalous diffusion exponent as a function of time for both groups of cells (B).

We then determined the total distance L travelled per cell in different substrate conditions, presented as histograms in Figure 4.9, and calculated the corresponding ensemble-averaged total distance $\langle L \rangle$ in each condition. As before, there were some quantitative differences between the silicone and collagen substrates. While the maximum ensemble-averaged total distance was $\langle L \rangle = 350 \pm 4 \mu$m on the 0.5kPa silicone substrate, the corresponding maximum value was $\langle L \rangle = 380 \pm 6 \mu$m on the 10kPa collagen substrate. On either side of 10kPa, the average value of $\langle L \rangle$ then decreased. Thus, the melanoma cells seemed to have an optimal substrate stiffness around 10kPa on the collagen substrates. Furthermore, on the 100kPa substrate, the control cells moved an average of $\langle L \rangle = 267 \pm 4 \mu$m, whereas on the 64.0kPa silicone substrate, the cells only moved an average of $\langle L \rangle = 242 \pm 3 \mu$m. As a consequence, $\langle L \rangle$ on the silicone decreased faster than it did on the

collagen substrates with an increase of modulus away from the optimum value, as in case with the average displacement, $\langle \Lambda \rangle$. As with the silicone substrates, there reduction in $\langle L \rangle$ between the control and KD cell populations. On the collagen substrates, there were statistically significant decreases between 31-61μm in $\langle L \rangle$ on all substrates except the 1kPa (Table 4.14). Similar to the silicone substrates, the largest decrease was seen on the stiffest substrate, for which $\langle \Delta L \rangle$= -61 μm on the 100kPa substrate.

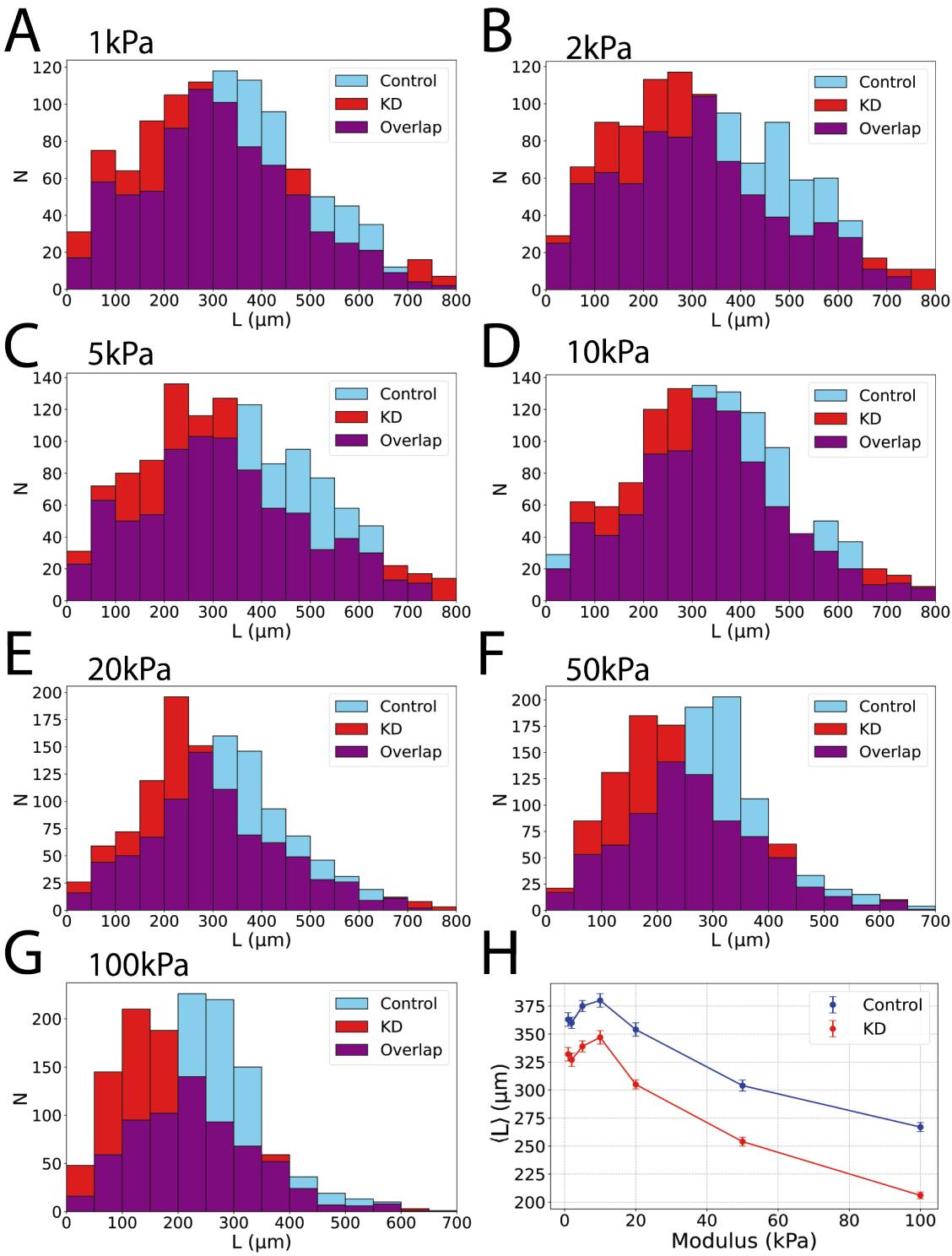

Figure 4.9: The average distance travelled (L) by control (Blue) and knockdown (KD - Red) cells on the collagen substrates. Figures A-G are for the 1kPa, 2kPa, 5kPa, 10kPa, 20kPa, 50kPa, and 100kPa substrates respectively. The ensemble-averaged distance travelled ⟨L⟩ plotted against substrate modulus (H). The error bars are the SEM.

Modulus (kPa)	Control $\langle L \rangle$ (μm)	KD $\langle L \rangle$ (μm)	Difference $\langle \Delta L \rangle$ (μm)
1	363 ± 6	332 ± 6	-31 ± 8
2	360 ± 5	327 ± 6	-33 ± 8*
5	375 ± 5	339 ± 5	-36 ± 7**
10	380 ± 6	347 ± 6	-33 ± 8**
20	354 ± 6	305 ± 4	-49 ± 7***
50	304 ± 5	254 ± 4	-50 ± 6***
100	267 ± 4	206 ± 3	-61 ± 5***

Table 4.14: The ensemble-averaged distance travelled $\langle L \rangle$ with their standard error on the mean (SEM) for control and knockdown (KD) cells on increasing collagen substrate moduli. The last column shows the difference of $\langle L \rangle$ between the control and KD cells.

Following this, we then looked to see if the bimodal behavior of these cells was also present on the collagen substrates, first by plotting histograms of t_m, the average time a cell is in motion, and using this data to compute an ensemble-averaged time in motion, $\langle t_m \rangle$ (Figure 4.10 A-G). We noticed qualitatively similar behaviour for the dependence of $\langle t_m \rangle$ on modulus and cell type that was previous observed for $\langle \Lambda \rangle$ and $\langle L \rangle$: a decreasing value of $\langle t_m \rangle$ for moduli away from the optimal value. We found that the maximum value of $\langle t_m \rangle$ was 560 ± 6 minutes on the 10kPa substrate, compared to the maximum value of 574 ± 2 minutes on the 0.5kPa silicone substrate. This apparent shift in the maximum value of $\langle t_m \rangle$ was in quantitative accord with the shifts seen in the other quantities, for which the cells seemed to have an optimal modulus of 10kPa on the collagen substrates. Moreover, $\langle t_m \rangle$ subsequently decreased with increasing substrate modulus to a minimum value of 478 ± 4 minutes on the 100kPa substrate, a minimum value that was lower on this substrate than the corresponding minimum value on the 64kPa silicone substrate, in qualitative accord with expectations for a higher modulus substrate. As before, we were able to standardize the control and knockdown datasets across all of the substrates to have a single master curve define them (Figure 4.11 A & B).

We also noticed qualitatively similar behaviour with the average moving speed ($\langle s_m \rangle$) on these collagen substrates. In particular, the most pronounced changes in these values were seen on either side of the optimal modulus. However, the differences in average moving speed between control and knockdown cells, while present, are less pronounced and do not account for the substantial reduction in overall motility seen with the average distance travelled. This further emphasizes that the primary factor dictating the motility patterns in knockdown cells is the reduced time spent moving rather than a marked decrease in their speed. Thus, the punctuated motility observed is more attributable to the temporal dynamics of movement rather than the cells' inherent speed on the substrates, as found with the silicone substrates.

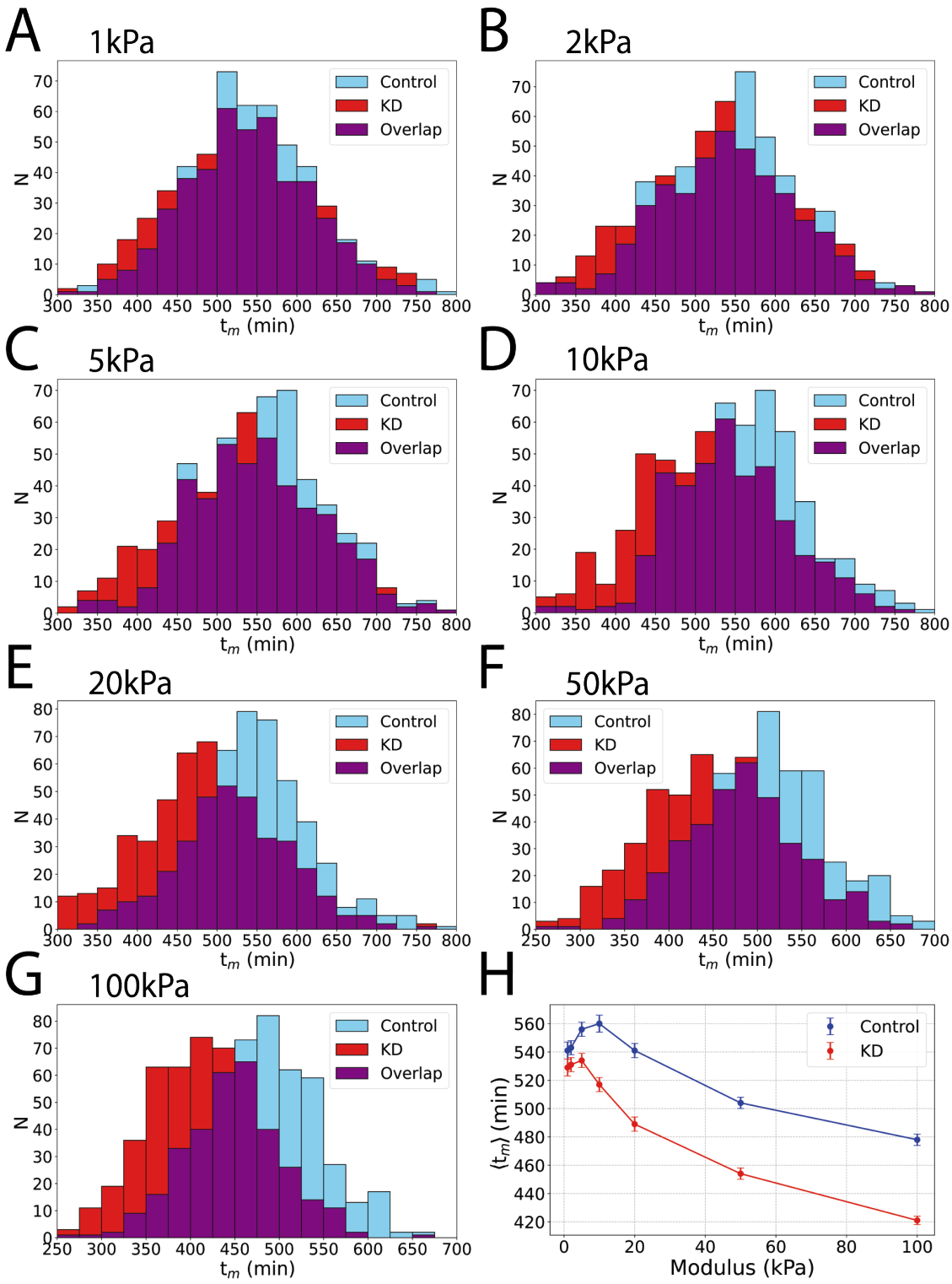

Figure 4.10: The average time spent in motion (t_m) by control (Blue) and knockdown (KD - Red) cells on the collagen substrates. Figures A-G are for the 1kPa, 2kPa, 5kPa, 10kPa, 20kPa, 50kPa, and 100kPa substrates respectively. $\langle t_m \rangle$ a function of substrate modulus (H).

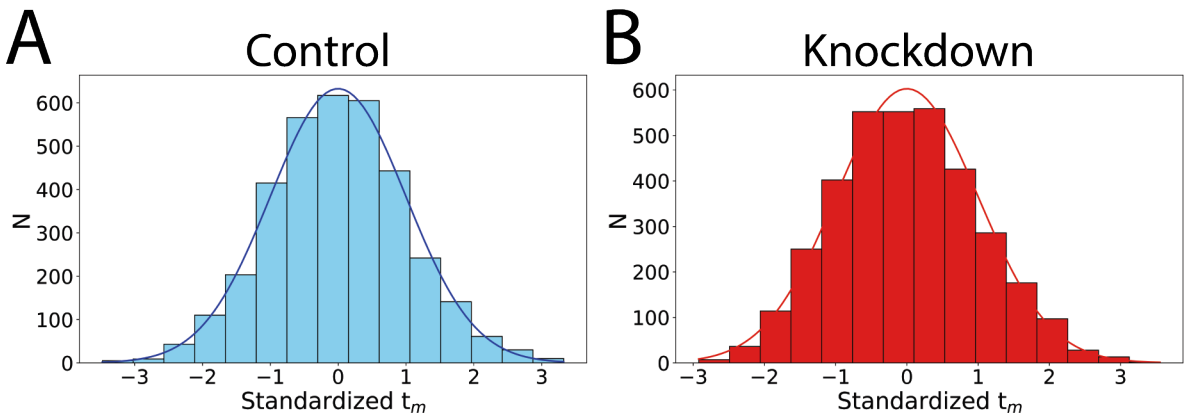

Figure 4.11: The standardized datasets for t_m from all substrates for the control and KD populations.

Modulus (kPa)	Control $\langle t_m \rangle$ (min)	KD $\langle t_m \rangle$ (min)	$\langle \Delta t_m \rangle$ (min)
1	541 ± 6	529 ± 6	-12 ± 8*
2	543 ± 5	531 ± 5	-12 ± 7*
5	556 ± 5	534 ± 6	-22 ± 7**
10	560 ± 6	517 ± 5	-43 ± 7***
20	541 ± 5	489 ± 5	-52 ± 7**
50	504 ± 4	454 ± 4	-50 ± 5***
100	478 ± 4	421 ± 3	-57 ± 5***
Master Curve	Mean	StDev	SEM
Control	540	80	4
KD	480	90	5

Table 4.15: A summary of the ensemble-averaged time spent in motion ($\langle t_m \rangle$) for the control and knockdown (KD) cells on the bio-mimetic collagen substrates. The error shown is the SEM. The final column is the difference of $\langle t_m \rangle$ between the control and KD values. *p<0.05, **p<0.01, ***p<0.001, ****p<0.0001

Modulus (kPa)	Control $\langle s_m \rangle$ (μm/h)	KD $\langle s_m \rangle$ (μm/h)	$\langle \Delta s_m \rangle$ (μm/h)
1	40.3 ± 1.4	37.6 ± 1.2	3 ± 1
2	39.8 ± 1.5	36.9 ± 1.1	3 ± 1
5	40.5 ± 1.4	38.1 ± 1.3	2 ± 1
10	40.7 ± 1.4	40.3 ± 1.6	0 ± 1
20	39.3 ± 1.3	37.4 ± 1.2	2 ± 1
50	36.1 ± 1.1	33.6 ± 1.1	3 ± 1
100	33.5 ± 1.2	29.4 ± 1.0	4 ± 1

Table 4.16: Summary of the ensemble-averaged moving speed ($\langle s_m \rangle$) for the control and knockdown (KD) cells across various substrate moduli. The error shown is the SEM. The final column is the difference of $\langle s_m \rangle$ between the control and KD values.

4.4 Discussion

A2058 cells displayed pronounced morphological changes on homogeneous substrates of varying moduli, with both silicone and collagen substrates eliciting similar responses. On softer substrates, cells adopted more circular morphologies, while on stiffer substrates, they became increasingly elongated. This change in cell shape was quantified by a decrease in roundness and was further supported by increases in both the Feret Diameter (FD) and cell perimeter (P), indicating greater cell elongation and spreading as substrate stiffness increased. Similarly, FMNL2 knockdown cells also showed enhanced elongation in response to increased substrate stiffness. These cells consistently exhibited slightly longer morphologies compared to control cells on the same substrates, as indicated by their consistently lower R values. Additionally, the average FD and perimeter values for knockdown cells were higher than those for control cells, reinforcing the observation of enhanced elongation. These behaviors suggest that cellular responses to substrate stiffness are influenced by the FMNL2 protein, aligning with findings in other cell types [16, 17]. The pronounced morphological changes in FMNL2 knockdown cells, particularly the increase in elongation, imply

a significant role of FMNL2 in cell mechanosensing. Typically, elongated cells exhibit larger focal adhesions, crucial for anchoring cells to the substrate and facilitating mechanotransduction. Given the link between FMNL2 and actin regularization [108, 109], it is plausible to hypothesize that FMNL2 is integral to the mechanosensing capabilities of these melanoma cells.

The movement of A2058 cells also showed changes on substrates of different moduli. The ensemble-averaged components of displacement vectors on all studied hydrogels were close to 0, indicative of random motion. On both the silicone and collagen hydrogel substrates, the ensemble-averaged displacement magnitudes of the cells were maximized in an intermediate range of substrate moduli. On the silicone hydrogels, their displacement reached a maximum value on the 2.0kPa substrates. While on the collagen hydrogels, this occurred on the 10kPa substrates, a noticeably larger modulus value. On substrates stiffer than these optimal values, their displacements decreased monotonically over the range of tested moduli. The existence of optimal substrate moduli were also found for maximizing other motility parameters such as the ensemble-averaged cell speed and distance travelled. On either side of these optimal moduli, these parameters monotonically decreased.

Analysis of the ensemble-averaged mean square displacement (MSD) of cells also indicates the anomalous diffusion exponent characterizing the MSD is maximized at the same optimal moduli as the other motility parameters (10kPa for collagen substrates and 0.5kPa for silicone substrates). On these substrates, the cells underwent the largest degree of super diffusive motion at the optimal moduli, and on either side of this stiffness, the MSD increased somewhat more slowly. Moreover, on any given substrate modulus, the anomalous exponent showed a maximal value midway during the total time the cells were tracked. This is manifested at early times by an apparently rapid increase of the MSD rate, followed by a regime of slowing down at late times that is consistent with other studies on cell diffusion [47]. Such behaviour may be consistent with cell division. When a cell divides, it will progressively slow down its motion during this process. Another related explanation comes from crowding effects, wherein as time goes on, the number of cells in a given region will increase, due to cell division, resulting in enhanced local inhibition of cell motion due to local confinement effects. The biphasic behaviour we observe in A2058 cells was previously

predicted by motor clutch models of cell motion [30, 31], wherein at this optimal value, the tensile forces between the cell and the substrate are maximized [26]. The biphasic behavior of A2058 cells allows us to hypothesize and predict what their durotactic behavior may show. Some cancerous cell types have been found to only exhibit durotactic behavior around their optimal stiffness [24], and beyond these regions, their durotactic potential dramatically drops. Furthermore, cells that exhibit maximal speed and distance on softer substrates typically undergo negative durotaxis on substrates with elevated stiffness beyond their optimal value [25, 26].

In the knockdown cell populations, the average displacement and distance travelled were consistently lower than the control cells on the same stiffness substrate. This effect was most noticeable on the stiffer substrates, for both the silicone and collagen substrates. This indicates that the role of FMNL2 in motility is also dependent on substrate stiffness. In previous studies, FMNL2 has been linked to the generation of protrusive forces and lamellipodium protrusion speed in B16 melanoma cells [64], and is also associated with the formation of filopodia and invasion in melanoma cells [59, 60, 63]. So, our results showing a decrease in the motility of FMNL2 suppressed cells is consistent with other studies on similar cell types. Furthermore, if the knockdown cells were unable to generate sufficient forces to facilitate mechanosensing and focal adhesion formation turnover, then this could impact their overall motion, as we found. These cells also seemed to adopt a bimodal mode of cell motility, characterized by periods of motion and cell arrest. On both sets of substrates, the ensemble-averaged time in motion $\langle t_m \rangle$ was shown to change with substrate stiffness. On the silicone substrates, a maximum value of t_m was found on the 0.5kPa substrate, where it then monotonically decreased afterwards. On the collagen substrates, a noticeable shift in the maximum once again occurred, with a maximum on the 10kPa substrate. However, the knockdown cells on both sets of substrates consistently had lower average values of $\langle t_m \rangle$.

We also calculated the ensemble-averaged cell speeds $\langle s_m \rangle$ on both sets of substrates, to see if the decreases seen in the ensemble-averages values of Λ and L were due to slower motion, or merely remaining in an arrested state for longer. The $\langle s_m \rangle$ were also found to monotonically decrease on the silicone substrates, with a maximum at 0.5kPa. A shift in this parameter was

also again noticed, with a maximum moving speed achieved on the 10kPa collagen substrate. The moving speeds on the softest substrates were similar between the control and knockdown groups, but became more pronounced on the stiffest substrates. These results also highlight once again that the role of FMNL2 in A2058 cells is dependent on the absolute stiffness of the substrate. Furthermore, the variation of $\langle s_m \rangle$ with substrate stiffness, with the existence of an apparent optimum stiffness, underlines the inherent biphasic behavior of these cells. One puzzling feature of our results is the apparent shift between the optimal modulus on the silicone and collagen substrates. On the silicone ones, the various motility parameters indicate that the optimal value is between 0.5-2kPa, while the collagen data indicates an optimal around 10kPa. These results could be explained by the differences in ligand binding sites on the substrates. The silicone gels were chemically functionalized with fibronectin, while the collagen substrates had embedded RGD sites in the protein sequence. Previous studies have indicated that the type, density and presentation of ligand binding sites can have a larger impact on cell behavior than the mechanical properties of the substrate material.

4.5 Conclusion

In this section, we found that A2058 cells exhibited pronounced changes in their morphology and motility on substrates of different moduli. On the soft substrates, the cells adopted circular morphologies that progressively became more elongated as the stiffness of the substrate increased. On both the silicone and collagen substrates, they exhibited random motion as characterized by their displacements, and also displayed a biphasic relationship with substrate stiffness. An optimal modulus was found for their motility to be between 0.5-2kPa for the silicone substrates, and around 10kPa on the collagen substrates.

In the FMNL2 knockdown cell population, similar trends in morphology and motility were observed with these cells. They became more elongated and exhibited similar biphasic behavior as the controls. Interestingly, when compared to the control cells, they were consistently more elongated, and they were found to travel smaller distances, and spend less time in motion, with these effects being more pronounced on the stiffer substrates. Overall, these results seem to

indicate that FMNL2 plays a role in the actin characteristics of A2058 melanoma cells, as shown by the changes in morphology and motility. The role that FMNL2 does play also seems to be dependent on the stiffness of the substrate as well, with higher moduli substrates showing more pronounced knockdown behaviors.

Proceeding into the next chapter, we will now transition to cell motion on collagen hydrogels with a gradient in their modulus. We will be able to compare the data analyzed here with their motion on the gradient substrates to see if any noticeable changes are seen, and if A2058 cells do respond in any way to a stiffness gradient.

Chapter 5

Cell Motion on Gradient Substrates

5.1 Introduction

Durotaxis, as described in chapter 2, refers to the directed migration of cells in response to gradients in substrate stiffness. This phenomenon was first described in the context of fibroblast movement on substrates with varying rigidity, where cells preferentially migrated toward stiffer regions. Durotaxis studies have typically been performed in-vitro, utilizing synthetic substrates such as polyacrylamide, which have well establish protocols for creating gradients [112].

Numerous studies have found a number of cell lines that exhibit stiffness guided migration, with the vast majority showing evidence of positive durotaxis [25, 113]. However, other cell lines have been found to display behavior different than this, with some cell lines exhibiting adurotactic behavior [114], where they are unable to sense the change in stiffness, and some showing negative durotactic behavior. Negative durotaxis has been found primarily in cancerous cell lines [33, 113], and could be a key factor in understanding the 'migration paradox' created by cancer metastasis [25]. This paradox refers to cancer cell's ability to metastasize and invade other healthy tissue, when they must cross a stiff to soft boundary, as cancerous tissues are often much stiffer than their neighbouring healthy tissue. Cells preferentially migrating along this gradient would be undergoing negative durotaxis, which contradicts the positive durotactic behavior observed in most cell lines. Quantitative motility studies of cancerous cell lines exhibiting this behavior could play an important role in understanding cancer invasion.

The motor clutch model, described in chapter 2, provides insight into durotactic behavior of different cell lines. This model describes how cells interact with ligand binding sites in their ECM and generate 'clutches', that can engage and disengage with binding sites to facilitate motion [31, 115]. This process requires the generation of contractile forces with the ECM, and stiffer substrates allow for larger forces to be generated, resulting in more engagement with the substrate and more effective motion. On softer substrates, clutch formation with the ECM would be reduced, resulting in smaller contractile forces that affect the stability of the clutches. So, this model would then predict motion in the direction of increasing stiffness (positive durotaxis), as this would optimize their ability to migrate and their stability with their substrate [30]. However, the motor clutch model also predicts cells having a biphasic response to substrate stiffness, where they can find an optimal stiffness region to maximize force generation with the substrate [30, 115]. This response has been illustrated in some cell lines including U251-MG glioblastoma cells, where they exhibited both positive and negative durotaxis on either side of their optimal stiffness [26]. For cell lines that have a stiffness optimum at an intermediate stiffness range, this model then predicts preferential motion from a stiffer region down to their optimal region (negative durotaxis).

A key protein implicated in the durotactic behavior of melanoma cells is Formin-like 2 (FMNL2). FMNL2 is a member of the formin family of proteins, which are involved in the regulation of actin dynamics and the formation of cellular protrusions such as filopodia and lamellipodia. FMNL2 promotes actin polymerization at the leading edge of migrating cells, facilitating the formation of protrusions that enable cells to navigate through the ECM [116]. In melanoma cells, FMNL2 expression is associated with increased migratory and invasive capabilities. It has been shown that FMNL2 enhances the formation of cell protrusions, contributing to the ability of melanoma cells to respond to mechanical cues and migrate toward stiffer substrates [63, 117, 118, 119]. Furthermore, FMNL2 has been implicated in the regulation of focal adhesion dynamics and integrin signaling in melanoma cells [58]. By modulating the turnover and maturation of focal adhesions, FMNL2 influences the cell's ability to generate traction forces and migrate in response to substrate stiffness [64]. This regulation is critical for the durotactic migration of melanoma cells, as it enables them to sense and respond to the mechanical properties of their environment

[57].

In the previous chapter, we characterized the morphological and motility based behaviors of A2058 cells on homogeneous moduli substrates. We also looked at the effects of suppressing the protein FMNL2, and found it to have an impact on cell motion. In this chapter, we will now look at the motion of the same cells on substrates with a gradient in their modulus. We will utilize the methods discussed in chapter 3 to fabricate collagen hydrogels with multiple known stiffness gradients with a range of biologically relevant moduli. Using these we can analyze the motion of A2058 cells across a large range of moduli to see how the absolute stiffness affects their behavior. Simultaneously, we can also fabricate substrates with multiple gradient strengths to see how that impacts their motion in all of the imaged regions. Finally, the effect of suppressing FMNL2 will be explored to see if analogous motility behaviour identified in the previous chapter are observed, and if FMNL2 impacts durotactic behavior in A2058 cells.

5.2 Methodology

5.2.1 Cell Culture

A2058 (CRL-11147) metastatic melanoma cells were obtained from the Copeland lab in the Faculty of Medicine at the University of Ottawa. The cells were cultured in Dulbecco's modified Eagle's medium containing 10% fetal bovine serum. Cells were kept at $37°C$ in 5% CO_2. Cells were used for experiments until passage number 12.

siRNA-mediated knockdown was performed by Sarah Fox from the Copeland lab, as previously described [59] using Dharmafect1 (Horizon Discovery Ltd; T-2001-03) and the following siRNA duplexes: FMNL2 siRNA Duplex1 (IDT; hs.Ri.FMNL2.13.1); FMNL2 siRNA duplex2 (IDT; hs.Ri.FMNL2.13.2).

5.2.2 Hydrogel Preparation

Gradient modulus collagen-mimetic hydrogel substrates were prepared from mixtures of VB and VB-RGD proteins as described in chapter 3 using genipin diffusion, with a final protein ratio of

19:1 (VB:VB-RGD). Four different substrates were made with gradient strengths of approximately 3kPa/mm, 10kPa/mm, 20kPa/mm, and 40kPa/mm by altering the allowed diffusion time. The fabricated substrates were then immediately washed in PBS multiple times, and placed onto a shaker plate overnight in fresh PBS. This PBS was then removed, the gel washed three more times, and then placed into the cell incubator with Dulbecco's modified Eagle's medium for 3 hours prior to the addition of cells.

5.2.3 Live Cell Imaging

Imaging was performed using a Nikon Eclipse Ti-S microscope with an in-house designed image acquisition system. A 4X and 10X lens were used to acquire images at an interval of 10 minutes for up to 48 hours. Cells were kept in a 37°C and 5% CO_2 for the duration of the experiment.

5.2.4 Motility Analysis

The motility analysis was performed as described in chapter 4 section 4.2.5. Additionally, the orientation of cells along the gradient axis was quantified by the orientational order parameter described in chapter 2, utilizing equations 2.7 and 2.8. Additional durotaxis metrics were also calculated as discussed in chapter 2.

5.2.5 Statistical & error analysis

Statistical and error analysis was performed as previously described in chapter 4 section 4.2.6. Three knockdown trials were performed, with the results shown being the average of all three trials. For the control data, the results are the average of N = 3 trials for each substrate.

5.3 Results

5.3.1 Control A2058 Cell Behavior

To characterize the motion of A2058 cells on gradient stiffness substrates, we created bio-mimetic collagen protein substrates using the methods established in chapter 3. We studied the impact

of the gradient strength, as well as the absolute stiffness, to determine how these cells responded to the gradient. Starting off, we investigated the effect of a modest 2.5kPa/mm stiffness gradient on control A2058 cells. In Figure 5.1 below, we have plotted a comparison between cell motion on a gradient and homogeneous substrate with a modulus similar to the mean value of the ROI analyzed for the gradient substrate. The gradient region analyzed in this figure is a soft region, with a mean modulus of approximately 2kPa. Table 5.1 below presents the average components of cell velocity as well as the average angular displacement corresponding to the plots in Figure 5.1. Two additional figures with the same structure as Figure 5.1 are located in Appendix B, and show the results from two stiffer regions of the hydrogel with the same gradient strength.

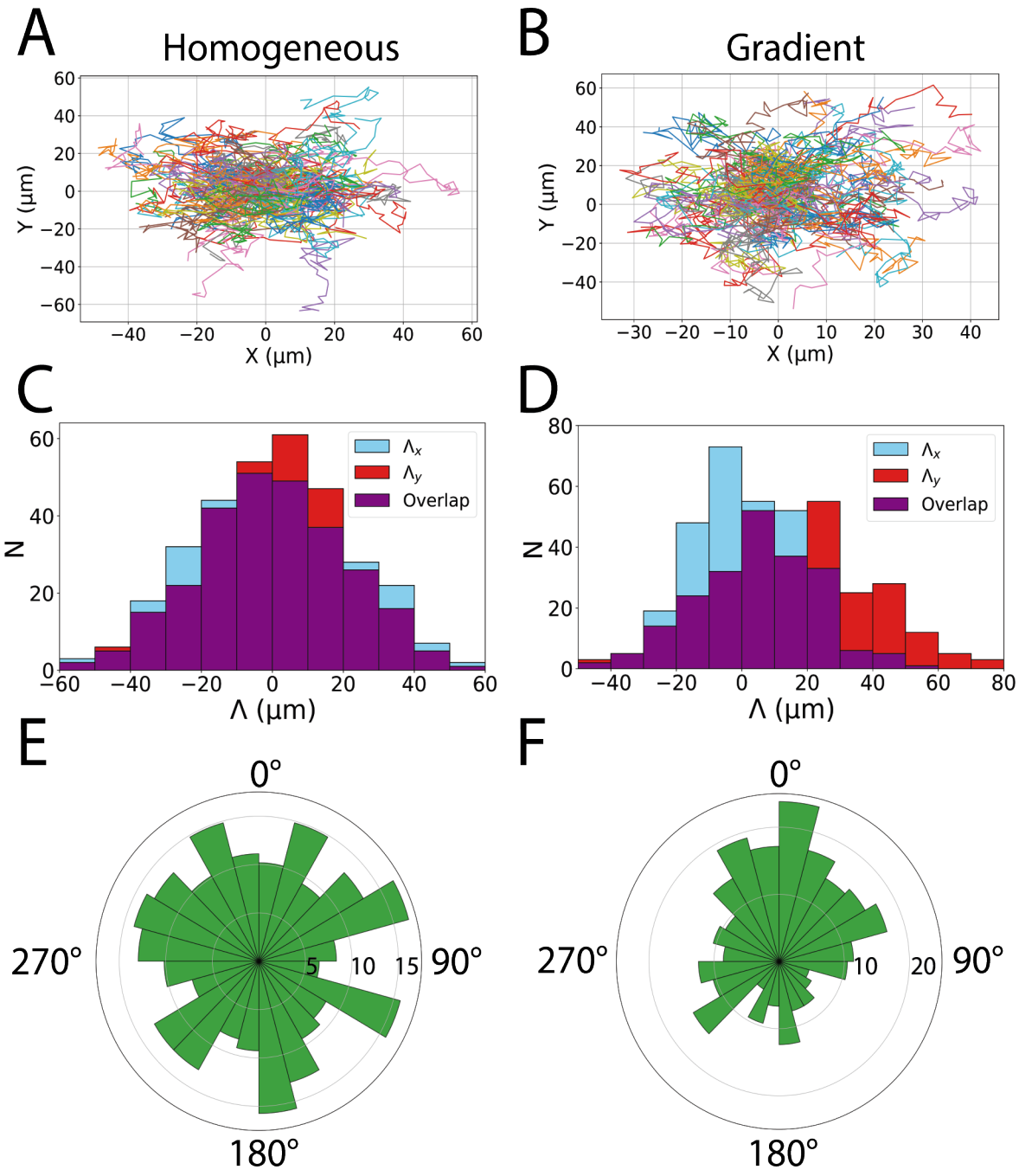

Figure 5.1: A comparison between cell motion on a homogeneous 2kPa substrate and a gradient substrate in a 2kPa region with a gradient strength of 2.5kPa/mm. Figures A and B compare the cell tracks of cells on homogeneous (A) and gradient (B) substrates. Figure C and D compares the displacement along x (Λ_x) and y (Λ_y). Figures E and F compare the angular displacement of cells on both substrates.

Qualitatively comparing the the cell tracks (Figures 5.1 A and B) plotted for the gradient and

	Homogeneous		Gradient		Differences	
Modulus (kPa)	v_x (μm/h)	v_y (μm/h)	v_x (μm/h)	v_y (μm/h)	Δv_x	Δv_y
2	0.2 ± 0.04	0.6 ± 0.08	0.1 ± 0.04	10.4 ± 0.4	-0.1 ± 0.06	9.8 ± 0.4*

Table 5.1: A summary of the velocity components perpendicular (v_x) and parallel (v_y) to the gradient. The final two columns indicate the difference between the gradient and homogeneous velocities, *p <0.0001.

homogeneous substrates shows no striking differences between the two substrates tested. So, we then plotted histograms showing the cell's final displacement coordinates in x and y directions to compare the data (Figures 5.1 C and D). Along the x-direction (perpendicular to the gradient) the motion was inherently random as the average displacement was close to 0, while in the y-direction (parallel to the gradient), there was a shift in the distribution towards a positive value, showing preferential motion here in the positive gradient direction towards a stiffer region. Furthermore, when we compare cell velocities between the substrate, we see that in the x-direction, there was no significant difference, while in the y-direction, there was a statistically significant shift to a larger value ($\Delta v_y = 9.8 \pm 0.4$). These results are then further corroborated by the noticeable change in the final angular displacement (Figures 5.1 E and F), with it having a tighter distribution around zero degrees, whereas the distribution on the homogeneous substrate is more uniform. These quantities thus indicate then that in this region, there was preferential motion by the cells in the direction of increasing stiffness.

We then investigated the impact of local stiffness on the behavior of these cells. To do this, we analyzed local cell motion on substrates with a wide range of modulus levels between 3-40kPa in the presence of a modest gradient strength of 3kPa/mm across the sample, and utilized the durotactic index (DI) from chapter 2 as a motility metric. Figure 5.2 shows the DI of cells along the x and y direction for different regions of the sample, with Table 5.2 summarizing the results.

Modulus (kPa)	DI_x	DI_y
3 - 10	0.03 ± 0.01	0.15 ± 0.01
10 - 15	-0.02 ± 0.01	0.09 ± 0.01
15 - 20	-0.03 ± 0.01	0.03 ± 0.01
20 - 25	0.03 ± 0.01	-0.01 ± 0.01
25 - 30	-0.04 ± 0.01	-0.05 ± 0.01
30 - 35	0.02 ± 0.01	-0.08 ± 0.01
35 - 40	-0.01 ± 0.01	-0.10 ± 0.01

Table 5.2: Average durotactic index (DI) in the x and y directions, DI_x and DI_y, with standard error of the mean (SEM), across different modulus ranges for a gradient strength of 3kPa/mm along the y direction.

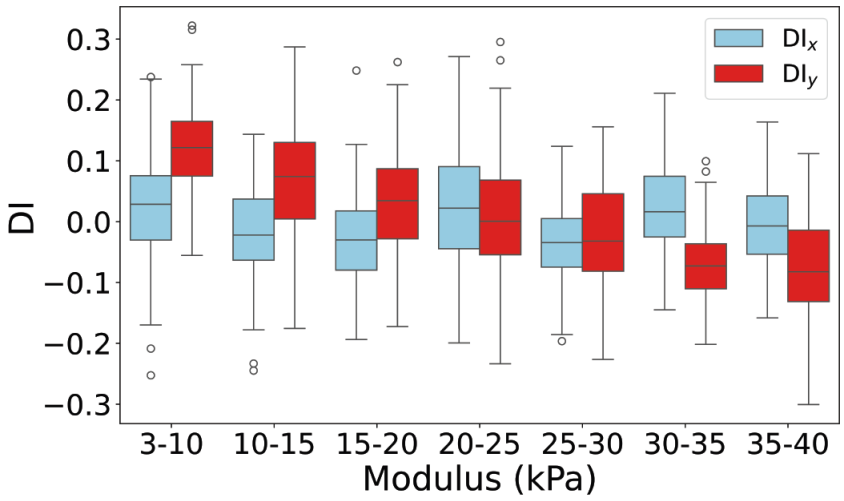

Figure 5.2: The durotactic index (DI) along the x and y direction of the substrate with a gradient strength of 3kPa/mm along the y direction.

On all regions of this substrate, the value of DI_x was close to 0, indicating no directed motion as expected. In the softest region of the substrate, we found that DI_y was 0.15 ± 0.01, indicating that positive durotaxis was occurring in this region. With increasing modulus, however, DI_y monotonically decreased toward zero (between 20 and 25kPa), indicating a progressive decrease in positive durotactic behaviour. Interestingly, increasing modulus beyond this region we found that there was the emergence of negative DI_y values, indicating a tendency for the cells to move in the direction of decreasing substrate stiffness (negative durotaxis). These results are reminiscent of the biphasic behavior noticed in the previous chapter, where cell behavior changed on either side of the optimal stiffness value between 5-10kPa. It appears that the motion of these cells is

biased towards regions of their optimal stiffness, leading to both positive and negative durotactic behaviour depending on the local stiffness of their environment relative to the optimal stiffness value.

We then investigated the impact of gradient strength on the motion these cells, utilizing substrates with gradient strengths of 1kPa/mm, 3kPa/mm, 10kPa/mm, and 20kPa/mm, in soft, optimal, and stiff regions of the substrates. The durotactic index DI_y for these gradient substrates are shown in Figure 5.3. We also utilized the orientational order parameter (S), defined in chapter 2, to quantify the alignment of cells along the gradient for these substrates (shown in Figure 5.4). The histograms in Figure 5.4 are for the soft region of the substrate only, with additional figures (Figure B.3 and Figure B.4), showing the histograms for the optimal and stiff regions.

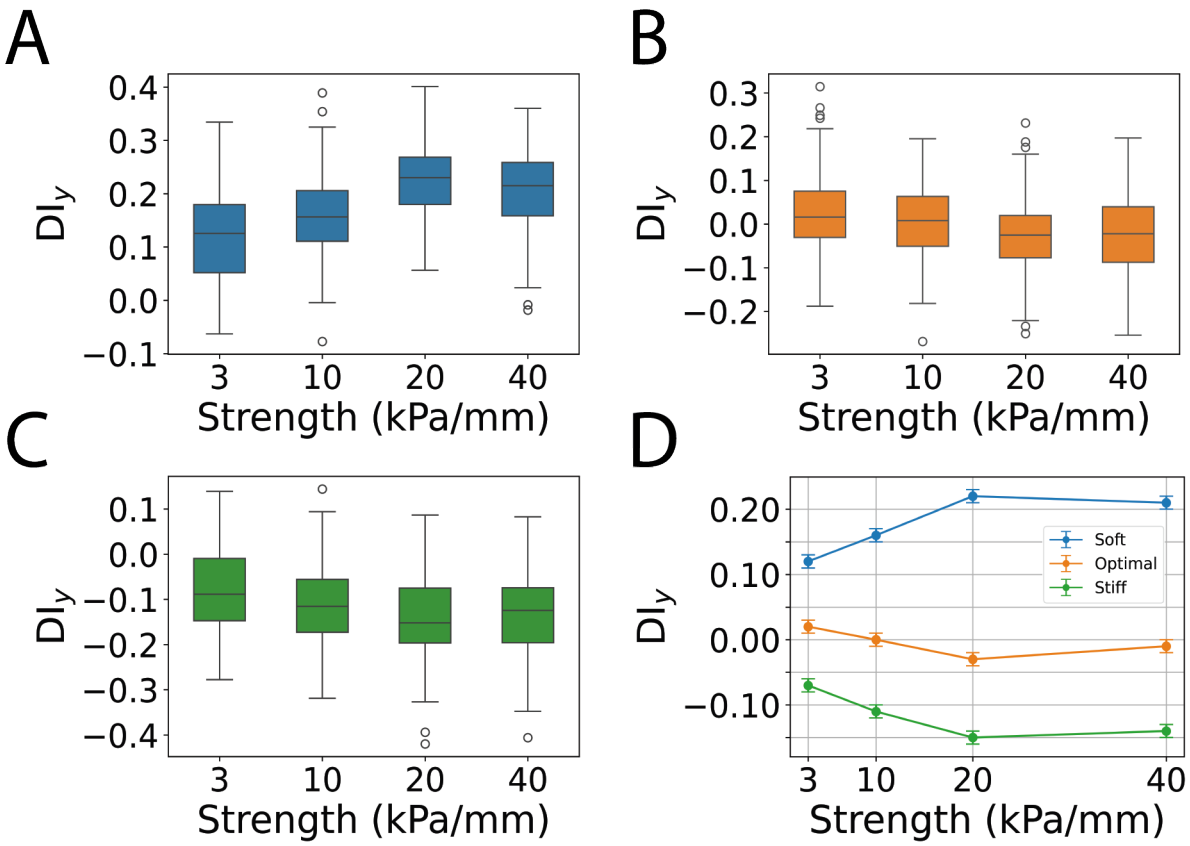

Figure 5.3: A, B, C shows the durotactic index along the gradient (DI_y for the soft (5-15kPa), optimal (15-25kPa), and stiff (>25kPa) respectively with different gradient strengths. D summarizes DI_y as a function of gradient strength for all samples in one plot. Data shown in each plot is the average of N = 3 samples. The error bars on the box plot indicate the standard deviation, while the points in D use the SEM.

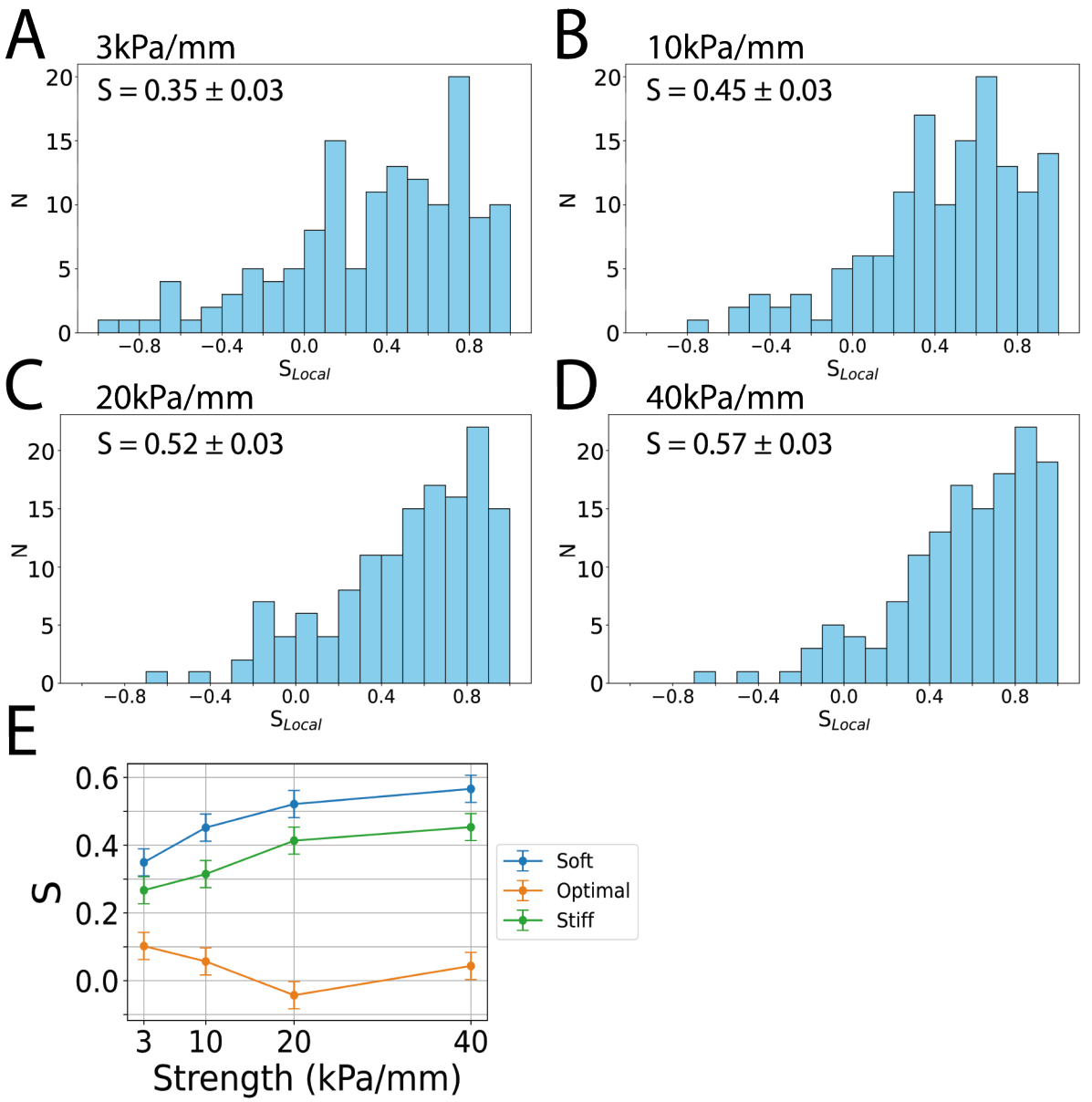

Figure 5.4: A, B, C, and D shows example distributions of the orientational order parameter for each cell (S_{Local}) on substrates with gradient strengths of 3, 10, 20 and 40 kPa/mm respectively, in the soft region (5-15kPa) of the samples. E summarizes the average value of the distribution for each gradient strength, S=$\langle S_{Local} \rangle$, plotted as a function of gradient strength for soft (5-15kPa) samples. The errors bars are the standard error on the mean. Each plot is the average of N = 3 samples.

As shown in Figure 5.3, the value of DI_y increased (becoming more positive) up to a gradient strength of 20kPa/mm on the (soft) 5-15kPa samples, before eventually saturating at high

gradient strengths. Likewise, the value of DI_y decreased (becoming more negative) up to a gradient strength of 20kPa/mm on the (stiff) >25kPa samples, before eventually saturating at high gradient strengths. For the intermediate stiffness samples, DI_y remains near zero with increasing gradient strength, as would be expected for cells on an "optimal" stiffness substrate. Figure 5.4 shows a similar behaviour for cell alignment, where the value of S monotonically increased with the gradient strength on the soft and stiff regions of the substrate, whereas the cell alignment along the gradient remains weak on the intermediate (optimal) stiffness samples. This behavior indicates that the cells on substrates that are sufficiently softer or stiffer than a characteristic optimal stiffness did respond to the increase in gradient strength by becoming more aligned along the gradient, and that the strength of the gradient in modulus amplifies this effect for modest gradient strengths (<20kPa/mm).

We now focus on the response of cells to a relatively strong modulus gradient over a wider range of local substrate modulus (up to 90kPa). Figure 5.5 shows the value of DI_y as a function of stiffness on a 40kPa/mm substrate.

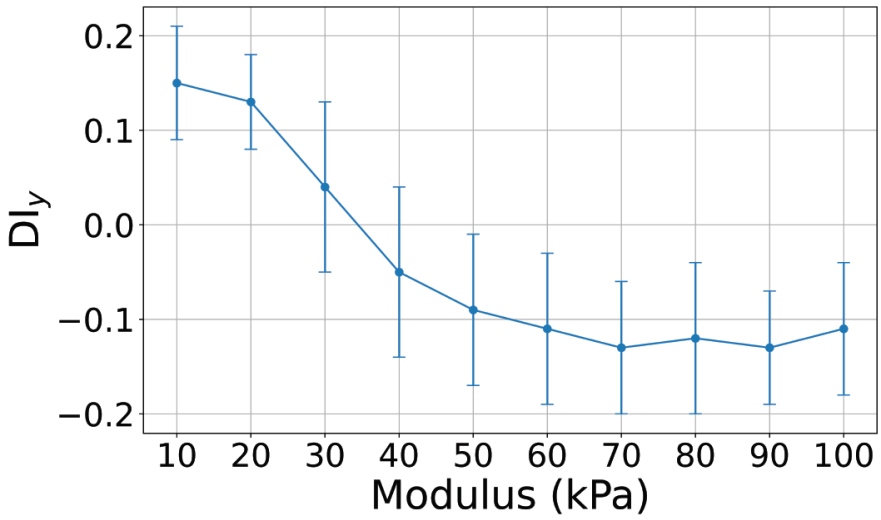

Figure 5.5: The value of DI_y as a function of the substrate modulus for a 40kPa/mm modulus gradient. Error bars are the standard error on the mean, and the average of N = 3 samples is shown.

The figure shows that the durotactic index along the gradient direction monotonically decrease up until saturating at a value of -0.11 ± 0.04 at around 60kPa. We next characterized how

ensemble-averaged cell velocity was impacted by the gradient. Figure 5.6 shows a plot of the magnitude of the ensemble-averaged cell velocity as a function of the substrate modulus.

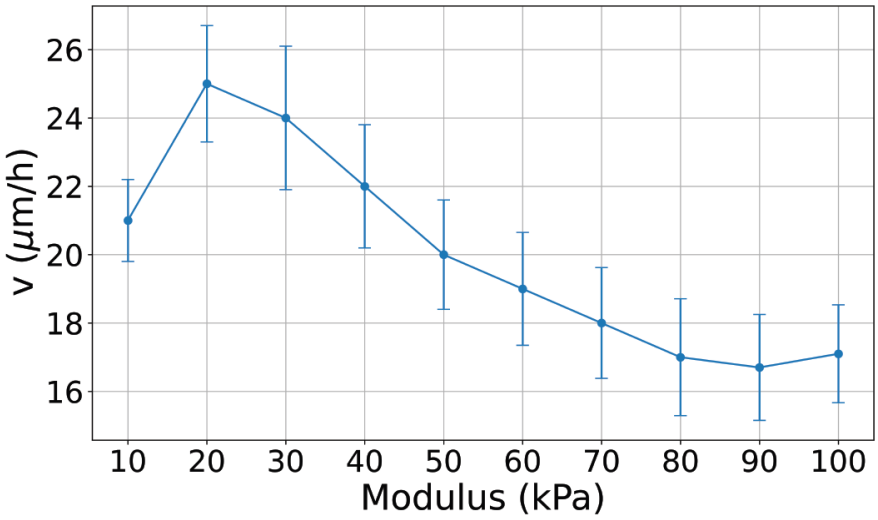

Figure 5.6: The average magnitude of cell velocity (v) on different regions of substrate stiffness for a 40kPa/mm modulus gradient. The errors bars indicate the SEM, and the data is the average of N = 3 samples.

As shown, cell velocity peaked in the region of optimal stiffness, where there was the least durotactic behavior. On either side of this region, the velocity monotonically decreased. This indicates that the cell populations with the most pronounced durotactic behavior actually moved slower than the cells exhibiting adurotactic behavior. Evidently, the magnitude of velocity of these cells is not a suitable metric of their durotactic potential. To further characterize the impact the gradient had on cell motility, we calculated the MSD of the cells on the substrates as a function of the gradient strength, for soft (5-15kPa), optimal (15-25kPa), and stiff (25-40kPa) substrates. Figure 5.7 shows the cumulative anomalous MSD exponent α as a function of lag time for the three stiffness regimes and four stiffness gradient values.

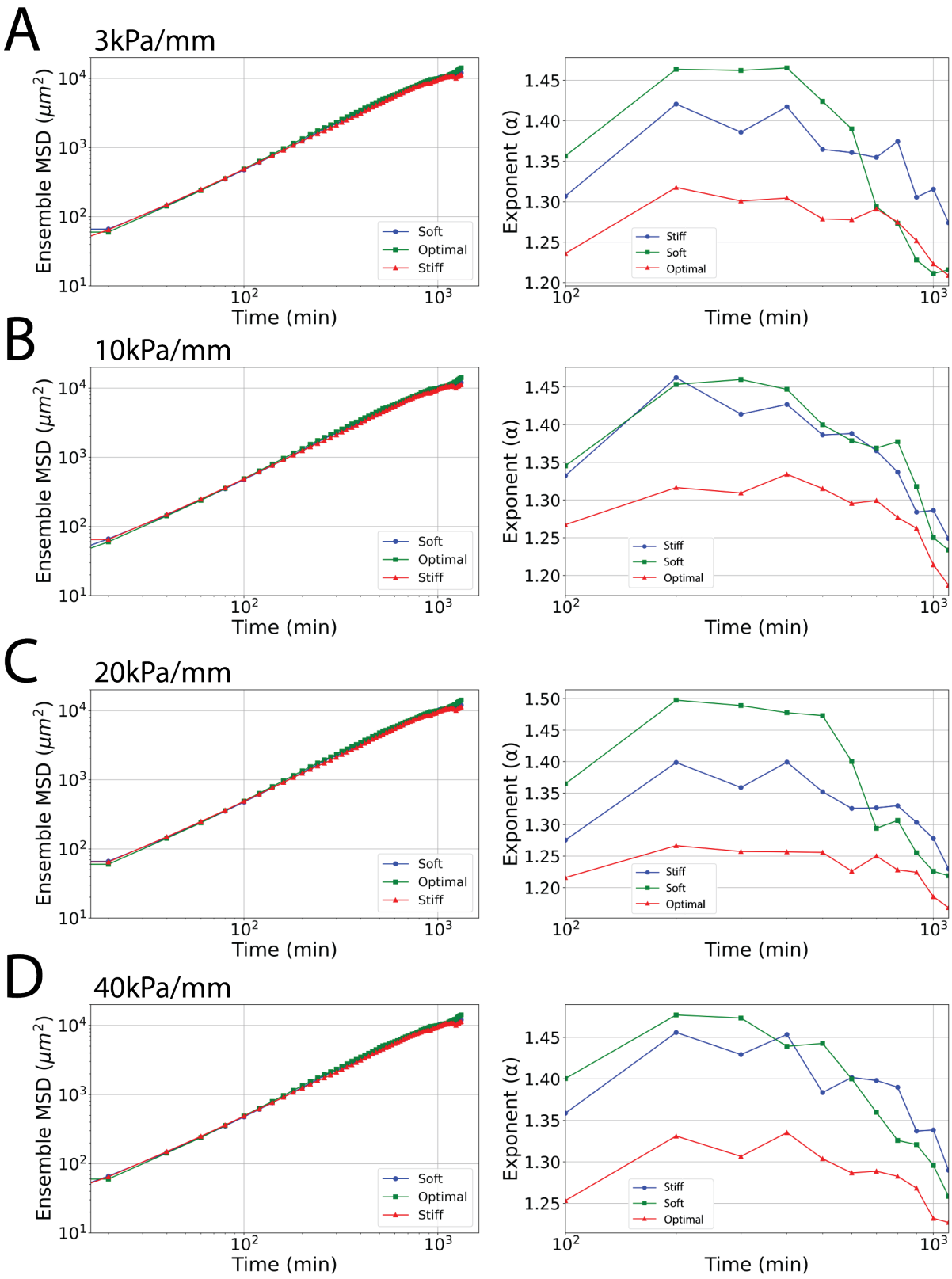

Figure 5.7: A, B, C, and D are plots of the ensemble MSD (left) and cumulative diffusion exponent (α) (right) as a function of time, for gradient strengths of 3kPa/mm, 10kPa/mm, 20kPa/mm, and 40kPa/mm. Each plot is the average of N = 3 trials.

The MSD behavior of the cells was qualitatively similar to that on homogeneous substrates (as shown in Figure 4.8), but did seem to be impacted by the gradient strength in each of the three regions. Specifically, the anomalous exponent increased from 1.2 to 1.4 in the soft region, 1.3-1.4 in the optimal region, and 1.1-1.3 in the stiff region, indicating increased superdiffusive behavior. This indicates that when the cells were undergoing durotaxis, they were more superdiffusive than when they were undergoing negative durotaxis.

5.3.2 FMNL2 Knockdown Effects

Following the studies of control cells on the gradient substrates, we now investigate the potential effects of knockdown of FMNL2 on the durotactic behavior of A2058 cells. As with the control (WT) A2058 cells, we study the knockdown (KD) cell motility in soft, optimal, and stiff regions of the substrate for prescribed substrate modulus gradient strength. Due to the nature of knockdown experiments, where the efficacy of the knockdown decays with time, we could only investigate one gradient strength in order to film the cells for an adequate amount of time. So, a gradient strength of 10kPa/mm was chosen, as this was adequate to induce durotactic behavior in the control cells, while simultaneously providing a soft, optimal, and stiff region to be studied between 5 and 70kPa. The first quantities we examined were the cell displacements and durotactic indices along the gradient. Figure 5.8 presents histograms of displacement data and a comparative plot of the DI along the gradient direction for the three stiffness regions, with Table 5.3 giving a summary of these results.

	WT			KD			Differences		
Region	Λ_y (μm)	Λ (μm)	DI_y	Λ_y (μm)	Λ (μm)	DI_y	$\Delta\Lambda_y$ (μm)	$\Delta\Lambda$ (μm)	Δ DI_y
Soft	46 ± 2	115 ± 4	0.11 ± 0.01	40 ± 3	92 ± 4	0.08± 0.01	-6 ± 4	23 ± 6***	-0.03 ± 0.01
Optimal	8 ± 4	118 ± 5	0.00 ± 0.01	2 ± 5	99± 5	0.02 ± 0.01	-6 ± 6	19 ± 7***	0.02 ± 0.01
Stiff	38 ± 3	104 ± 4	-0.08 ± 0.01	28 ± 5	83 ± 5	-0.06 ± 0.01	-10 ± 6*	21 ± 6***	0.02 ± 0.01

Table 5.3: A summary of the displacements (Λ_y) along the gradient direction, the net displacement (Λ), and the durotactic index along the gradient (DI_y) for wild type (WT) and knockdown (KD) cells on a 10kPa/mm substrate in soft (5-15kPa), optimal (15-25kPa), and stiff (>30kPa) regions. The shown error is the SEM, *p <0.05, ***p <0.001.

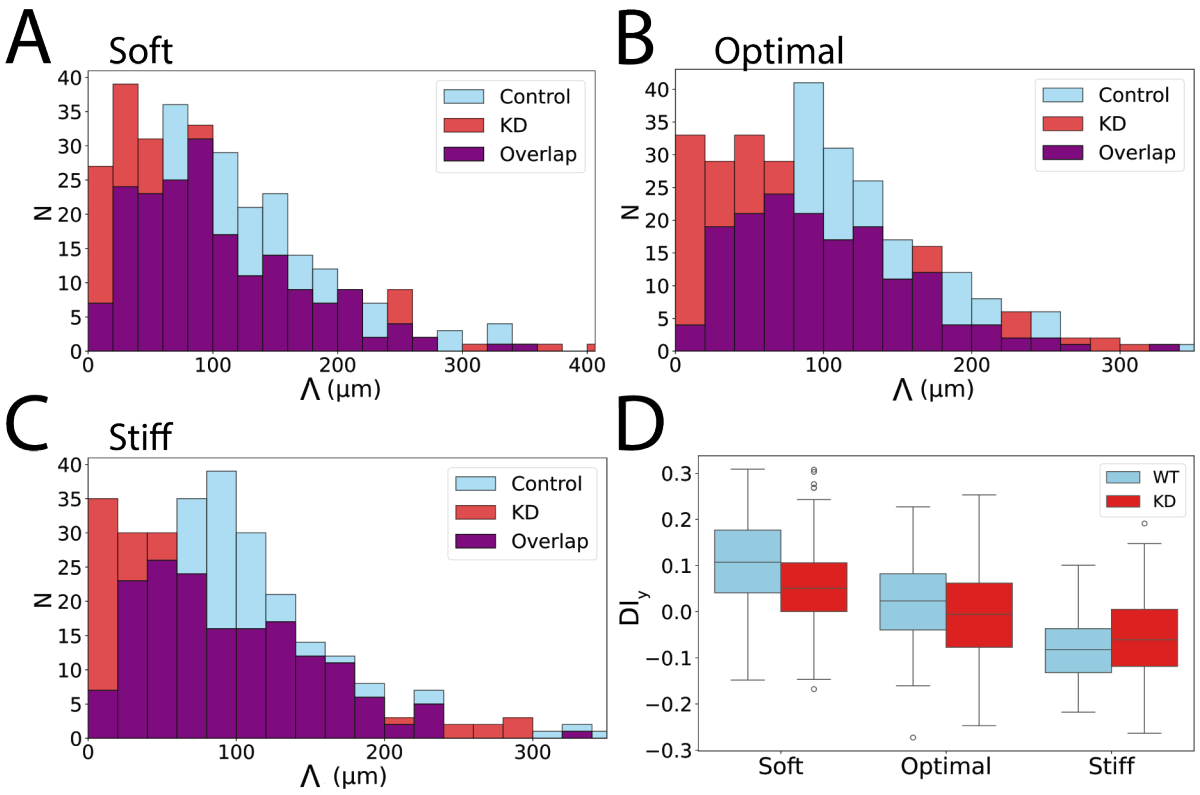

Figure 5.8: Histograms of wild type (WT) and knockdown (KD) cell net displacements (Λ), in different regions of a 10kPa/mm substrate (A,B,C). D shows the value of the DI along the gradient direction (DI_y). These results are the average of N = 3 KD trials.

In these results, we found that the KD cells had minor changes in the average displacement along the gradient direction ($\langle\Lambda_y\rangle$) with only the stiff region having a significant difference. However, only one of these changes (in the stiff region), was statistically significant. If we instead look

Region	WT S	KD S	ΔS
Soft	0.45 ± 0.03	0.39 ± 0.04	-0.06 ± 0.05
Optimal	0.08 ± 0.05	0.11 ± 0.05	0.03 ± 0.07
Stiff	0.51 ± 0.04	0.43 ± 0.05	-0.08 ± 0.06*

Table 5.4: A summary of S for WT and FMNL2 KD Cells in the soft, optimal, and stiff regions of the substrate. *p<0.05

at the average total displacement magnitude ($\langle\Lambda\rangle$), we see statistically significant changes in all studied regions, similar to what was found in chapter 4. The value of DI_y was also above positive in the soft region, and negative in the stiff region, suggesting that they still underwent (positive and negative) durotaxis. However, when we compare the value of DI_y between the WT and KD cells, we see that in the KD populations, its value is consistently smaller. To further characterize durotactic behavior, we then analyzed the order parameter S, to see how well the cells aligned with the gradient.

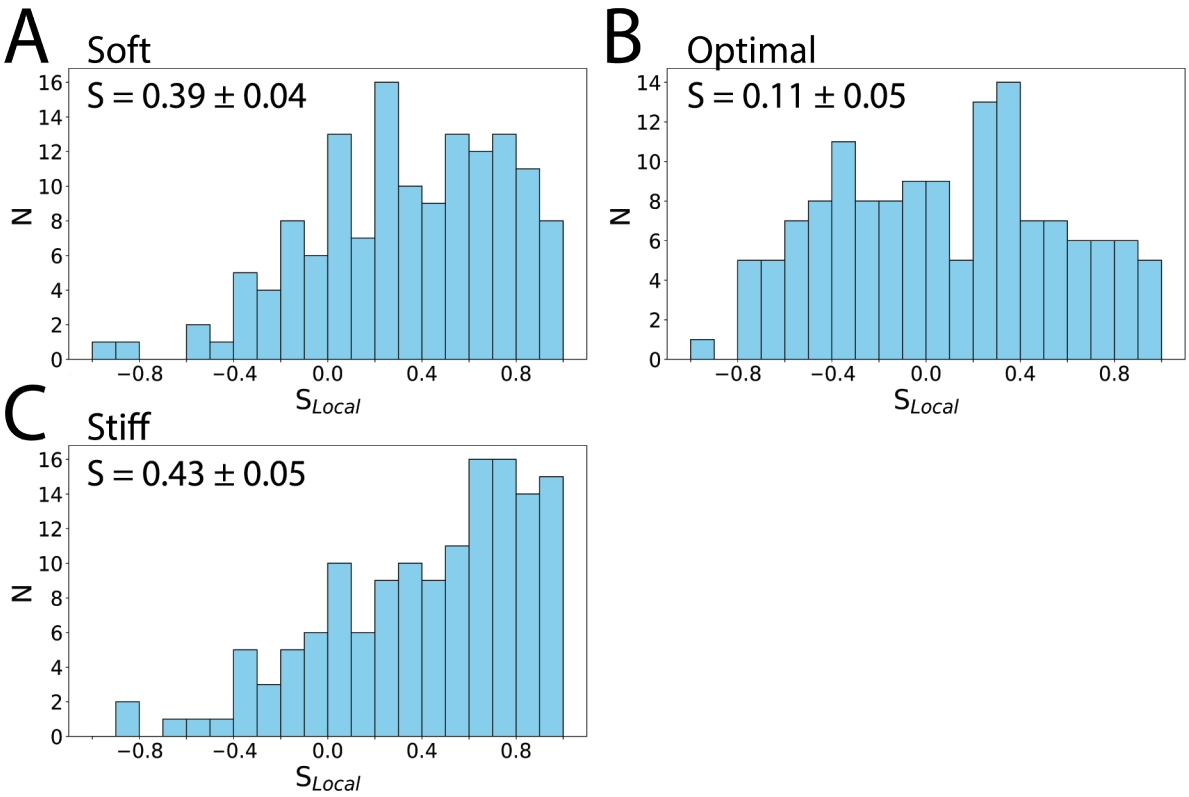

Figure 5.9: Histograms of S_{Local} for knockdown (KD) cell populations, in different regions of a 10kPa/mm substrate (A,B,C).

These results show that the KD cells are significantly aligned along the axis of the gradient

direction in both the soft and stiff regions, as in the case of the control WT cells. Moreover, the value of S is close to zero in the optimal region, indicating a lack of alignment, in accordance with the results for the WT cells. Comparing the WT and KD values of S in Table 5.4, we see that KD cells exhibited somewhat lower alignment in the soft and stiff regions. However, statistical testing revealed that this difference in alignment was only significant in the stiff region. We next analyzed the angular displacement of the KD cells on the same soft, optimal, and stiff substrates, as shown in Figure 5.10. The angular displacement distributions of the KD cells on these substrates (Figure 5.10A) were found to qualitatively similar to those found for WT cells (Figure 5.10B). In the KD cells, their durotactic behavior seemed to be slightly reduced, as shown by the broadening of the angular displacement distributions. However, the KD cells still show durotactic behavior, with the majority of the cells in the soft and stiff regions having a net displacement in the positive or negative direction along the gradient respectively.

These results for cell displacement, angular displacement, durotactic index, and orientational order parameter all support the conclusion that the knockdown cells undergo durotaxis on the soft and stiff substrate regions, while exhibiting adurotactic behaviour on the optimal stiffness regions, as was found for the WT cells. Quantitatively, it was found that KD cells exhibited a more muted durotactic response compared to the control A2058 cells.

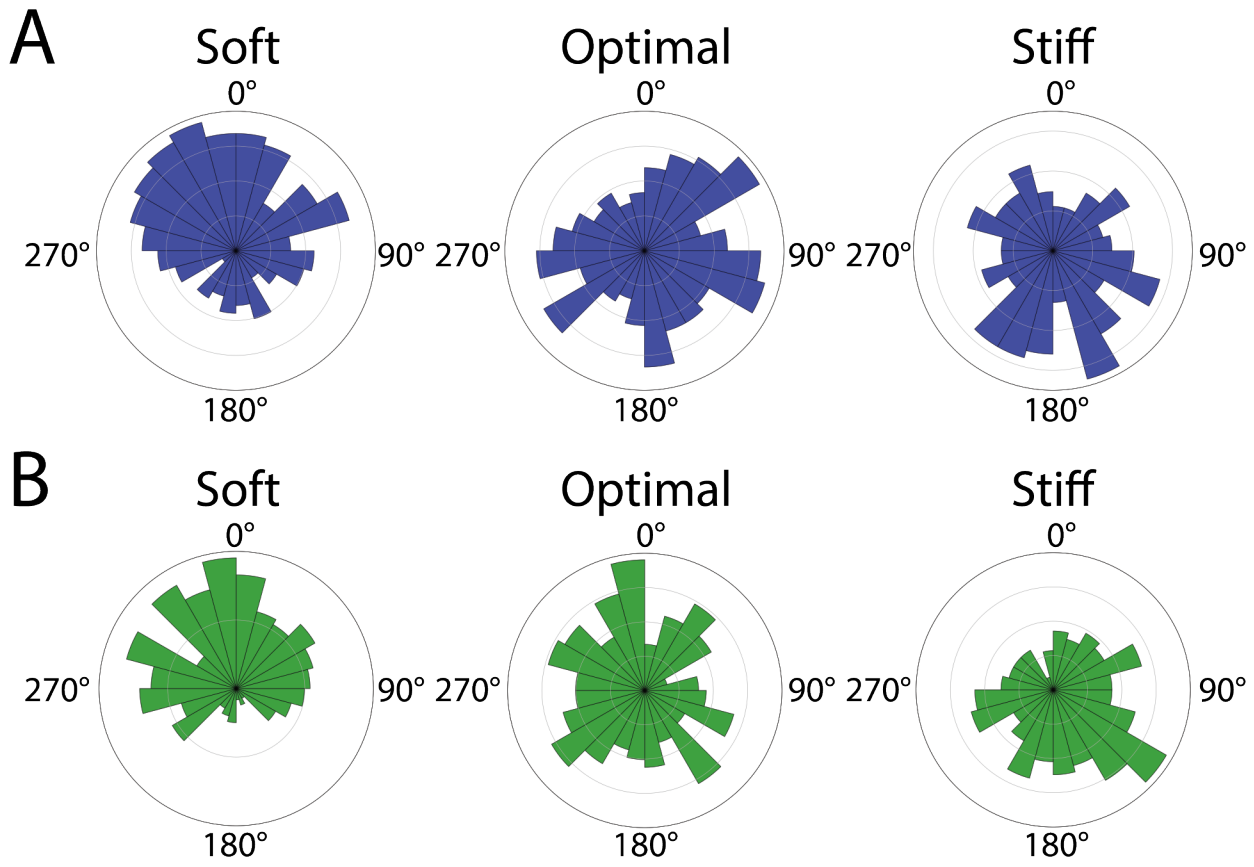

Figure 5.10: Figure A shows the angular displacement distributions for KD A2058 cells in three different regions of a 10kPa/mm substrate, and B shows the same parameter for the WT cells in the same regions.

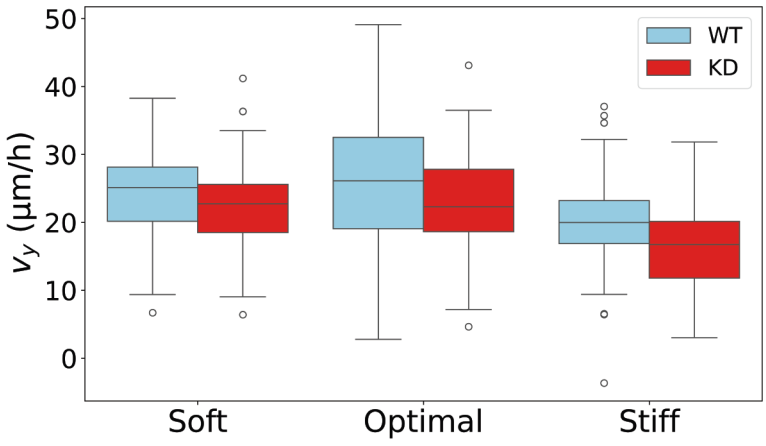

Figure 5.11: The distributions of cell velocity along the gradient, v_y for WT and KD cells in each region. Each box is the average of N = 3 KD trials.

The final comparison made between WT and KD cells was the average cell velocity component along the gradient direction v_y on the three stiffness regions. Figure 5.11 shows the data as a composite box plot of v_y, and Table 5. indicating similar behavior for the two cell types. The KD cells consistently had a lower velocity component along the gradient than the WT cells in all three regions tested, similar to the results from the homogeneous substrates. These results also show both cell populations having somewhat higher (**p $<$0.01) average velocity in the optimal stiffness region.

5.4 Discussion

In this chapter, the durotactic behavior of wild type and FMNL2 suppressed A2058 cells was studied for the first time on biomimetic gradient stiffness hydrogel substrates with a physiologically relevant range of elastic modulus. Durotactic behavior was inferred by the character of ensemble-averaged cell displacements along the gradient direction, and corroborated by several other motility metrics including the DI value, the net average angular displacement, and the orientational order parameter S.

In the first part, we found that the control cells exhibited all three forms of durotactic behavior. The cell exhibited positive durotaxis between 1-15kPa and negative durotaxis above 25kPa. Between 15-25kPa, the cells seemed to no longer respond to the gradient, and moved in a random fashion. This behavior was supported by measurements of the DI parameter along the gradient direction, DI_y, which decreased with increasing substrate modulus, as shown by Figure 5.2. These results are consistent with the results from the previous chapter showing the biphasic behavior of these cells. In particular, cells undergoing both positive and negative durotaxis are an indication that there exists a stiffness optimum for this cell type, which when reached maximizes the cells motility. This optimal value is also where the cells exert the maximum traction force with their substrate, thus inducing positive durotaxis towards the optimal value when below it, and negative durotaxis at regions of stiffness larger than the optimum. This was corroborated by the dependence on average cell velocity along the gradient direction as a function of stiffness, shown in Figure 5.6, which indicated that the maximum cell velocity occurred when the cells were in their

ideal region. After this, the velocity then decreased monotonically to a plateau value at high stiffness. These behaviors are consistent with the results from other cell lines. Duchez et all showed for multiple cancer cell lines that cell migration speed was not indicative of durotactic behavior, as the cells with the largest durotactic index had the lowest migration speeds [24]. In other study on U251 glioblastoma cells, the cells exhibited a similar biphasic response to substrate stiffness as the A2058 cells did. On either side of their optimal stiffness, they exhibited both positive and negative durotaxis [26]. Furthermore, multiple melanoma cell lines including B16F1 and B16F10 (metastatic melanoma from mice), as well as A375 (human metastatic melanoma), have all been shown to undergo negative durotaxis [33]. While these studies did not test the durotactic behavior in different regions of stiffness, they did find that the optimal substrate stiffness (e.g. 2.18kPa for the B16 cells, which is less than that found here for A2058 cells). We also investigated the impact of the local stiffness value on the negative durotaxis of these cells, as reported in Figure 5.5. We found that the value of DI_y decreased up until around 60kPa, where it reached an apparent a plateau value. This behavior indicates that the cells durotactic response is strengthened by its proximity to an optimal stiffness region, consistent with other studies of cancerous cell lines undergoing durotaxis [24].

We then investigated the impact of gradient strength on these cells in the three regions with different durotactic behavior. We utilized motility based quantities such as the durotactic index, and we also show that cell alignment can predict durotactic behavior. We found that the magnitude of the durotactic response increased with the gradient strength, before plateauing around 40kPa/mm. Figure 5.3 shows this behavior with the value of DI_y, which became increasingly positive with increasing gradient strength up until 40kPa/mm in the soft region, and which became increasingly negative with increasing gradient strength up until 40kPa/mm in the stiff region. In the optimal region, the durotactic index changed minimally between the tested gradient strengths. We then utilized an orientational order parameter approach from soft condensed matter physics as a novel metric for characterizing cell alignment along the axis of the gradient and correlating with durotactic motility of the cells. This response was accompanied by an increase in the order parameter S with gradient strength, going from $S = 0.35 \pm 0.03$ on the 3kPa/mm substrates to

S = 0.57±0.03 on the 40kPa/mm substrate. These values indicate that a larger number of cells became polarized along the direction of the gradient when the gradient strength was increased. The superdiffusive motility of the cells exhibited by their MSD traces in time also reflected this behavior, with the largest average value of the anomalous MSD exponent α being on the 40kPa/mm substrates in all of the tested regions. However, what was also interesting was that the cells still exhibited the most superdiffusive behavior in the region of optimal local stiffness, consistent with the results of chapter 4, as shown by α consistently having the largest value for the optimal stiffness region in Figure 5.8. The behavior in the soft and stuff regions was also consistent, as the soft regions exhibited a larger value of α than the stiff regions. All of these results were somewhat intuitive, as an increase in gradient strength means that the cell will be able to sense larger change in stiffness over a small length. Meaning that the cells will be able to exert tensile forces more similar to those at the optimal stiffness over a shorter distance, which resulted in the increases in DI_y that were observed.

We finally investigated the impact of suppressing FMNL2, a protein that was shown to impact A2058 motility and morphology in chapter 4. Interestingly, we found that the KD cells still exhibited durotactic behavior, but which was somewhat muted compared to the control WT cells, in a manner reminiscent to the results reported in chapter 4 for homogeneous substrates. Importantly, although values of the DI and S parameters were consistently lower than those of the WT cells, they were not low enough to indicate adurotactic motion. This suggests that FMNL2 does not significantly impact the durotactic behavior of these cells, and the noticeable changes in motility would be noticed on all substrates, regardless of a stiffness gradient. This result is similar to behaviour reported in fibroblast cells, where the affects of suppressing FMNL3 were studied [120], showing that the suppression of this formin resulted in no noticeable difference between the WT and KD cells on their gradient substrates.

5.5 Conclusion

In this chapter we investigated the impact of a gradient in substrate stiffness on the motility of A2058 melanoma cells. We studied their motion within a range of physiologically relevant moduli

utilizing a bio-mimetic protein substrate where we could create linear stiffness gradients using the diffusion of chemical crosslinkers. We found that the cells exhibited a biphasic dependence on cell motility consistent with the finding in chapter 4 of an optimal modulus for maximizing cell motility. When occupying the soft regions of a gradient substrate between 5-15kPa, the cells underwent positive durotaxis, while in areas above 25kPa, the cells underwent negative durotaxis. In the stiffness region between, cell motion was seemingly adurotactic. When introduced to substrates with different gradient strengths, we found that their durotactic motion was enhanced, as quantified by the noticeable increase in the value of DI along the gradient direction as well as the global order parameter S. The absolute stiffness of the local region also impacted cell durotaxis, as the value of DI decreased on either side of the 15-25kPa region, before reaching a plateau around 70kPa. The suppression of FMNL2 was also studied, with the results suggesting that FMNL2 does not impact A2058 cell durotaxis in a qualitatively significant way. Rather, motility for KD cells was reduced relative to WT cells, in a manner similar to the results of chapter 4, but the cells still showed more directed motion along the gradient when compared to the cells on homogeneous moduli substrates.

Chapter 6

Conclusion

The results presented in this work showcase the impact that the mechanical properties of a cell's environment can have on its behavior. We studied the impact of mechanical stiffness on melanoma cancer cells, which are known for their ability to invade and spread throughout the human body. We specifically studied A2058 melanoma cells, which are a known highly metastatic cell line. We found that A2058 melanoma cells exhibit pronounced morphological and motility based changes between substrates with different moduli. The role of the protein FMNL2, which is known to be relevant to the motility of melanoma cells, was also investigated through A2058 melanoma cells which were modified to reduce the expression of this protein, so-called protein knockdown cells (KD). The behavior of these KD cells on gradient stiffness substrates was also characterized and compared to the control A2058 cells, to characterize their durotactic behavior.

In chapter 3, we developed different methods of fabricating gradient stiffness substrates to study the durotactic response of A2058 cells. We were able to successfully create substrates with three different techniques that had linear stiffness gradients. The first method utilized photocrosslinking methods with riboflavin. The samples created had linear gradients from end to end, however, they were not thermally stable. The exact mechanisms for the noticed instability are unknown, and it would be beneficial to determine the underlying stability mechanisms, so they could be used for future cell culture studies. The other two methods, utilizing the diffusion of the crosslinkers EDC & NHS or genipin, also successfully created linear stiffness gradients over a large range of moduli. However, due to the nonlinear behavior of crosslinker diffusion, the resulting modulus

gradients of these gels were not linear throughout the entire substrate but rather only in defined regions. In future work with these substrates, it would be interesting to utilize the color changes that result from using genipin (which displays a concentration-dependent level of violet hue) as a colorimetric measure of local crosslink density to estimate the local gel modulus. Furthermore, genipin is also fluorescent, so the reaction dynamics of protein crosslinking could be studied, as well as the structure of the resultant gels using fluorescent microscopy techniques.

In chapter 4, we investigated the morphology and motility of A2058 cells on silicone and biomimetic collagen substrates. We found that these cells became progressively more elongated on stiffer substrates, and that their motility was optimized on relatively softer substrates. Specifically, on the silicone substrates, we found that this optimal modulus was between 0.2-2.0kPa, while on the collagen substrates it was close to 10kPa. On either side of these regions, net cell displacements, distance traveled, and speeds were found to decrease, showcasing the biphasic behavior of these cells around the optimal region. We also found that the suppression of FMNL2 decreased the total distance the cells would travel, as well as their time spent moving. This indicates that FMNL2 may play a role in the mechanosensing abilities of these cell lines. For future work, it would be beneficial to utilize traction force microscopy (TFM) [121]. This technique allows for the forces exerted by the cell on their substrate to be calculated by analyzing the displacement of fluorescent beads embedded in the substrate that result from the tensile forces cell protrusions apply to their local environment. This technique would allow us to directly determine which substrate conditions are trigger the cell to exert the highest traction force, a potential measure of the optimal substrate stiffness cell motility. The experiments conducted in this thesis were for dilute populations of cells on the substrates. It would be very interesting to redo these experiments for more concentrated cell populations, to look for potential collective effects on motility. Furthermore, it would be interesting to redo these experiments with other melanoma cancer cell lines, to see if they exhibit similar behavior as the A2058 cells.

In chapter 5, we investigated the behavior of these cells on gradient stiffness substrates. We found that they undergo positive durotaxis in soft regions between 1-15kPa, and negative durotaxis in regions >25kPa. In the regions between 15-25kPa, there was minimal durotactic behavior

noticed. This behavior once again highlights the biphasic behavior of these cells, with them preferentially migrating towards a stiffness optimum. We also found that their durotactic response increases with gradient strength, but declined for regions of absolute stiffness that were significantly outside of their stiffness optimum. We then investigated the impact of suppressing FMNL2, and we found that the cells still exhibited durotactic behavior, but with a reduced capacity. We also found similar behavior to that found in chapter 4, where their motility was reduced, but their durotactic abilities were not significantly impacted. These results suggest that the suppression of FMNL2 did not impact the cells ability to sense substrate stiffness, as they still underwent durotaxis. However, it still quantitatively impacted their motion, as was seen in chapter 4. In future work, utilizing TFM to see where the cells exerted the largest tensile forces would be beneficial to more accurately determine the stiffness optimum. Furthermore, it would be also interesting to explore other migratory methods of these cells. For example haptotaxis, cell migration along a gradient in substrate binding sites, would be interesting to study. Moreover, we could then combine multiple antagonistic gradients, e.g. one being a stiffness gradient and the other being a haptotactic gradient, to see which extracellular signal dominates cell behavior under different conditions.

Finally, we note that all of the work done in this thesis was based on two-dimensional in-vitro cell studies which do not reflect the true environment where melanoma cells would be found in vivo. In the future, three dimensional cell culture studies could also be performed to see how the additional dimensional degree of freedom affects their behavior. Stiffness gradients can be fabricated in 3D, and it would be interesting to study which direction the cells prefer to move if different gradient strengths were present in each direction. Furthermore, melanoma cells in real environments are most often found not as single cells, but large groups of cells generally in the form of tumours. So, studying the collective motion of isolated groups of these cells, as well as those around the periphery of a tumor, could provide crucial information about factors that lead to cancer cell metastasis.

Bibliography

[1] H. Gest. The discovery of microorganisms by Robert Hooke and Antoni van Leeuwenhoek, Fellows of The Royal Society. *Notes and Records of the Royal Society of London*, 58.2 (2004), 187–201.

[2] P. Hänggi and F. Marchesoni. Introduction: 100years of Brownian motion. *Chaos: An Interdisciplinary Journal of Nonlinear Science*, 15.2 (2005), 026101.

[3] R. Cole. Live-cell imaging. *Cell Adhesion & Migration*, 8.5 (2014), 452–459.

[4] D. J. Stephens and V. J. Allan. Light Microscopy Techniques for Live Cell Imaging. *Science*, 300.5616 (2003), 82–86.

[5] X. Trepat, Z. Chen, and K. Jacobson. Cell migration. *Compr Physiol*, 2.4 (10), 2369–92.

[6] D. J. Cohen, W. J. Nelson, and M. M. Maharbiz. Galvanotactic control of collective cell migration in epithelial monolayers. *Nature Materials*, 13.4 (2014), 409–417.

[7] J. B. Reece et al. *Campbell Biology*. 2nd Canadian Edition. Campbell, 2017.

[8] J. T. Parsons, A. R. Horwitz, and M. A. Schwartz. Cell adhesion: integrating cytoskeletal dynamics and cellular tension. *Nature Reviews Molecular Cell Biology*, 11.9 (2010), 633–643.

[9] A. A. Khalili and M. R. Ahmad. A Review of Cell Adhesion Studies for Biomedical and Biological Applications. *Int J Mol Sci*, 16.8 (2015), 18149–18184.

[10] B. S. Ludwig et al. RGD-Binding Integrins Revisited: How Recently Discovered Functions and Novel Synthetic Ligands (Re-)Shape an Ever-Evolving Field. *Cancers (Basel)*, 13.7 (2021).

[11] C. J. Dalton and C. A. Lemmon. Fibronectin: Molecular Structure, Fibrillar Structure and Mechanochemical Signaling. *Cells*, 10.9 (2021).

[12] T. Mitchison and M. Kirschner. Cytoskeletal dynamics and nerve growth. *Neuron*, 1.9 (1988), 761–772.

[13] C. E. Chan and D. J. Odde. Traction Dynamics of Filopodia on Compliant Substrates. *Science*, 322.5908 (2008), 1687–1691.

[14] Z. Xu, F. Xu, and B. Cheng. The motor-clutch model in mechanobiology and mechanomedicine. *Mechanobiology in Medicine*, 2.3 (Sept. 2024), 100067.

[15] R. J. Petrie, A. D. Doyle, and K. M. Yamada. Random versus directionally persistent cell migration. *Nature Reviews Molecular Cell Biology*, 10.8 (2009), 538–549.

[16] M. Gupta et al. Cell shape and substrate stiffness drive actin-based cell polarity. *Physical Review E*, 99.1 (2019).

[17] M. Prager-Khoutorsky et al. Fibroblast polarization is a matrix-rigidity-dependent process controlled by focal adhesion mechanosensing. *Nature Cell Biology*, 13.12 (2011), 1457–1465.

[18] M. Gupta et al. Adaptive rheology and ordering of cell cytoskeleton govern matrix rigidity sensing. *Nat Commun*, 6 (2015), 7525.

[19] M. Stoker and E. Gherardi. Regulation of cell movement: the motogenic cytokines. *Biochimica et Biophysica Acta (BBA) - Reviews on Cancer*, 1072.1 (1991), 81–102.

[20] S. SenGupta, C. A. Parent, and J. E. Bear. The principles of directed cell migration. *Nature Reviews Molecular Cell Biology*, 22.8 (2021), 529–547.

[21] C.-M. Lo et al. Cell Movement Is Guided by the Rigidity of the Substrate. *Biophysical Journal*, 79.1 (2000), 144–152.

[22] E. B. Evans et al. Schwann cell durotaxis can be guided by physiologically relevant stiffness gradients. *Biomaterials Research*, 22.1 (2018), 14.

[23] J. R. Tse and A. J. Engler. Stiffness gradients mimicking in vivo tissue variation regulate mesenchymal stem cell fate. *PLoS One*, 6.1 (2011), e15978.

[24] B. J. DuChez et al. Durotaxis by Human Cancer Cells. *Biophysical Journal*, 116.4 (2019), 670–683.

[25] M. Mathieu, A. Isomursu, and J. Ivaska. Positive and negative durotaxis – mechanisms and emerging concepts. *Journal of Cell Science*, 137.8 (2024), jcs261919.

[26] A. Isomursu et al. Directed cell migration towards softer environments. *Nat Mater*, 21.9 (2022), 1081–1090.

[27] R. Sunyer et al. Collective cell durotaxis emerges from long-range intercellular force transmission. *Science*, 353.6304 (2016), 1157–1161.

[28] M. E. Pallarès et al. Stiffness-dependent active wetting enables optimal collective cell durotaxis. *Nature Physics*, 19.2 (2023), 279–289.

[29] A. Shellard and R. Mayor. Collective durotaxis along a self-generated stiffness gradient in vivo. *Nature*, 600.7890 (2021), 690–694.

[30] B. L. Bangasser and D. J. Odde. Master Equation-Based Analysis of a Motor-Clutch Model for Cell Traction Force. *Cellular and Molecular Bioengineering*, 6.4 (2013), 449–459.

[31] B. L. Bangasser et al. Shifting the optimal stiffness for cell migration. *Nature Communications*, 8.1 (2017), 15313.

[32] D. E. Koser et al. Mechanosensing is critical for axon growth in the developing brain. *Nature Neuroscience*, 19.12 (2016), 1592–1598.

[33] Y. Huang et al. YAP Activation in Promoting Negative Durotaxis and Acral Melanoma Progression. *Cells*, 11.22 (2022).

[34] M. Zhu et al. Spatial mapping of tissue properties in vivo reveals a 3D stiffness gradient in the mouse limb bud. *Proceedings of the National Academy of Sciences*, 117.9 (Mar. 2020), 4781–4791.

[35] H. T. Nia, L. L. Munn, and R. K. Jain. Physical traits of cancer. *Science*, 370.6516 (2020), eaaz0868.

[36] I. Acerbi et al. Human breast cancer invasion and aggression correlates with ECM stiffening and immune cell infiltration. *Integrative Biology*, 7.10 (2015), 1120–1134.

[37] D. Lachowski et al. Substrate Rigidity Controls Activation and Durotaxis in Pancreatic Stellate Cells. *Scientific Reports*, 7.1 (May 2017), 2506.

[38] L. G. Vincent et al. Mesenchymal stem cell durotaxis depends on substrate stiffness gradient strength. *Biotechnology Journal*, 8.4 (Apr. 2013), 472–484.

[39] B. C. Isenberg et al. Vascular Smooth Muscle Cell Durotaxis Depends on Substrate Stiffness Gradient Strength. *Biophysical Journal*, 97.5 (2009), 1313–1322.

[40] M. Doi. *Brownian motion and thermal fluctuations*. 2013.

[41] R. Phillips et al. *Physical Biology of the Cell*. 2nd Edition. Garland Science, 2012.

[42] N. Monnier et al. Bayesian approach to MSD-based analysis of particle motion in live cells. *Biophysical journal*, 103.3 (2012), 616–626.

[43] I. D. Luzhansky et al. Anomalously diffusing and persistently migrating cells in 2D and 3D culture environments. *APL Bioengineering*, 2.2 (6), 026112.

[44] P. N. Pusey. Brownian Motion Goes Ballistic. *Science*, 332.6031 (2011), 802–803.

[45] M. Peccianti and R. Morandotti. Beyond ballistic. *Nature Physics*, 8.12 (2012), 858–859.

[46] P. Dieterich et al. Anomalous dynamics of cell migration. *Proceedings of the National Academy of Sciences*, 105.2 (2008), 459–463.

[47] B. G. Mitterwallner et al. Non-Markovian data-driven modeling of single-cell motility. *Physical Review E*, 101.3 (2020). PRE, 032408.

[48] M. Micoulaut. *Correlation Functions and Linear Response Theory*.

[49] D. E. Discher, P. Janmey, and Y.-L. Wang. Tissue Cells Feel and Respond to the Stiffness of Their Substrate. *Science*, 310.5751 (2005), 1139–1143.

[50] S. M. Salili. *Liquid Crystal Scalar and Tensorial Order Parameters in 2 and 3 Dimensions*. 2017.

[51] P. de Gennes and J. Prost. *The Physics of Liquid Crystals*. International Series of Monographs on Physics. Clarendon Press, 1993.

[52] Z. Apalla et al. Epidemiological trends in skin cancer. *Dermatol Pract Concept*, 7.2 (2017), 1–6.

[53] S. C. Wei et al. Matrix stiffness drives epithelial-mesenchymal transition and tumour metastasis through a TWIST1-G3BP2 mechanotransduction pathway. *Nat Cell Biol*, 17.5 (2015), 678–88.

[54] A. Arjonen, R. Kaukonen, and J. Ivaska. Filopodia and adhesion in cancer cell motility. *Cell Adhesion & Migration*, 5.5 (2011), 421–430.

[55] L. E. Young, E. G. Heimsath, and H. N. Higgs. Cell type–dependent mechanisms for formin-mediated assembly of filopodia. *Molecular Biology of the Cell*, 26.25 (Dec. 2015), 4646–4659.

[56] J. Lynch et al. Metastasis Suppressor microRNA-335 Targets the Formin Family of Actin Nucleators. *PLoS ONE*, 8.11 (2013), e78428.

[57] S. Kühn et al. The structure of FMNL2–Cdc42 yields insights into the mechanism of lamellipodia and filopodia formation. *Nature Communications*, 6 (2015), 7088.

[58] V. Dimchev et al. Induced Arp2/3 Complex Depletion Increases FMNL2/3 Formin Expression and Filopodia Formation. *Frontiers in Cell and Developmental Biology*, 9 (2021).

[59] S. Fox et al. Cooperative assembly of filopodia by the formin FMNL2 and I-BAR domain protein IRTKS. *Journal of Biological Chemistry*, 298.11 (2022), 102512.

[60] C. Péladeau et al. A specific FMNL2 isoform is up-regulated in invasive cells. *BMC Cell Biology*, 17.1 (2016).

[61] K. Grikscheit et al. Junctional actin assembly is mediated by Formin-like 2 downstream of Rac1. *Journal of Cell Biology*, 209.3 (2015), 367–376.

[62] Y. Wang et al. Formin-like 2 Promotes β1-Integrin Trafficking and Invasive Motility Downstream of PKCα. *Developmental Cell*, 34.4 (Aug. 2015), 475–483.

[63] M. Gardberg et al. FMNL2/FMNL3 formins are linked with oncogenic pathways and predict melanoma outcome. *The Journal of Pathology: Clinical Research*, 2.1 (2016), 41–52.

[64] F. Kage et al. FMNL formins boost lamellipodial force generation. *Nature Communications*, 8 (2017), 14832.

[65] F. Ullah et al. Classification, processing and application of hydrogels: A review. *Materials Science and Engineering: C*, 57 (Dec. 2015), 414–433.

[66] E. M. Ahmed. Hydrogel: Preparation, characterization, and applications: A review. *Journal of Advanced Research*, 6.2 (2015), 105–121.

[67] S. S. Wong and L.-J. C. Wong. Chemical crosslinking and the stabilization of proteins and enzymes. *Enzyme and Microbial Technology*, 14.11 (Nov. 1992), 866–874.

[68] M. D. Shoulders and R. T. Raines. Collagen Structure and Stability. *Annual Review of Biochemistry*, 78.Volume 78, 2009 (2009). Journal ArticleAnnual Review of Biochemistry 2009;78(1):929-958, 929–958.

[69] M. I. A. Rodríguez, L. G. R. Barroso, and M. L. Sánchez. Collagen: A review on its sources and potential cosmetic applications. *Journal of Cosmetic Dermatology*, 17.1 (2018), 20–26.

[70] R. Naomi, P. M. Ridzuan, and H. Bahari. *Current Insights into Collagen Type I*. 2021.

[71] K. Adamiak and A. Sionkowska. Current methods of collagen cross-linking: Review. *International Journal of Biological Macromolecules*, 161 (2020), 550–560.

[72] K. Merrett et al. Enhanced Collagen-like Protein for Facile Biomaterial Fabrication. *ACS Biomaterials Science & Engineering*, 7.4 (2021), 1414–1427.

[73] Thermofisher. Image.

[74] C. Yang. Enhanced physicochemical properties of collagen by using EDC/NHS-crosslinking. *Bulletin of Materials Science*, 35.5 (Oct. 2012), 913–918.

[75] J. Hua et al. Preparation and properties of EDC/NHS mediated crosslinking poly (gamma-glutamic acid)/epsilon-polylysine hydrogels. *Materials Science and Engineering: C*, 61 (2016), 879–892.

[76] Y. Yu et al. Genipin-cross-linked hydrogels based on biomaterials for drug delivery: a review. *Biomaterials Science*, 9.5 (2021).

[77] W. Song et al. The Short-Term Safety Evaluation of Corneal Crosslinking Agent-Genipin. *Ophthalmic Research*, 62.3 (2019), 141–149.

[78] J. P. Beier et al. Collagen matrices from sponge to nano: new perspectives for tissue engineering of skeletal muscle. *BMC Biotechnology*, 9 (2009), 34.

[79] N. Siddiqui, K. Pramanik, and E. Jabbari. Osteogenic differentiation of human mesenchymal stem cells in freeze-gelled chitosan/nano β-tricalcium phosphate porous scaffolds crosslinked with genipin. *Materials Science and Engineering: C*, 54 (2015), 76–83.

[80] S.-M. Lien, W.-T. Li, and T.-J. Huang. Genipin-crosslinked gelatin scaffolds for articular cartilage tissue engineering with a novel crosslinking method. *Materials Science and Engineering: C*, 28.1 (2008), 36–43.

[81] Y.-J. Hwang et al. Effect of genipin crosslinking on the optical spectral properties and structures of collagen hydrogels. *ACS applied materials & interfaces*, 3.7 (2011), 2579–2584.

[82] P. Sánchez, J. L. Pedraz, and G. Orive. Biologically active and biomimetic dual gelatin scaffolds for tissue engineering. *International Journal of Biological Macromolecules*, 98 (2017), 486–494.

[83] B. P. Partlow et al. Highly Tunable Elastomeric Silk Biomaterials. *Advanced Functional Materials*, 24.29 (2014), 4615–4624.

[84] C. Liu et al. Photochemistry of bioinspired dityrosine crosslinking. *Journal of Materials Science & Technology*, 63 (2021), 182–191.

[85] D. A. Fancy and T. Kodadek. Chemistry for the analysis of protein–protein interactions: Rapid and efficient cross-linking triggered by long wavelength light. *Proceedings of the National Academy of Sciences*, 96.11 (1999), 6020–6024.

[86] A. V. Vashi et al. Stabilization of collagen tissues by photocrosslinking. *Journal of Biomedical Materials Research Part A*, 100A.9 (Sept. 2012), 2239–2243.

[87] D. Cherfan et al. Collagen cross-linking using rose bengal and green light to increase corneal stiffness. *Invest Ophthalmol Vis Sci*, 54.5 (2013), 3426–3433.

[88] B. P. Partlow et al. Dityrosine Cross-Linking in Designing Biomaterials. *ACS Biomaterials Science & Engineering*, 2.12 (2016), 2108–2121.

[89] R. Huang, E. Choe, and D. B. Min. Kinetics for Singlet Oxygen Formation by Riboflavin Photosensitization and the Reaction between Riboflavin and Singlet Oxygen. *Journal of Food Science*, 69.9 (2004), C726–C732.

[90] S. Piluso et al. Rapid and cytocompatible cell-laden silk hydrogel formation via riboflavin-mediated crosslinking. *Journal of Materials Chemistry B*, 8.41 (2020), 9566–9575.

[91] J. K. Placone et al. Development and Characterization of a 3D Printed, Keratin-Based Hydrogel. *Annals of Biomedical Engineering*, 45.1 (2017), 237–248.

[92] P. Oswald. *Rheophysics: The Deformation and Flow of Matter*. Cambridge University Press, 2014.

[93] H. T. Banks, S. Hu, and Z. R. Kenz. A Brief Review of Elasticity and Viscoelasticity for Solids. *Advances in Applied Mathematics and Mechanics*, 3.1 (2011), 1–51.

[94] R. S. Lakes. Viscoelastic measurement techniques. *Review of Scientific Instruments*, 75.4 (July 2004), 797–810.

[95] D. J. Müller et al. Atomic Force Microscopy-Based Force Spectroscopy and Multiparametric Imaging of Biomolecular and Cellular Systems. *Chemical Reviews*, 121.19 (2021), 11701–11725.

[96] S. V. Kontomaris and A. Malamou. Hertz model or Oliver & Pharr analysis? Tutorial regarding AFM nanoindentation experiments on biological samples. *Materials Research Express*, 7.3 (2020), 033001.

[97] A. Ikai. A Review on: Atomic Force Microscopy Applied to Nano-mechanics of the Cell. Nano/Micro Biotechnology. Berlin, Heidelberg: Springer Berlin Heidelberg, 2010, 47–61.

[98] A. E. Pelling et al. Approaches for investigating mechanobiological dynamics in living cells with fluorescence and atomic force microscopies. *Modern research and educational topics on microscopy*, 3 (2007), 3–10.

[99] M. Stolz et al. Dynamic elastic modulus of porcine articular cartilage determined at two different levels of tissue organization by indentation-type atomic force microscopy. *Biophys J*, 86.5 (5), 3269–83.

[100] F. Rico et al. Probing mechanical properties of living cells by atomic force microscopy with blunted pyramidal cantilever tips. *Physical Review E*, 72.2 (2005), 021914.

[101] I. N. Sneddon. The relation between load and penetration in the axisymmetric boussinesq problem for a punch of arbitrary profile. *International Journal of Engineering Science*, 3.1 (1965), 47–57.

[102] N. W. Tschoegl, W. G. Knauss, and I. Emri. Poisson's Ratio in Linear Viscoelasticity – A Critical Review. *Mechanics of Time-Dependent Materials*, 6.1 (Mar. 2002), 3–51.

[103] U. Chippada, B. Yurke, and N. A. Langrana. Simultaneous determination of Young's modulus, shear modulus, and Poisson's ratio of soft hydrogels. *Journal of Materials Research*, 25.3 (2010), 545–555.

[104] G. Sennakesavan et al. Acrylic acid/acrylamide based hydrogels and its properties - A review. *Polymer Degradation and Stability*, 180 (2020), 109308.

[105] P. Kiviranta et al. Collagen network primarily controls Poisson's ratio of bovine articular cartilage in compression. *Journal of Orthopaedic Research*, 24.4 (2006), 690–699.

[106] A. P. Janmey, A. D. Fletcher, and A. C. Reinhart-King. Stiffness Sensing by Cells. *Physiological Reviews*, 100.2 (2020), 695–724.

[107] A. J. Engler et al. Surface probe measurements of the elasticity of sectioned tissue, thin gels and polyelectrolyte multilayer films: Correlations between substrate stiffness and cell adhesion. *Surface Science*, 570.1–2 (2004), 142–154.

[108] S. V. Plotnikov et al. Force Fluctuations within Focal Adhesions Mediate ECM-Rigidity Sensing to Guide Directed Cell Migration. *Cell*, 151.7 (2012), 1513–1527.

[109] B. Geiger, J. P. Spatz, and A. D. Bershadsky. Environmental sensing through focal adhesions. *Nature Reviews Molecular Cell Biology*, 10.1 (2009), 21–33.

[110] K. Burridge and C. Guilluy. Focal adhesions, stress fibers and mechanical tension. *Experimental Cell Research*, 343.1 (2016), 14–20.

[111] G. Bradski. The OpenCV Library. *Dr. Dobb's Journal of Software Tools* (2000).

[112] A. Shellard and R. Mayor. Durotaxis: The Hard Path from In Vitro to In Vivo. *Developmental Cell*, 56.2 (2021), 227–239.

[113] C. Ji and Y. Huang. Durotaxis and negative durotaxis: where should cells go? *Communications Biology*, 6.1 (Nov. 2023), 1169.

[114] B. Yeoman et al. Adhesion strength and contractility enable metastatic cells to become adurotactic. *Cell Reports*, 34.10 (Mar. 2021), 108816.

[115] P. Sáez and C. Venturini. Positive, negative and controlled durotaxis. *Soft Matter*, 19.16 (2023), 2993–3001.

[116] J. Block et al. FMNL2 drives actin-based protrusion and migration downstream of Cdc42. *Current Biology*, 22.11 (2012), 1005–1012.

[117] E. S. Harris et al. Assembly of filopodia by the formin FRL2 (FMNL3). *Cytoskeleton*, 67.12 (Dec. 2010), 755–772.

[118] K. Pfisterer et al. FMNL2 regulates dynamics of fascin in filopodia. *Journal of Cell Biology*, 219.5 (Apr. 2020), e201906111.

[119] X. L. Ren et al. Cortactin recruits FMNL2 to promote actin polymerization and endosome motility in invadopodia formation. *Cancer Letters*, 419 (Apr. 2018), 245–256.

[120] R. M. Hakeem et al. A Photopolymerized Hydrogel System with Dual Stiffness Gradients Reveals Distinct Actomyosin-Based Mechano-Responses in Fibroblast Durotaxis. *ACS Nano*, 17.1 (2023), 197–211.

[121] Y. Huang et al. Traction force microscopy with optimized regularization and automated Bayesian parameter selection for comparing cells. *Scientific Reports*, 9.1 (Jan. 2019), 539.

Appendix A

A.1 Probability Distribution of a Random Walker in d Dimensions

In a random walk process, such as those found in Brownian systems, the displacement vector $\vec{R}$ after a single step can be decomposed into its components along each of the d dimensions. Let's denote these components as $R_1, R_2, \ldots, R_d$, where R_i is the displacement along the i-th dimension.

Assume that the length of each step ℓ is constant, but the direction of the step is uniformly distributed across all possible directions in the d-dimensional space. In this case, the probability distribution for the direction of the step is symmetric, meaning that each component R_i has an equal chance of being positive or negative. Given this symmetry, the expected value of the displacement in each direction is zero:

$$\langle R_i \rangle = 0 \tag{A.1}$$

However, the mean squared displacement (MSD) for each component R_i is non-zero. Since the random walk is isotropic (the same in all directions), the step length ℓ is related to the sum of the squares of the components as follows:

$$\ell^2 = \sum_{i=1}^{d} R_i^2 \tag{A.2}$$

Taking the expectation of both sides, and recognizing that each R_i^2 is identically distributed, we have:

$$\ell^2 = \sum_{i=1}^{d} \langle R_i^2 \rangle \tag{A.3}$$

Since the MSD is the same for each dimension, $\langle R_1^2 \rangle = \langle R_2^2 \rangle = \cdots = \langle R_d^2 \rangle$, we can simplify this to:

$$\langle R_i^2 \rangle = \frac{\ell^2}{d} \tag{A.4}$$

This result shows that the step length ℓ is evenly distributed among the d dimensions in terms of the mean squared displacement. The more dimensions there are, the smaller the contribution of each dimension to the overall step length.

After N steps, the total displacement vector $\vec{R}$ in d dimensions is given by the sum of the individual displacements:

$$\vec{R} = \sum_{j=1}^{N} \vec{R}_j \tag{A.5}$$

Since each step is independent, the mean squared displacement in d dimensions can be written as:

$$\langle \|\vec{R}\|^2 \rangle = \sum_{i=1}^{d} \langle R_i^2 \rangle = N \langle \|\vec{R}\|^2 \rangle = N\ell^2 \tag{A.6}$$

Substituting the expression for $\langle \|\vec{R}\|^2 \rangle$, we obtain:

$$\langle \|\vec{R}\|^2 \rangle = N \frac{\ell^2}{d} \times d = N\ell^2 \tag{A.7}$$

To relate this to time, we note that if the random walk occurs over a time interval t, with N steps taken during this time, then N can be expressed as $N = \frac{t}{\Delta t}$, where Δt is the time interval per step. Therefore, the total mean squared displacement over time t becomes:

$$\langle \|\vec{R}\|^2 \rangle = \frac{t}{\Delta t} \ell^2 \tag{A.8}$$

We define the diffusion coefficient D as:

$$D = \frac{\ell^2}{2d\Delta t} \tag{A.9}$$

Substituting this into the expression for the mean squared displacement gives:

$$\langle \|\vec{R}\|^2 \rangle = 2dDt \tag{A.10}$$

The variance σ_i^2 for each component R_i of the displacement vector $\vec{R}$ can now be derived. Since R_i is normally distributed, we know that:

$$\sigma_i^2 = \langle R_i^2 \rangle - \langle R_i \rangle^2 \tag{A.11}$$

Given that $\langle R_i \rangle = 0$, the variance simplifies to:

$$\sigma_i^2 = \langle R_i^2 \rangle = 2Dt \tag{A.12}$$

Now, instead of using the central limit theorem, we can derive the probability distribution $P(\vec{R}, t)$ for the displacement vector $\vec{R}$ over a time interval t by solving the diffusion equation in d dimensions.

The diffusion equation in d dimensions is given by:

$$\frac{\partial P(\vec{R}, t)}{\partial t} = D\nabla^2 P(\vec{R}, t) \tag{A.13}$$

We apply the Fourier transform to both sides of the diffusion equation. The Fourier transform of $P(\vec{R}, t)$ is defined as:

$$\hat{P}(\vec{k}, t) = \int_{-\infty}^{\infty} \cdots \int_{-\infty}^{\infty} P(\vec{R}, t) e^{-i\vec{k}\cdot\vec{R}} \, d^d R \tag{A.14}$$

where: - $\vec{k} = (k_1, k_2, \ldots, k_d)$ is the Fourier space vector. - $\vec{R} = (R_1, R_2, \ldots, R_d)$ is the position vector in d dimensions.

Taking the d-dimensional Fourier transform of the diffusion equation:

$$\frac{\partial \hat{P}(\vec{k}, t)}{\partial t} = -D \left(k_1^2 + k_2^2 + \cdots + k_d^2 \right) \hat{P}(\vec{k}, t) \tag{A.15}$$

This simplifies to:

$$\frac{\partial \hat{P}(\vec{k},t)}{\partial t} = -D|\vec{k}|^2 \hat{P}(\vec{k},t) \tag{A.16}$$

where $|\vec{k}|^2 = k_1^2 + k_2^2 + \cdots + k_d^2$ is the squared magnitude of the wave vector $\vec{k}$.

This equation is a first-order linear ordinary differential equation in time. The general solution is:

$$\hat{P}(\vec{k},t) = \hat{P}(\vec{k},0) \exp\left(-D|\vec{k}|^2 t\right) \tag{A.17}$$

where $\hat{P}(\vec{k},0)$ is the Fourier transform of the initial condition $P(\vec{R},0)$.

Assume the initial condition is a delta function, meaning the particle starts at the origin:

$$P(\vec{R},0) = \delta(\vec{R}) = \delta(R_1)\delta(R_2)\cdots\delta(R_d) \tag{A.18}$$

The Fourier transform of a delta function is 1, so:

$$\hat{P}(\vec{k},0) = 1 \tag{A.19}$$

Thus, the solution in Fourier space becomes:

$$\hat{P}(\vec{k},t) = \exp\left(-D|\vec{k}|^2 t\right) \tag{A.20}$$

To find the solution in real space, we take the inverse Fourier transform:

$$P(\vec{R},t) = \frac{1}{(2\pi)^d} \int_{-\infty}^{\infty} \cdots \int_{-\infty}^{\infty} \hat{P}(\vec{k},t) e^{i\vec{k}\cdot\vec{R}}\, d^d k \tag{A.21}$$

Substituting $\hat{P}(\vec{k},t)$:

$$P(\vec{R},t) = \frac{1}{(2\pi)^d} \int_{-\infty}^{\infty} \cdots \int_{-\infty}^{\infty} \exp\left(-D|\vec{k}|^2 t + i\vec{k}\cdot\vec{R}\right)\, d^d k \tag{A.22}$$

The integrals over each k_i can be solved independently. For each component k_i, the integral is of the form:

$$\int_{-\infty}^{\infty} \exp\left(-Dk_i^2 t + ik_i R_i\right)\, dk_i = \sqrt{\frac{\pi}{Dt}} \exp\left(-\frac{R_i^2}{4Dt}\right) \tag{A.23}$$

Therefore, the solution in real space is:

$$P(\vec{R}, t) = \frac{1}{(2\pi)^d} \prod_{i=1}^{d} \sqrt{\frac{\pi}{Dt}} \exp\left(-\frac{R_i^2}{4Dt}\right) \tag{A.24}$$

Multiplying the factors together:

$$P(\vec{R}, t) = \left(\frac{1}{\sqrt{4\pi Dt}}\right)^d \exp\left(-\frac{|\vec{R}|^2}{4Dt}\right) \tag{A.25}$$

where $|\vec{R}|^2 = R_1^2 + R_2^2 + \cdots + R_d^2$ is the squared magnitude of the displacement vector $\vec{R}$. The final probability distribution $P(\vec{R}, t)$ in d dimensions is:

$$P(\vec{R}, t) = \frac{1}{(4\pi Dt)^{d/2}} \exp\left(-\frac{|\vec{R}|^2}{4Dt}\right) \tag{A.26}$$

A.2 MSD Derivation in d Dimensions

The Gaussian form of the probability distribution for random walk processes in d dimensions is given by:

$$P(\vec{R}, t) = \frac{1}{(4\pi Dt)^{d/2}} \exp\left(-\frac{|\vec{R}|^2}{4Dt}\right). \tag{A.27}$$

The MSD for purely diffusive motion can be derived from the second moment of this probability distribution as follows. The MSD, denoted by $\langle R^2(t)\rangle$, is defined as:

$$\langle R^2(t)\rangle = \int_{\mathbb{R}^d} R^2 P(\vec{R}, t)\, d^d R \tag{A.28}$$

where $d^d R$ is the differential volume element in d dimensions. To simplify the integration, we convert to spherical coordinates in d dimensions, where R is the radial coordinate. The volume

element in spherical coordinates is:

$$d^d R = R^{d-1}\, dR\, d\Omega_d \tag{A.29}$$

where $d\Omega_d$ represents the differential solid angle in d dimensions. The MSD can now be expressed as:

$$\langle R^2(t)\rangle = \int_0^\infty R^2 \cdot P(\vec{R}, t) \cdot R^{d-1}\, dR \int d\Omega_d \tag{A.30}$$

The integral over the angular part $\int d\Omega_d$ is the total solid angle in d dimensions, denoted as Ω_d. For a d-dimensional space:

$$\Omega_d = \frac{2\pi^{d/2}}{\Gamma(d/2)} \tag{A.31}$$

Thus, the MSD becomes:

$$\langle R^2(t)\rangle = \frac{\Omega_d}{(4\pi Dt)^{d/2}} \int_0^\infty R^{d+1} \exp\left(-\frac{R^2}{4Dt}\right) dR \tag{A.32}$$

Introducing the substitution $u = \frac{R^2}{4Dt}$ with $du = \frac{R}{2Dt} dR$, the integral becomes:

$$\langle R^2(t)\rangle = \frac{\Omega_d}{(4\pi Dt)^{d/2}} \cdot (4Dt)^{(d/2)+1} \int_0^\infty u^{(d/2)} \exp(-u)\, du \tag{A.33}$$

Simplifying and evaluating the integral, we find:

$$\langle R^2(t)\rangle = \frac{\Omega_d \cdot 4Dt}{(4\pi Dt)^{d/2}} \cdot \Gamma\left(\frac{d}{2} + 1\right) \tag{A.34}$$

where $\Gamma\left(\frac{d}{2} + 1\right)$ is the Gamma function. Using the relationship $\Gamma(z+1) = z\Gamma(z)$, the MSD simplifies to:

$$\langle R^2(t)\rangle = \frac{4Dt \cdot \Gamma\left(\frac{d}{2} + 1\right)}{(4\pi Dt)^{d/2-1} \cdot \pi^{d/2}} \tag{A.35}$$

$$\langle R^2(t)\rangle = 2dDt \tag{A.36}$$

where Ω_d and other terms cancel out, leaving the result dependent on the number of dimensions. Thus, the mean squared displacement (MSD) for cells moving diffusively in d dimensions is:

$$\Delta r^2_{\text{MSD}}(\tau) = 2dD\tau \tag{A.37}$$

where τ is the lag time, D is the diffusion constant, and d is the number of spatial dimensions. For two dimensions ($d = 2$), this simplifies to:

$$\Delta r^2_{\text{MSD}}(\tau) = 4D\tau \tag{A.38}$$

which is the result obtained in the main text.

A.3 Biased Diffusion Derivation in 1D

Consider a particle moving in one dimension under the influence of a bias [41]. The particle can jump to the right with probability p_+ and to the left with probability p_- in each time step Δt. The particle moves a distance ℓ in each step. For a single step, the mean displacement $\langle \Delta x \rangle$ is:

$$\langle \Delta x \rangle = \ell \cdot p_+ \Delta t + (-\ell) \cdot p_- \Delta t = \ell(p_+ - p_-)\Delta t \tag{A.39}$$

The simplified variance of the displacement $\text{var}(\Delta x)$ is:

$$\text{var}(\Delta x) = \ell^2 \cdot p_+ \Delta t + \ell^2 \cdot p_- \Delta t - \langle \Delta x \rangle^2 \tag{A.40}$$

Since $\langle \Delta x \rangle^2$ is of order $(\Delta t)^2$, this means that it can be neglected, so:

$$\text{var}(\Delta x) = \ell^2(p_+ + p_-)\Delta t \tag{A.41}$$

For a total time t, where the particle takes $N = \frac{t}{\Delta t}$ steps, the total mean displacement $\langle x(t) \rangle$ and variance $\text{var}(x(t))$ are:

$$\langle x(t) \rangle = N \langle \Delta x \rangle = \ell(p_+ - p_-)t \tag{A.42}$$

$$\text{var}(x(t)) = N\text{var}(\Delta x) = \ell^2(p_+ + p_-)t \tag{A.43}$$

Thus, the drift velocity v and diffusion coefficient D are given by:

$$v = \frac{\langle x(t) \rangle}{t} = \ell(p_+ - p_-) \tag{A.44}$$

$$D = \frac{\text{var}(x(t))}{2t} = \frac{\ell^2(p_+ + p_-)}{2} \tag{A.45}$$

The probability of finding the particle at position x at time $t + \Delta t$ is:

$$P(x, t + \Delta t) = [1 - (p_+ + p_-)\Delta t]P(x, t) + p_+\Delta t \cdot P(x - \ell, t) + p_-\Delta t \cdot P(x + \ell, t) \tag{A.46}$$

Expanding $P(x, t + \Delta t)$, $P(x - \ell, t)$, and $P(x + \ell, t)$ using a Taylor series gives:

$$P(x, t + \Delta t) = P(x, t) + \frac{\partial P(x, t)}{\partial t}\Delta t + \ldots \tag{A.47}$$

$$P(x \pm \ell, t) = P(x, t) \pm \ell\frac{\partial P(x, t)}{\partial x} + \frac{\ell^2}{2}\frac{\partial^2 P(x, t)}{\partial x^2} + \ldots \tag{A.48}$$

Substituting these expansions into the probability equation and equating the terms linear in Δt, we obtain the diffusion equation:

$$\frac{\partial P(x, t)}{\partial t} = -v\frac{\partial P(x, t)}{\partial x} + D\frac{\partial^2 P(x, t)}{\partial x^2} \tag{A.49}$$

Now, let's solve this partial differential equation using the Fourier transform method. The Fourier transform of the probability density $P(x, t)$ is defined as:

$$\hat{P}(k, t) = \int_{-\infty}^{\infty} P(x, t)e^{-ikx}\, dx \tag{A.50}$$

where k is the wave number. Taking the Fourier transform of both sides of the diffusion equation:

$$\frac{\partial \hat{P}(k, t)}{\partial t} = -ikv\hat{P}(k, t) - Dk^2\hat{P}(k, t) \tag{A.51}$$

This is a first-order linear ordinary differential equation in t, which can be solved using the method of integrating factors. The solution is:

$$\hat{P}(k,t) = \hat{P}(k,0) \exp\left(-ikvt - Dk^2 t\right) \tag{A.52}$$

To find $\hat{P}(k,0)$, we use the initial condition $P(x,0) = \delta(x)$, which gives:

$$\hat{P}(k,0) = \int_{-\infty}^{\infty} \delta(x) e^{-ikx}\, dx = 1 \tag{A.53}$$

Thus, the solution in Fourier space is:

$$\hat{P}(k,t) = \exp\left(-ikvt - Dk^2 t\right) \tag{A.54}$$

Taking the inverse Fourier transform to find $P(x,t)$:

$$P(x,t) = \frac{1}{2\pi} \int_{-\infty}^{\infty} \hat{P}(k,t) e^{ikx}\, dk \tag{A.55}$$

Substituting $\hat{P}(k,t)$ into the integral:

$$P(x,t) = \frac{1}{2\pi} \int_{-\infty}^{\infty} \exp\left(-ikvt - Dk^2 t + ikx\right)\, dk \tag{A.56}$$

This integral can be simplified as follows. Combine the terms in the exponent:

$$P(x,t) = \frac{1}{2\pi} \int_{-\infty}^{\infty} \exp\left(-Dk^2 t + ik(x - vt)\right)\, dk \tag{A.57}$$

The integral can be recognized as a standard Gaussian integral in k:

$$\int_{-\infty}^{\infty} \exp\left(-\alpha k^2 + \beta k\right)\, dk = \sqrt{\frac{\pi}{\alpha}} \exp\left(\frac{\beta^2}{4\alpha}\right) \tag{A.58}$$

where $\alpha = Dt$ and $\beta = i(x - vt)$. Applying this to our equation:

$$P(x,t) = \frac{1}{2\pi}\sqrt{\frac{\pi}{Dt}}\exp\left(-\frac{(x-vt)^2}{4Dt}\right) \tag{A.59}$$

Simplifying further:

$$P(x,t) = \frac{1}{\sqrt{4\pi Dt}}\exp\left(-\frac{(x-vt)^2}{4Dt}\right) \tag{A.60}$$

This is the Gaussian solution for the probability distribution. To find the mean squared displacement $\langle x^2(t)\rangle$, we compute the second moment of the distribution:

$$\langle x^2(t)\rangle = \int_{-\infty}^{\infty} x^2 P(x,t)\,dx \tag{A.61}$$

Substituting the Gaussian solution:

$$\langle x^2(t)\rangle = \frac{1}{\sqrt{4\pi Dt}}\int_{-\infty}^{\infty} x^2 \exp\left(-\frac{(x-vt)^2}{4Dt}\right) dx \tag{A.62}$$

This can be computed by changing the variable $u = \frac{x-vt}{\sqrt{4Dt}}$, leading to:

$$\langle x^2(t)\rangle = (vt)^2 + 2Dt \tag{A.63}$$

where $v = \ell(p_+ - p_-)$ is the drift velocity, and $D = \frac{\ell^2(p_+ + p_-)}{2}$ is the diffusion coefficient.

Appendix B

The following two plots (Figure B.1 and Figure B.2), are two plots following the same analysis shown in Figure 5.1, except they are in 20kPa and 40kPa regions respectively.

In Figure B.1, the analysis was performed in a 20kPa region, which falls within the defined optimal region found in Chapter 5. As such, the behavior of the cells in this region was seemingly adurotactic, with both displacement components (Λ_x and Λ_y) being close to 0. Furthermore, the angular displacement plots were also well distributed from 0 to 360 degrees. Whereas in Figure B.2 (corresponding to the 40kPa region), there was directed behavior that was noticed. The displacement along the gradient (Λ_y) shifted to a negative value, and the angular displacement on the gradient substrate showed a peak around 180 degrees. This is the opposite of what was noticed in Figure 5.1, as this indicates that the cells moved from the stiff to soft regions of the hydrogel, or underwent negative durotaxis.

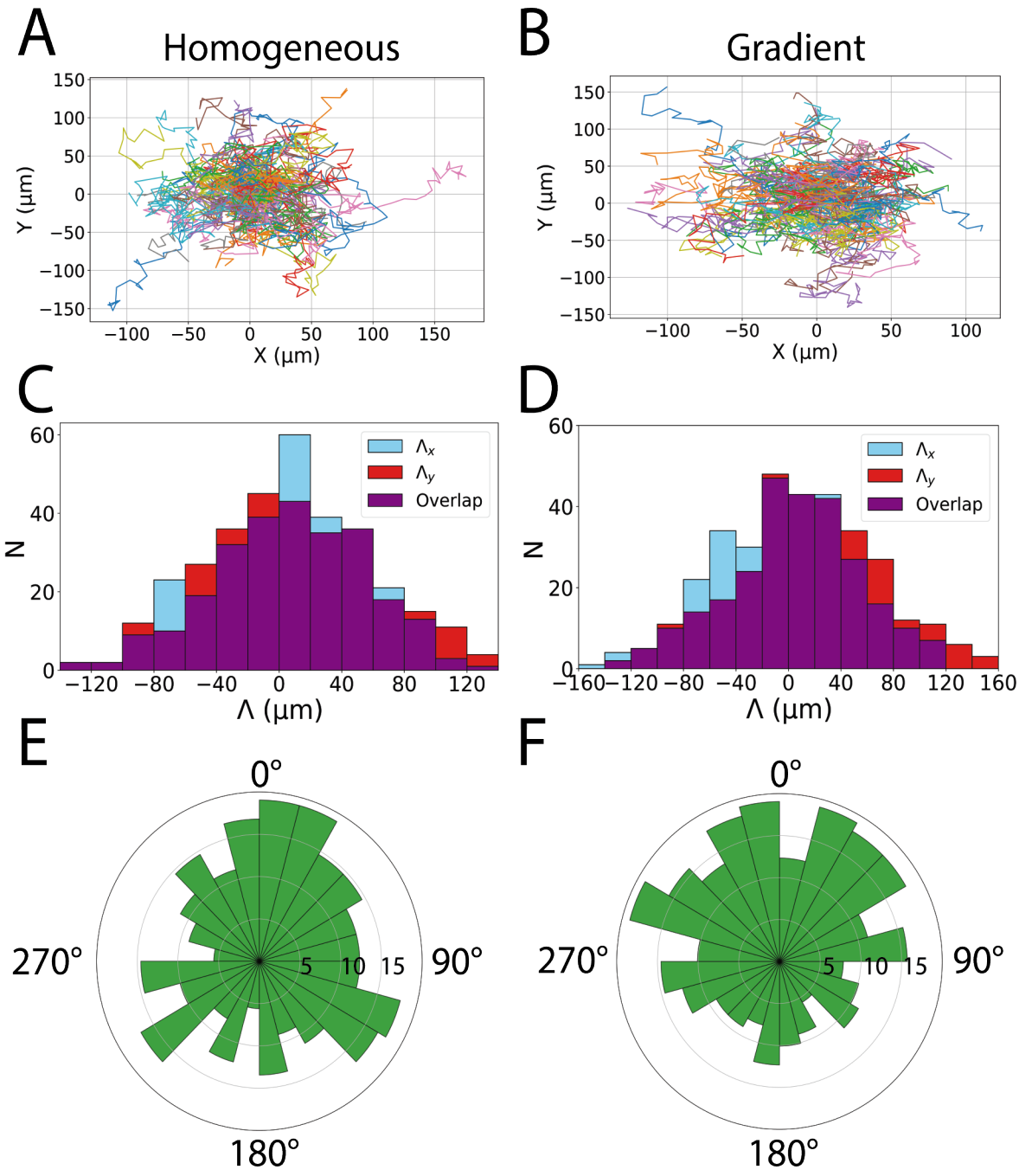

Figure B.1: A comparison between cell motion on a homogeneous 20kPa substrate and a gradient substrate in a 20kPa region with a gradient strength of 2.5kPa/mm. Figures A and B compare the cell tracks of cells on homogeneous (A) and gradient (B) substrates. Figure C and D compares the displacement along x (Λ_x) and y (Λ_y). Figures E and F compare the angular displacement of cells on both substrates.

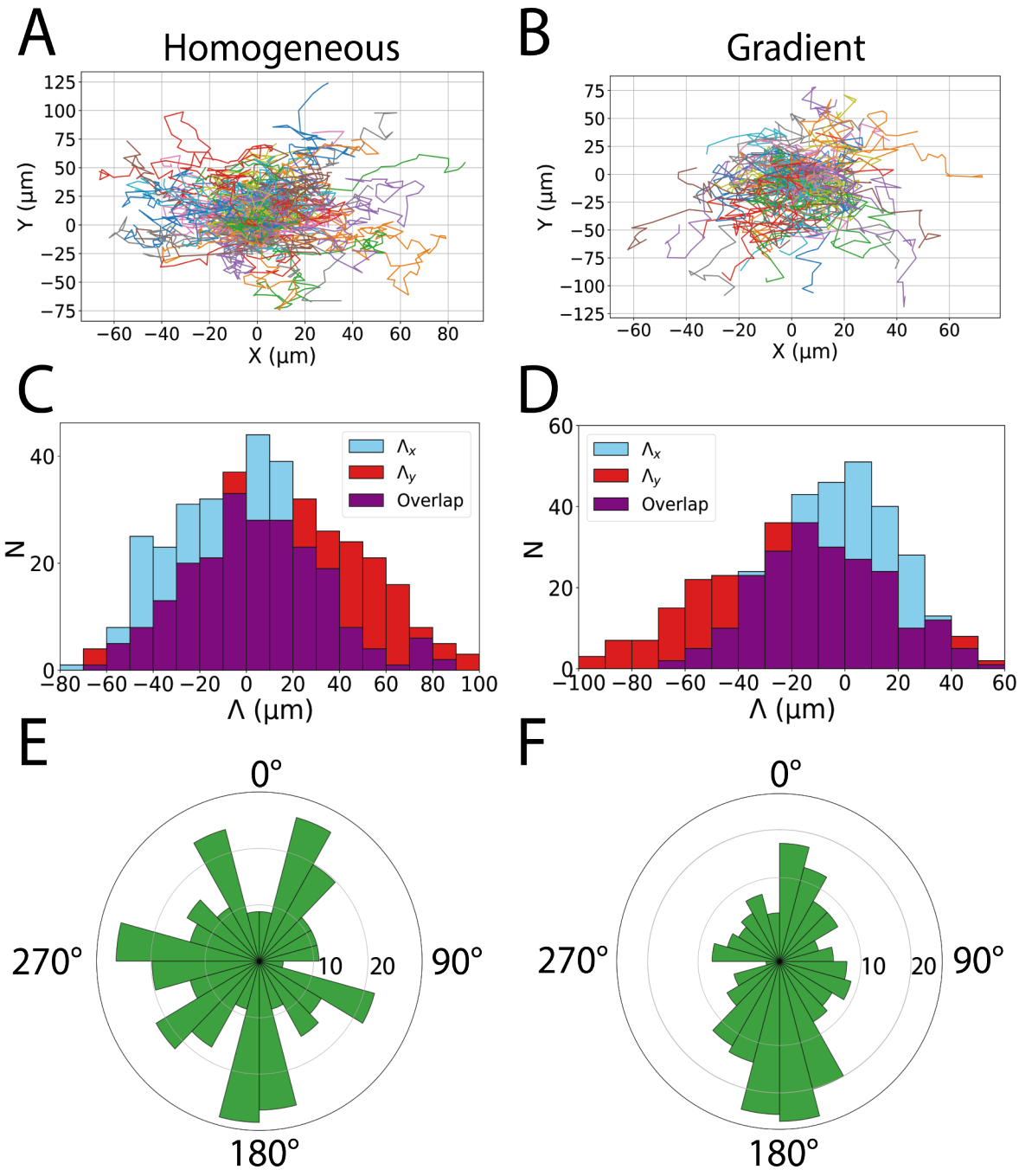

Figure B.2: A comparison between cell motion on a homogeneous 40kPa substrate and a gradient substrate in a 40kPa region with a gradient strength of 2.5kPa/mm. Figures A and B compare the cell tracks of cells on homogeneous (A) and gradient (B) substrates. Figure C and D compares the displacement along x (Λ_x) and y (Λ_y). Figures E and F compare the angular displacement of cells on both substrates.

In Figures B.3 and B.4 below, histograms of the local orientational order parameter (S_{Local})

are plotted in the optimal (20kPa) and stiff (40kPa) regions of substrates with different gradient strengths. In Figure B.3, the value of S is close to 0 on all histograms indicating nearly random alignment in this region. This further illustrates how A2058 cells seem to exhibit adurotactic behavior in their optimal region of stiffness. In Figure B.4, histograms of S_{Local} are also plotted, but in a 40kPa region. S in these regions was found to increase with the gradient strength, and was also much larger than the values found in the optimal region, indicating that the cells were aligning along the direction of the gradient.

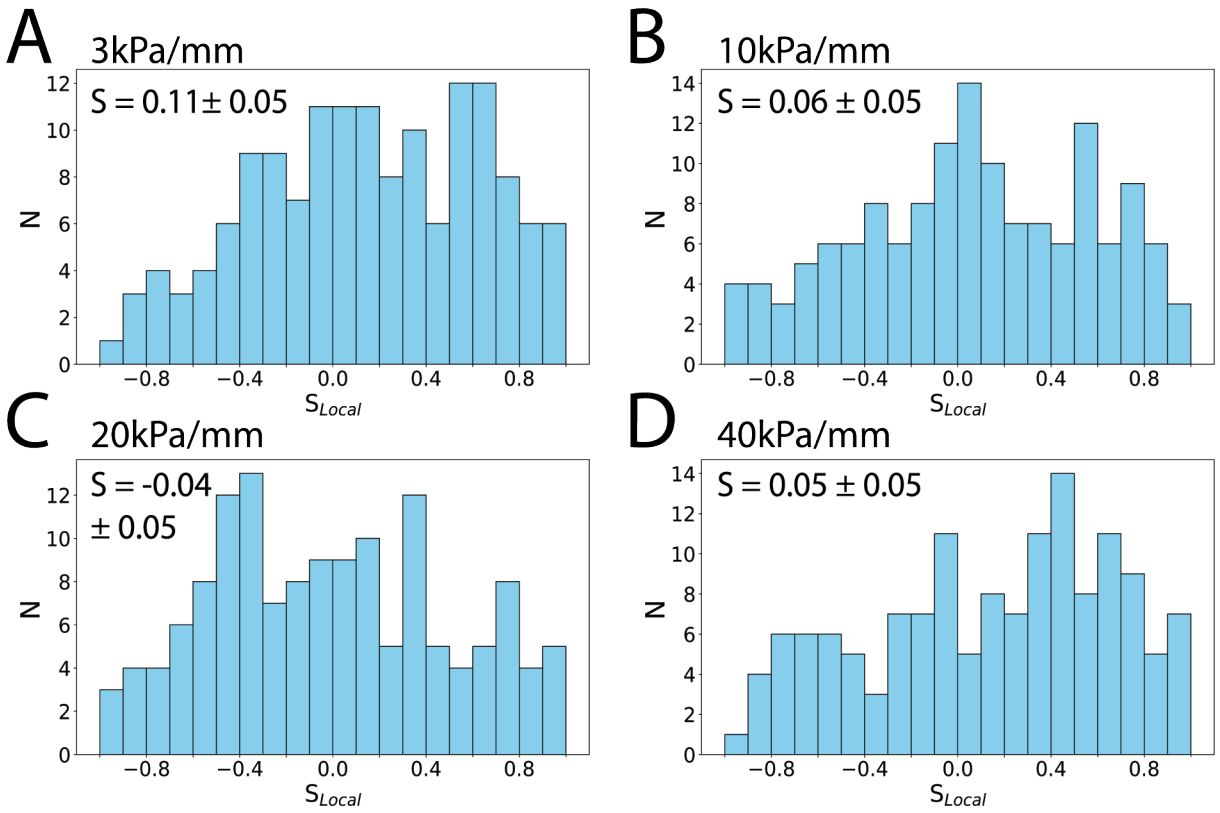

Figure B.3: Histograms of the orientational order parameter (S_{Local}) in the optimal region of the substrate.

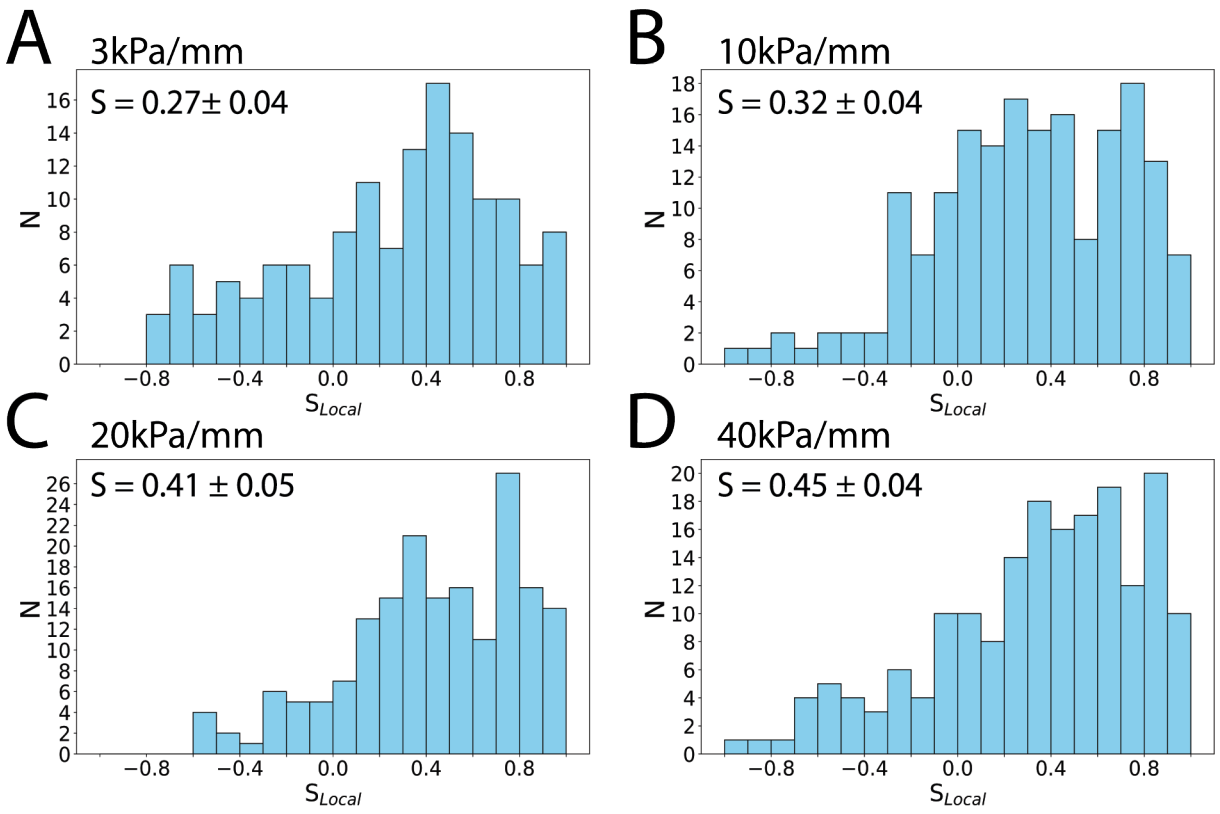

Figure B.4: Histograms of the orientational order parameter (S_{Local}) in the stiff region of the substrate.